the STEEL centre

Steel Centre Engineering Report No. 023 | August 2022

BEHAVIOUR OF EMBEDDED PLATES UNDER ECCENTRIC SHEAR LOADING IN REINFORCED CONCRETE

Caine Smithaniuk

Doug Tomlinson

UNIVERSITY OF ALBERTA

Behaviour of Embedded Plates Under Eccentric Shear Loading in Reinforced Concrete

by

Caine Smithaniuk

and

Douglas Tomlinson

Steel Centre Engineering Report No. 023

Department of Civil and Environmental Engineering
University of Alberta
Edmonton, Alberta, Canada

August 2022

Abstract

Embedded plates (embeds) are a common method of joining steel and concrete members in structures. Research at the University of Alberta emphasized the lack of consideration in the Canadian concrete design standard CSA A23.3:19 Annex D for the effect of reinforcement on anchorage capacity, as well as the treatment of combined loading for common shear-type connections. Conservatism in design and confusion for designers are manifestations of the current limitations of the design standard. There is currently no practical approach, codified or otherwise, that can accurately describe the behavior of embeds in reinforced concrete. This research project aims to improve the design of embeds by identifying limitations in current design practices, and then testing previously standardized embedded plates to assess the effects of supplementary reinforcement and common shear connections, parameters that are inadequately addressed by CSA A23.3:19 Annex D.

One four-stud embed standardized by Chin (2021) was tested in eccentric shear towards a free edge at a constant edge distance of 150 mm to the nearest row of anchors. Eight full-scale tests were conducted with shear reinforcement (10M stirrups) spaced at 250, 215, or 175 mm on centre with two different shear connection details (double angle and shear tab) that are commonly used in practice. From the test results, A23.3:19 was conservative in its calculation of concrete breakout strength in shear especially when tension-shear inter- action effects due to eccentricity of the shear load (distance between top of concrete to bolt line on the shear connection) are considered. An average test-to-predicted ratio of 3.75 was found when comparing test results that failed by concrete breakout to A23.3:19 predictions as they would be calculated by designers (i.e., including material resistance factors and the 5% fractile which is an additional safety factor that reduces capacity by ~25%), whereas this ratio is 1.17 when the material resistance factor is omitted and the 50% fractile (i.e., the

mean or average expression) is used to calculate concrete breakout strength. The latter test- to-predicted ratio is closer to unity because the failure mode shifted from shear to tension concrete breakout as shear reinforcement density increased, meaning that shear reinforce- ment was unable to increase capacity due to a lack of rotational restraint in the test system. Tension effects on embeds loaded in eccentric shear are significant and must be considered in design. When increasing shear breakout strength by adding supplementary reinforcement, tension breakout strength must also be increased to properly utilize shear reinforcement. When tension effects associated with a lack of rotational restraint are properly accounted for, expressions from Eligehausen et al. (2019) provide good estimates of capacity for the tests, with test-to-predicted ratios of 0.98 to 1.07. Interaction curves for the standardized four stud embed from Chin (2021) are also provided for ease of calculating shear capacity.

Acknowledgements

This research was funded by the Natural Sciences and Engineering Research Council (NSERC) Collaborative Research and Development program (CRDPJ 530162-18: Standardization of Embedded Plates for Steel-Concrete Connections in Buildings) and the Steel Centre at the University of Alberta. The in-kind donation of the embedded plates by Steel Centre members, Collins Steel and DIALOG, as well as the in-kind donation of concrete by Lafarge, is gratefully acknowledged.

Table of Contents

1 Introduction **1**

1.1 Background and Motivation 2

1.2 Objectives and Scope 4

1.3 Report Organization 5

2 Literature Review **6**

2.1 Introduction 6

2.2 Headed Anchors 6

2.2.1 Tension Failure Modes 7

2.2.1.1 Anchor Rupture 7

2.2.1.2 Concrete Cone Breakout 8

2.2.1.3 Anchor Pullout 12

2.2.1.4 Concrete Side Face Blowout 13

2.2.2 Shear Failure Modes 14

2.2.2.1 Anchor Failure 14

2.2.2.2 Concrete Pryout 16

2.2.2.3 Concrete Breakout 18

2.3 Anchor Groups 21

2.3.1 Anchor Groups Subjected to Tension Loads 21

2.3.2 Anchor Groups Subjected to Shear Loads 22

2.4 Summary 24

3 Development of CSA A23.3:19 Design Standard Anchorage to Concrete Provisions **25**

3.1 CSA A23.3:19 Design Provisions 26

3.1.1 Resistance Modification Factor, R 26

3.1.2 5% Fractile 28

3.1.3 Steel Failure in Tension 29

3.1.4 Pullout Failure 29

3.1.5 Concrete Side Face Blowout 30

3.1.6 Concrete Breakout in Tension 31

3.1.7 Steel Failure in Shear 34

3.1.8 Concrete Pryout 34

3.1.9 Concrete Breakout in Shear 35
3.2 Tension Shear Interaction 40
3.3 Limitations in Annex D 42

4 Additional Considerations for the Design of Embedded Plates 43
4.1 Behaviour of Embedded Plates in Reinforced Concrete 43
4.1.1 Sharma et al. (2018) Reinforced Concrete Breakout Model 52
4.1.2 Park et al. (2017) Reinforced Concrete Breakout Model 54
4.1.3 Summary 55
4.2 Effect of Moment Transfer into Embedded Plates 56
4.2.1 Tension Shear Interaction 59
4.2.2 Semi-Rigid Connections 61
4.2.3 Summary 64

5 Experimental Program 65
5.1 Introduction 65
5.2 Test Program 66
5.2.1 Embedded Plate Design 68
5.2.2 Reinforcement Details 70
5.2.3 Perimeter Reinforcement 71
5.3 Fabrication Process 71
5.4 Materials 72
5.5 Test Setup and Instrumentation 74
5.6 Loading Arm 76

6 Results and Discussion 80
6.1 Concrete Breakout Failure 89
6.2 Considerations for Anchor Group Design 90
6.3 Effect of Reinforcement on Embedded Plate Capacity 93
6.4 Effect of Connection Type on Embedded Plate Behaviour 94
6.5 Comparison to CSA A23.3:19 95
6.6 Discussion on Tension Shear Interaction 97
6.6.1 Design Aid for Calculating Anchorage Capacities 98
6.7 Comparison to Sharma et al. (2018) 100
6.8 Discussion of Park et al. (2017) 102

6.9 Serviceability Considerations 103
7 Summary and Recommendations 109
7.1 Summary 109
7.2 Conclusions 109
7.3 Recommendations for Future Work 111

References 112

Appendix A Design Calculations 118

Appendix B Load versus Crack Width Plots 125

Appendix C Material Properties 127

List of Tables

3.1 Resistance modification factor, *R* (adapted from CSA A23.3-19) 27

5.1 Test matrix.....67
5.2 Concrete cylinder and MOR 35 day strengths 73
5.3 Reinforcement properties.....73
5.4 Nelson stud properties 73

6.1 Test results.....81

List of Figures

1.1 Typical four-stud embedded plate with a double angle shear connection (left) and a shear tab (right) for connecting to the web of a wide-flange beam or channel. 1

1.2 Failure modes of anchors embedded in concrete loaded in (a) tension, and (b) shear (adapted from CSA (2019)) 2

2.1 Headed studs welded to a steel plate 6

2.2 Steel failure of a headed anchor, embedded in concrete, under tension loading 8

2.3 Concrete breakout failure where one half of the breakout cone has been re- moved (Nilforoush, 2017). 8

2.4 Stress cone method (adapted from Nilforoush (2017)) 9

2.5 Plan view of concrete breakout surface according to the CCD method (adapted from CSA (2019)) 11

2.6 Concrete breakout failure of a headed anchor preceded by pullout failure, where δ is the displacement of the anchor due to the crushing of concrete above the anchor head (adapted from Eligehausen et al. (2006)) 12

2.7 Side face blowout failure of a headed stud loaded in tension near an edge that is parallel to the applied load. 13

2.8 Shear anchor failure (CSA, 2019) 14

2.9 Reaction forces of headed anchor subjected to shear loading (adapted from Eligehausen et al. (2006)) 15

2.10 concrete pryout mechanism in headed anchors (adapted from Anderson and Meinheit (2005)) 16

2.11 Pushout test setup for examining shear behaviour of headed studs (Ollgaard et al. (1971)) 17

2.12 Concrete breakout mechanism in headed anchors (adapted from Fuchs et al. (1995)) ... 18

2.13 Breakout cone of headed anchor (a) in plan view and (b) section view (CSA, 2019) 20

2.14 Shear breakout cone area in elevation view (CSA, 2019) 20

2.15 Plan view of concentrically loaded anchor group with overlapping tension breakout cones and a nearby free edge (CSA, 2019) 22

2.16 Concentrically loaded anchor group with overlapping shear breakout cones (CSA, 2019) 23

3.1 Supplementary reinforcement for anchors loaded in (a) section view of tensile loading and (b) plan view of shear loading (CSA, 2019) 28
3.2 Tension breakout cone truncated by a free edge. 33
3.3 Influence of member thickness on shear capacity (adapted from Eligehausen et al. (2006)) 37
3.4 Projected failure area for an anchor near a corner of a member with $c_{a2} < 1.5c_{a1}$ (CSA, 2019) 40
3.5 Combined shear (V) and tension (T) load applied to a single anchor resulting from an inclined force (P). 40
3.6 Trilinear interaction curve, and interaction curve with $k = 1.5$ plotted against (a) single anchor test data and (b) the same data adjusted for the 5% fractile (Eligehausen et al., 2006) 41

4.1 Hanger reinforcement for shear loads permitted by Annex D (CSA, 2019) 43
4.2 Proximity requirements for bars to be considered effective in resisting shear load (bar is in tension) (CSA, 2019) 44
4.3 Depiction of the test setup used by Chin (2021). Note the pin supports at the front and back of the jack 46
4.4 (a) Test setup used by Sharma et al. (2017a) (adapted from Sharma et al. (2017a)) and (b) illustration of test setup boundary conditions from Sharma et al. (2017a) 47
4.5 Primary shear and secondary tension cracking due to the prying effect of an eccentric shear load (adapted from Sharma et al. (2017b)) 48
4.6 Embedded plate design and reinforcement layout for tension tests conducted by Bujňák et al. (2019) 51
4.7 Free body diagram offered by EN1994-2 (adapted from Sharma et al. (2017b)) 54
4.8 Tension (T) and compression (C) force couple induced by an eccentric shear load (V) and corresponding linear strain diagram if the baseplate is assumed to be rigid. 56
4.9 Trilinear interaction curve, and interaction curve with $k = 1.2$ plotted against single and multiple anchor test data where the governing failure mode is concrete breakout in shear (adapted from Eligehausen et al. (2006)) 58
4.10 Influence of baseplate compressive force on tension breakout capacity (adapted from Eligehausen et al. (2006)) 59

4.11 Tension shear interaction diagram shown in CSA A23.3:19 that includes the trilinear interaction curve proposed by Bode and Roik (1987) (CSA (2019)). 59
4.12 (a) Embed with angles welded to the baseplate along their toes, and (b) bolted double angle connection prying away from baseplate (adapted from Hong et al. (2002)) 61
4.13 Beam line AB and a typical moment rotation curve OQ (Jones et al., 1983). Point A is the maximum or fixed end moment, and point B is the rotation that would occur if the connection were a perfect pin 62

5.1 Plan drawing of block used for (a) ST-175^{P}, DA-175^{P}, ST-250^{P}, DA-250^{P}, and (b) ST-215^{B}, DA-215^{B}, PR-20M^{B}, PR-UR^{B} 68
5.2 Shop drawings for embedded plates with (a) double angles and (b) shear tabs. ST1, DA1, FP1, and NS150 are item marks for fabrication purposes. 69
5.3 Reinforcement cage prior to embed placement and concrete pour (lifting hooks not shown). 72
5.4 (a) Test setup prior to instrumentation installation and (b) pin connection between the jack and the strong wall 74
5.5 Test instrumentation 75
5.6 Schematic of instrumentation used in the test program. (a) Plan view and (b) section view 76
5.7 Embedded plate loaded (a) with uplift restraint and (b) without uplift re- straint (Sharma et al., 2017b) 77
5.8 Depictions of researcher's test setups indicating the degree of uplift restraint used. Restraint used in (a) the current test program, (b) by Chin (2021), and (c) by Sharma et al. (2018). Note that for (c) the shear load was not applied through a shear tab but is shown similar to (a) and (b) for consistency.....78
5.9 Rendered image of embedded plate with (a) wide-flange stub and clevis plate attached, and (b) with loading arms attached. 79
5.10 Rendered image of an embed with loading arms modified to include three bolts to connect loading arms directly to the angle legs or shear tab 79

6.1 Load versus net plate displacement curves calculated from LVDT and trans- ducer data for (a) the six tests that failed by concrete breakout and (b) the two tests that failed by weld rupture, plus ST-215^{B} for reference. 81
6.2 (a) Gap between top of concrete block and bearing support at beginning of test, and (b) at peak load when the gap was closed. 83
6.3 Locations of the points used in VIC 2D to calculate plate and block displace- ments (principal strains for ST-215 shown). 84

6.4 Comparison of the load displacement curves generated from LVDT and cable transducer data, and the DIC data (ST-250^{P} shown).....85
6.5 Load versus net plate displacement curves calculated using VIC 2D for (a) the six tests that failed by concrete breakout and (b) the two tests that failed by weld rupture, plus ST-215^{B} for reference. Curves plotted up to the point that DIC was no longer able to track displacements in front of the embed. 86
6.6 Side view of ST-175^{P} at peak displacement, displaying a combination of tension and shear breakout, or a pryout style failure 87
6.7 Side view of DA-250^{P} (a) at the beginning of the test, (b) just before weld rupture, and (c) weld rupture on the angle connection 88
6.8 Stabilizing effect of the bolted loading arm connection.....89
6.9 Typical concrete breakout cone for an anchorage loaded in shear towards a free edge (ST-215^{B} shown).....90
6.10 ST-250^{P} breakout cone. Note the shear breakout cone forming from the embed, while the tension breakout cone extends past the back of the embed.....90
6.11 Back stud of DA-215^{B} which yielded due to bending, but also experienced notable shear deformation just below the weld that connected it to the baseplate. 91
6.12 Load versus baseplate rotation curves for (a) the six tests that failed by concrete breakout and (b) the two tests that failed by weld rupture. 92
6.13 Load versus connection rotation curves for (a) the six tests that failed by concrete breakout and (b) the two tests that failed by weld rupture. 92
6.14 ST-250 and ST-175 at maximum displacement 94
6.15 Load-rotation curves for the baseplates (BP) and connections (W) for ST-215^{B} and DA-215^{B} 94
6.16 Failure surfaces of (a) ST-215^{B} and (b) DA-215^{B} 95
6.17 Comparisons of the test results with predictions from CSA A23.3.....96
6.18 Reduction in shear resistance due to interaction effects for the 4SEP. The un- factored stud shear strength is included and would be an upper limit. Curves shown for k = 1.2 and 1.67. 98
6.19 Interaction curves for the 4SEP designed by Chin (2021) plotted as a function of (a) eccentricity of shear load and (b) applied moment. 99
6.20 Comparisons predictions from Sharma et al. (2018) with test results from (a) this report and (b) Chin (2021).....101
6.21 Schematic showing how crack widths were estimated using two points, A and B, on either side of, and in close proximity to, the crack. 104
6.22 Locations where crack widths were measured 105
6.23 ST-250 crack widths.....106

6.24 (a) Comparison of crack widths at Location 1 and 2 for ST-175^{P} and ST-250^{P} and (b) comparison of crack widths at Location 1 for DA-175^{P} and DA-250^{P}. 107

List of Symbols

f_c^t specified compressive strength of concrete

λ_a factor to account for low-density concrete in certain concrete anchorage applications

φ_c material resistance factor for concrete

φ_s steel embedment material resistance factor for reinforcement

$\Psi_{c,N}$ modification factor for anchor resistance in tension based on presence or absence of cracks

$\Psi_{c,P}$ modification factor for pullout resistance of anchors based on presence or absence of cracks

$\Psi_{c,V}$ modification factor for resistance in shear of anchors based on presence or absence of cracks

$\Psi_{cp,N}$ factor used to modify the tensile strength of post-installed anchors intended for use in uncracked concrete without supplementary reinforcement to account for splitting tensile stresses due to installation

$\Psi_{ec,N}$ modification factor for resistance in tension to account for anchor groups loaded ec- centrically

$\Psi_{ec,V}$ modification factor for resistance in shear to account for anchor groups loaded eccen- trically

$\Psi_{ed,N}$ factor used to modify tensile strength of anchors based on proximity to edges of concrete member

$\Psi_{ed,V}$ modification factor for resistance in shear based on proximity to edges of concrete members

$\Psi_{h,V}$ factor used to modify shear strength of anchors located in concrete members with $h_a < 1.5c_{a1}$

A_{Nco} projected concrete failure area of a single anchor, for calculation of resistance in tension, when not limited by edge distance or spacing

A_{Nc} projected concrete failure area of a single anchor, or a group of anchors, for calculation of resistance in tension

$A_{se,N}$ effective cross-sectional area of anchor in tension

$A_{se,V}$ effective cross-sectional area of anchor in shear

$A_{V\,co}$ projected concrete failure area of one anchor, for calculation of resistance in shear, when not limited by corner influences, spacing, or member thickness

$A_{V\,c}$ projected concrete failure area of a single anchor or group of anchors, for calculation of resistance in shear

c_{a1} distance from the centre of an anchor shaft to the edge of concrete in one direction. If shear is applied to anchor, c_{a1} is taken in the direction of the applied shear. If tension is applied to the anchor, c_{a1} is the minimum edge distance

c_{a2} distance from centre of an anchor shaft to the edge of concrete in the direction or- thogonal to c_{a1}

$c_{a,min}$ minimum distance from centre of an anchor shaft to the edge of concrete

$c_{a1,n}$ distance from the centre of the furthers anchor from the edge of concrete in one direction

c_{ac} critical edge distance required to develop the basic resistance as controlled by concrete breakout or bond of a post-installed anchor in tension in uncracked concrete without supplementary reinforcement to control splitting

d_a outside diameter of anchor or shaft diameter of headed stud, headed bolt, or hooked bolt

e'_N eccentricity of normal force on a group of anchors. The distance between the resultant tension load on a group of anchors in tension and the centroid of the group of anchors loaded in tension. e'_N is always positive

e'_V eccentricity of shear force on a group of anchors; the distance between the point of shear force application and the centroid of the group of anchors resisting shear in the direction of the applied shear

f_r modulus of rupture of concrete

f_t tensile stress

f_{uta} specified tensile strength of anchor steel

f_{ya} specified yield strength of anchor steel

h_a thickness of member in which an anchor is anchored, measured parallel to anchor axis

h_{ef} effective anchor embedment depth

k_c coefficient for concrete breakout resistance in tension

k_{cp} coefficient for pryout resistance

k_v coefficient for concrete breakout resistance in shear

l_e load-bearing length of anchor for shear, not to exceed $8d_a$

M_a moment applied to a connection

M_f factored moment

n number of anchors in a group

N_f tensile force

N_r resistance in tension

N_{br} concrete breakout resistance in tension of a single anchor in cracked concrete

N_{cbgr} concrete breakout resistance in tension of a group of anchors N_{cbr}

concrete breakout resistance in tension of a single anchor N_{cpr}

pullout resistance in tension of a single anchor

N_{pr} pullout resistance in tension of a single anchor in cracked concrete

N_{sar} resistance of a single anchor or individual anchor in a group of anchors in tension as governed by the steel resistance

N_{sbgr} side-face blowout resistance of a group of anchors

N_{sbr} side-face blowout resistance of a single anchor

R resistance modification factor

s anchor centre-to-centre spacing

V_f shear force

V_r shear resistance

V_{br} concrete breakout resistance in shear of a single anchor in cracked concrete

V_{cbgr} concrete breakout resistance in shear of a group of anchors V_{cbr}

concrete breakout resistance in shear of a single anchor V_{cpgr}

concrete pryout resistance of a group of anchors

V_{cpr} concrete pryout resistance of a single anchor

V_{fa} shear force applied to a single anchor or group of anchors

V_{sar} resistance in shear of a single anchor or individual anchor in a group of anchors as governed by the steel resistance

1 Introduction

Embedded plates (embeds) are a common method of joining steel and concrete members in a structure. Embeds usually consist of a steel anchor plate welded to headed studs (Figure 1.1). The plate is attached to the formwork prior to pouring such that the top face of the plate is flush with the concrete surface, and the headed studs are embedded within the concrete. Once formwork is stripped, another member can then be connected to the embed. Embedded plates can be placed nearly anywhere within a concrete member, giving engineers and architects tremendous design flexibility. A number of factors affect the response of embeds to loading, such as the location, the number of studs, the length of studs, the connection between the supported member and the embed, and the reinforcement layout in the concrete.

Figure 1.1 – Typical four-stud embedded plate with a double angle shear connection (left) and a shear tab (right) for connecting to the web of a wide-flange beam or channel.

Applications of embedded plates include providing end support for steel beams, braces, or columns that are framing into concrete columns, beams or slabs/foundations. Depending on the application, embeds may be subjected to shear, tension, moment, or any combination thereof. Shear forces are transferred to the concrete through bearing along the anchor shaft, and tensile forces are resisted by the head of the anchor, which bears against the concrete directly above it.

Designers should be aware of all possible failure modes and understand how to identify which modes are most critical for their specific application of embeds. Embed failure modes are defined in the Canadian design standard for concrete, CSA A23.3.

1.1 Background and Motivation

There are a variety of failure modes for headed stud anchorages embedded in concrete, and Limit States Design (LSD) protocols require that the failure mode with the lowest capacity dictates connection capacity. Figure 1.2 shows possible failure modes for concrete anchorages, though some are not applicable to embeds, such as bond failure or concrete splitting. For headed studs of typical length/embedment for building applications (100-200 mm), failure is usually in the concrete (Eligehausen et al., 2006). Steel failures are typically associated with larger embedment depths for embeds loaded in tension or large edge distances for those loaded in shear.

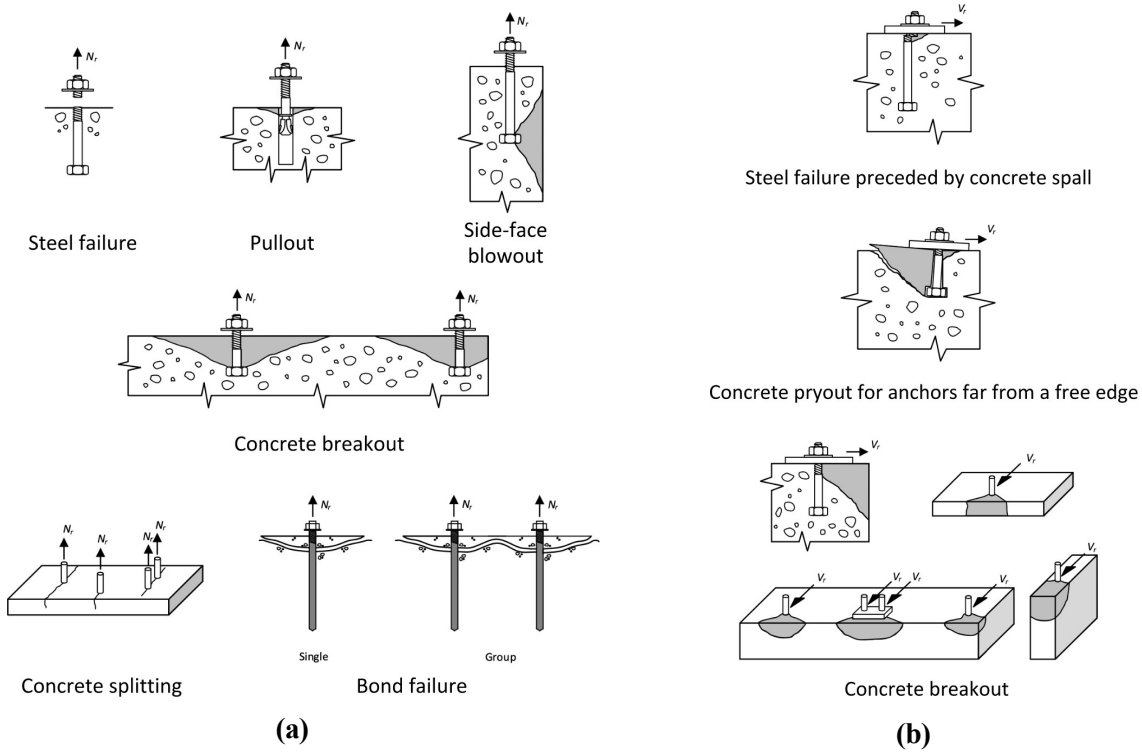

Figure 1.2 – Failure modes of anchors embedded in concrete loaded in (a) tension, and (b) shear (adapted from CSA (2019))

Annex D is a section of the CSA A23.3 that is considered to be difficult to work with by some designers. There are many factors to consider when designing embeds, and research upon which the provisions are based is not easily understood, nor is it readily available. There are few resources for designers to refer to beyond the standard. The Concrete Design Handbook is sparse in commentary on anchorage to concrete, and the Canadian Prestressed Precast Concrete Institute (CPCI) design manual provides a methodology for shear calculations from the Precast Concrete Institute (PCI) that is inconsistent with Annex D. Nonetheless, these connections must be designed to be safe and reliable. The uncertainty associated with an- chorage to concrete, coupled with the conservative nature of the standard's clauses, results in anchorages that are cautious and limiting to an engineers design.

One major contributor to the conservative nature of Annex D is that it essentially treats concrete as if it were unreinforced. There are a few factors that serve to modify the capacity of an anchorage system depending on the arrangement and amount of reinforcement but these provisions are a qualitative assessment of reinforcement's crack controlling ability and ductility rather than any sort of measure of increased capacity. Recently, research programs have been conducted with the intent to push the European design standard for fastening to concrete (EN1992-4) towards incorporating reinforcement effects into anchorage design. A better understanding of the behaviour of anchorages is required before these discussions can be had with respect to A23.3. Much of the basis of A23.3 is from empirical data from single anchor tests. Anchorages with multiple anchors, such as embeds, share similarities, but there are also important differences in their behaviour that are not well addressed in the design standard, such as the treatment of combined loading and distribution of forces to the anchors.

Interaction loading on embeds is not directly covered in Annex D. Guidelines are provided for tensile loading, shear loading, and combinations of the two from direct shear/tension loads. However, for shear loading no guidance is given for the treatment of moments, such as those induced from eccentric loading or partial restraint of the connecting member. De- signers often utilize tension-shear interaction equations to address this behaviour, but these equations are based on tests loaded by combined tension and shear, usually from an inclined load. These interaction diagrams may not adequately represent the behaviour of common shear-type connections to embeds, where loading is a combination of shear and moment.

1.2 Objectives and Scope

The objective of this research is broken down into two parts. The first is to provide a resource for designers and students to aid in understanding and navigating Cast-In-Place (CIP) an- chorage to concrete. The second is to better understand the behaviour of embeds subjected to shear loads in reinforced concrete to add context to the standardized embedded plates created by Chin (2021). To achieve these objectives, the following tasks were completed:

1. Conduct a literature review to provide a broad understanding of precast anchorage to concrete, with a focus on the effects of reinforcement and the type of shear connector used to transfer the load from the supported member to the anchorage;

2. Conduct eight experimental tests on a standardized embedded plate loaded in shear towards an edge with different reinforcement layouts and connection details; and

3. Analyze the test results and compare them to current Canadian design standards to determine whether the design standard is increasingly conservative for larger amounts of reinforcement. The test results are also compared to recent research that has taken aim at better assessing the capacity of embedded plates in reinforced concrete.

Recent research from Chin (2021) at the University of Alberta showed that minimal amounts of reinforcement (even that required to meet temperature and shrinkage criteria) result in an increase in capacity beyond what CSA A23.3 predicts. A portion of the current study is dedicated to understanding the relationship between reinforcement spacing and anchorage capacity for a typical connection configuration. Furthermore, by conducting tests on two connection types, the effect of more or less flexible connections between loads and the embed will be examined and compared to current design standards, and design norms.

The scope of this project is limited to four-stud embedded plates at a fixed edge distance loaded in shear in reinforced concrete. This style and size of embed was proposed as a stan- dard design detail by Chin (2021) as advised by industry experts. Using these plates, in conjunction with edge distances and reinforcement sizes that are representative of practical applications, will provide valuable insight into the design of embedded plates.

1.3 Report Organization

This report is divided into seven chapters. Chapter 2 is a literature review that provides a summary of the state of the art on CIP anchorage to concrete. The focus is concrete breakout in shear. However, Chapter 2 also serves as a reference for students and designers. Section 2.2 summarizes relevant research for failure modes pertaining to headed studs, with a focus on concrete breakout. Sections 2.3.1 and 2.3.2 expand upon this discussion to include anchor groups, which is a more general term for embedded plates and is the focus of this report. Chapter 3 further summarizes this information and, where possible, shows how this research has been incorporated into the Canadian design standard. Research that has examined the effects of reinforcement on concrete anchorage is presented in Chapter 4, as well as the consideration of eccentric shear and combined loading. Where possible, detailed discussions of test programs are presented; however, some of the research for anchorage to concrete that has contributed to North American design standards and codes, such as CSA A23.3:19 and ACI 318-19, was carried out in Europe and is either inaccessible or not published in English Chapter 5 describes the experimental test program that was used to evaluate the report objectives. Chapter 6 details the results of the test program and discusses the test results as they relates to the objectives and beyond. Finally, Chapter 7 summarizes the work that was completed and reiterates the key observations drawn from the study and provides recommendations for future studies on the topic of embedded plates subjected to shear loading in reinforced concrete.

2 Literature Review

2.1 Introduction

This chapter summarizes research conducted on concrete anchorage as it applies to headed anchors or studs, which are an integral part of embedded plate (embed) connections. Rele- vant research on anchorage to concrete is discussed to understand the background on which the current design standard, CSA A23.3:19 Annex D, is built. Limitations in the current design standards that are the focus of this report are discussed in further detail.

2.2 Headed Anchors

Embeds usually consist of a steel plate welded to headed anchors (studs). Headed studs consist of a smooth steel rod with a flat head at one end. Typical studs have a head diameter around twice the shank diameter that allow studs to transfer force to concrete through bearing. Groups of four headed studs welded to a steel baseplate are shown in Figure 2.1.

Figure 2.1 – Headed studs welded to a steel plate

In this section failure modes for headed anchors are presented. Relevant research is shown with proposed equations for calculating the capacity for these failure modes.

2.2.1 Tension Failure Modes

Cast-In-Place (CIP) anchorages may experience one of four different failure modes when sub- jected to tensile loads: anchor rupture, anchor pullout, concrete cone breakout, or concrete side-face blowout.

2.2.1.1 Anchor Rupture

Anchor rupture is a desirable failure mode as it is the most ductile and most predictable. Pro- vided that the anchor plate and connecting weld are designed to preclude failure of a different element, the anchor will fail under uniaxial tensile stress (Figure 2.2). With modern welding tools designed specifically for headed anchors making the welding process consistent and the local increase in hardness and strength due to welding effects, anchor failures are usually limited to the unaffected base metal of the anchor (Anderson and Meinheit, 2000). Anderson and Meinheit (2000) conducted 23 tensile tests on headed anchors and recommended using the yield stress to calculate the capacity when the stud material has a well-defined yield point, and the ultimate strength otherwise. The steel typically used for headed studs is AWS Type B steel which does not have a clear yield plateau (Chin, 2021), so design standards typically use the ultimate strength. Anchor capacity can be calculated by taking the product of its cross-sectional area, A_s, and ultimate strength, f_{uta} (Equation (2.1)).

$$N_r = A_s f_{uta} \tag{2.1}$$

Anchor rupture tends to govern for deep embedments (long anchors) or when anchors are located "in the field," meaning they are sufficiently far from free edges or discontinuities, such that concrete failure is not a concern.

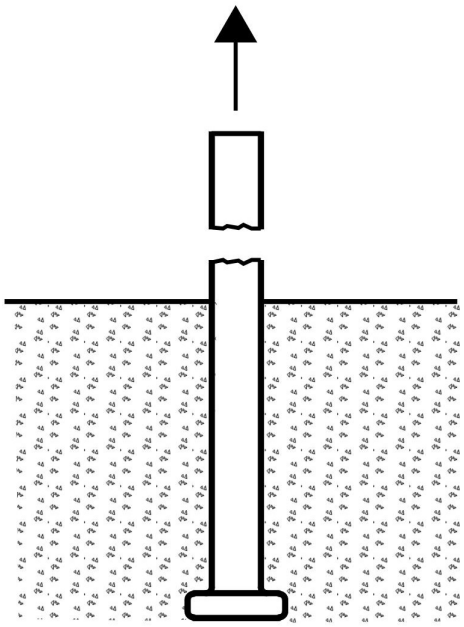

Figure 2.2 – Steel failure of a headed anchor, embedded in concrete, under tension loading

2.2.1.2 Concrete Cone Breakout

Concrete cone breakout is characterized by the anchor breaking free of the concrete member, bringing with it a conical section of concrete that originates at the head of the anchor and is truncated by the surface of the member as shown in Figure 2.3. Tensile breakout cones usually form at 35° from the horizontal, although this angle varies between 35 and 45° depending on the anchor embedment depth, or any disturbances in the concrete stress distribution due to adjacent loading (Eligehausen et al., 2006). Typically this angle increases with embedment depth.

Figure 2.3 – Concrete breakout failure where one half of the breakout cone has been removed (Nilforoush, 2017).

Concrete breakout is likely the most studied failure mode in concrete anchorages. Concrete breakout, a tensile failure of the concrete, has been analyzed using a number of different models.

Cannon et al. (1981) presented the Stress Cone Method (SCM) as the first codified ap- proach in North America, being adopted by ACI 349, the United States code for the design of nuclear structures, in 1979. The SCM assumes that breakout cones form at 45° from the horizontal, and that failure occurs when a tensile stress equal to the concrete rupture stress, f_r, is reached on the entire projected failure surface (Figure 2.4).

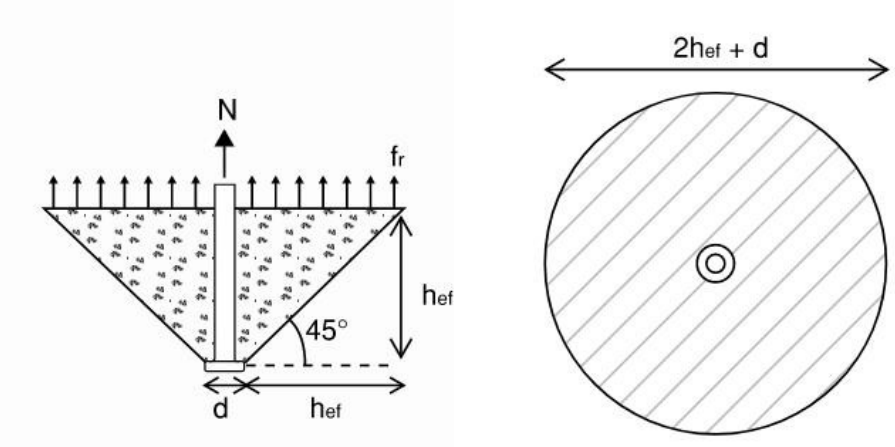

Figure 2.4 – Stress cone method (adapted from Nilforoush (2017))

There have been multiple efforts to derive analytical solutions for concrete breakout. By assuming concrete to be perfectly plastic Bræstrup et al. (1976) presented a solution to axisymmetric punching shear in slabs that could be translated to headed anchors if the em- bedment depth is taken as the slab thickness. This, along with other assumptions, allowed Bræstrup et al. to find an upper bound solution for the optimal failure cone shape and failure load. However, this model only shows agreement with test results when the tensile strength of concrete is assumed to be approximately five percent of its true value (Bažant, 1984). Bažant (1984) showed that such strength criteria (i.e., theories of elasticity or plasticity) are only applicable when the relative structure size is small and are unable to describe the behaviour of concrete fracture on a larger scale due to the heterogeneity of concrete. For design, concrete is assumed to be homogeneous, but the fracture behaviour of concrete differs from other brittle materials such as glass or ceramics in that crack propagation through the

cement is blunted by aggregates. Methods have been proposed to describe this behaviour, with the fracture process zone proposed by Bažant and Oh (1983) being the most well known. The Fracture Process Zone (FPZ) refers to the theoretical region around the tip of a prop- agating crack where there is a concentration of microscopic cracks. In this region there is a gradual strain softening behaviour rather than the traditional design assumption, which is that as soon as concrete is cracked it is unable to carry any load. Other methods that account for non-linear behaviour of concrete have also been proposed, but are impractical on a broader scale (Eligehausen et al., 2006).

Currently, the most practical option has been to estimate the breakout strength using empir- ically derived equations that also account for well understood principles. This methodology led to the Concrete Capacity Design (CCD) method (Fuchs et al., 1995), which is now incor- porated into many building codes and standards, including ACI 318-19 and CSA A23.3:19, which apply to the design of steel-reinforced concrete structures in the United States and Canada, respectively. Some modifications have been made, and more proposed in recent years, but the CCD method remains largely unchanged since its inception. Per the CCD method, the concrete breakout strength is calculated by Equation (2.2).

$$N_{cbr} = k_c \sqrt{f_c'} h_{ef}^{1.5} \tag{2.2}$$

where N_{cbr} is the concrete breakout resistance of a single headed anchor loaded in tension, k_c is an empirical constant equal to 16.8 for headed anchors, f_c' is the concrete compressive strength, and h_{ef} is the anchor embedment depth.

k_c was calibrated by Fuchs et al. (1995) using an extensive database of tests on a vari- ety of anchor types, such as headed, expansion, and undercut anchors (Nilforoush, 2017). Equation (2.2) assumes that N_{cbr} is proportional to the square root of the concrete compres- sive strength since it is generally accepted that the tensile strength of concrete is proportional to the square root of the compressive strength for normal strength concrete.

Eligehausen et al. (1992) conducted 35 pullout tests on headed studs embedded in mini- mally reinforced concrete (temperature and shrinkage reinforcement) with an average cube strength of 31 MPa ($f_c' \approx 36$ MPa) and embedment lengths from 50 mm to 450 mm. Most

tests failed by concrete breakout, except tests with an effective embedment depth of 50 mm. These anchors had a diameter, d_a, of 8 mm, and failed by steel rupture. However, following this steel rupture the researchers drilled a hole in the underside of the specimen and con- ducted pushout tests with those anchors to force a breakout cone to form. In any case, tests showed agreement with Equation (2.2). The SCM proposed by Cannon et al. (1981), which assumes that breakout strength is proportional to h_{ef}^2, derived this proportionality based on the area of the breakout surface being a function of the square of the embedment depth. Whether the breakout cone is assumed to be conical (Figure 2.4), or pyramidal (Figure 2.5), the surface area of the failure body is a function of the embedment depth.

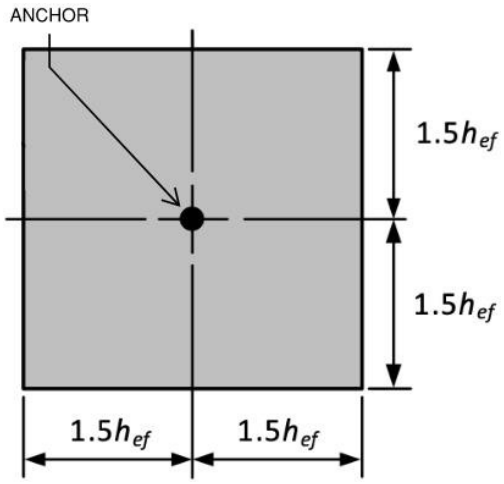

Figure 2.5 – Plan view of concrete breakout surface according to the CCD method (adapted from CSA (2019))

While this relationship is valid for a range of embedment lengths, it becomes unconservative at large embedment depths because it fails to account for the size effect, which is responsible for an inversely proportional relationship between breakout strength and h_{ef} (Fuchs et al., 1995). The size effect is well-known in concrete subject to cracking, or fracture, and explains why the relative strength of a member decreases as the member size increases. A detailed explanation of the size effect, and the associated crack band model, are given in Bažant (1984) and Bažant and Oh (1983), respectively.

Eligehausen et al. (1992) concluded that breakout capacity can be predicted with reasonable accuracy using fracture mechanics, since fracture mechanics accounts for the size effect un-

like strength-based criteria such as stress or strain failure criteria commonly used in design. However, Linear Fracture Mechanics (LFM) is only applicable to concrete when the struc- ture size is larger than any member or structure relevant to this discussion (Bažant and Oh, 1983). In other words, Non-Linear Fracture Mechanics (NLFM) is necessary to fully describe the fracture behaviour of concrete for any given structure size. However, since LFM predicts the most severe size effect, where $f_r \propto h_{ef}^{-1/}$, it is conservative to apply this relationship to structures of all sizes.

Fuchs et al. (1995) combined this information with the observations from Cannon et al. (1981) and presented Equation (2.2) with the factor of h^2 $_{ef} \cdot h_{ef}^{-1/2} = h_{ef}^{1.5}$.

2.2.1.3 Anchor Pullout

Anchor pullout is more common in post-installed anchors or CIP anchors without heads such as deformed bars, but this failure mode is still possible with headed anchors. With headed studs, anchor pullout initiates from large bearing stresses crushing the concrete above the anchor head. Eligehausen et al. (2006) reported that the stress in the bearing area (the concrete directly above the anchor head) can be up to 15 times greater than the compressive strength due to confinement effects. When concrete immediately above the anchor head crushes, the anchor can significantly displace, which reduces the embedment depth, and eventually a reduced concrete breakout cone forms (Figure 2.6).

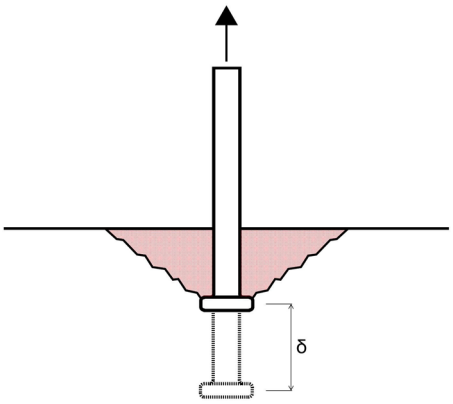

Figure 2.6 – Concrete breakout failure of a headed anchor preceded by pullout failure, where δ is the displacement of the anchor due to the crushing of concrete above the anchor head (adapted from Eligehausen et al. (2006))

Equations that estimate pullout failure for headed studs generally have the following form:

$$N_{cpr} = \alpha A_{brg} f_c^t \tag{2.3}$$

where N_{cpr} = pullout capacity of a headed anchor (N), α = coefficient ranging from 10 to 15, and A_{brg} = bearing area of the anchor head (mm^2). The bearing area of the anchor head is the full area above the anchor head minus the shank cross-sectional area. Eligehausen et al. (2006) reported that the ultimate bearing pressure varies with embedment depth, ranging anywhere from $10f_c^t$ to $15f_c^t$. α is used to calibrate the equation depending on the ultimate bearing stress, and uses a value between 10 and 15. Typically, larger values of α are associated with deeper embedments, whereas shorter embedment depths leave the anchor head closer to the surface of the concrete, which reduces the positive effects of confinement of the concrete above the anchor head.

2.2.1.4 Concrete Side Face Blowout

Side face blowout is characterized by a portion of concrete bursting laterally from the anchor head when the anchor is subjected to a tensile force near a free edge. According to Elige- hausen et al. (2006), large quasi-hydrostatic pressure near the head of the stud generates a lateral bursting force proportional to the applied tensile force. Similar to post-tension anchorage zones, the dispersion of compressive forces generates bursting forces that, unless the edge distance is sufficiently large or adequate reinforcement is present to confine the bursting forces, cause blowout perpendicular to the applied load (Figure 2.7).

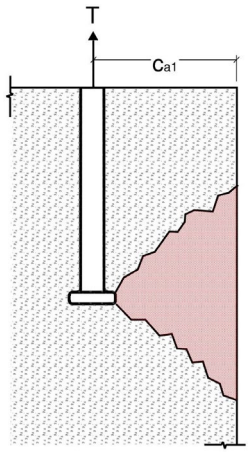

Figure 2.7 – Side face blowout failure of a headed stud loaded in tension near an edge that is parallel to the applied load.

Furche and Eligehausen (1991) conducted tensile tests on thirty-five 25 mm diameter headed anchors located near a concrete edge and found that side face blowout strength increased linearly with edge distance, c_{a1}. Further testing suggests that strength increases with $c^{0.75}$ (DeVries, 1996), though North American building codes use a linear relationship between edge distance and blowout strength. The point at which failure transitions from side blowout to concrete breakout is around 0.3 to 0.5 times the embedment depth in unreinforced concrete (Eligehausen et al., 2006). Eligehausen et al. (2006) summarized the work of Eligehausen and Hoffman in 2002, which proposes Equation (2.4) for the calculation of side face blowout:

$$N_{sbr} = 21 c_{a1}^{0.75} A_{brg}^{0.5} f_c^{0.75} \tag{2.4}$$

where c_{a1} = distance from the centre of the anchor to the edge of concrete.

2.2.2 Shear Failure Modes

This section presents possible shear failure modes, along with associated literature, for headed studs. There are three modes of shear failure: anchor failure, concrete breakout, and concrete pryout.

2.2.2.1 Anchor Failure

Shear failure is characterized by local crushing of concrete directly in front of the top of the anchor followed by steel shear failure, shown in Figure 2.8. Of the three possible shear failure modes, anchor failure is most likely to occur when embedment depths are large and the anchor is far from any free edges.

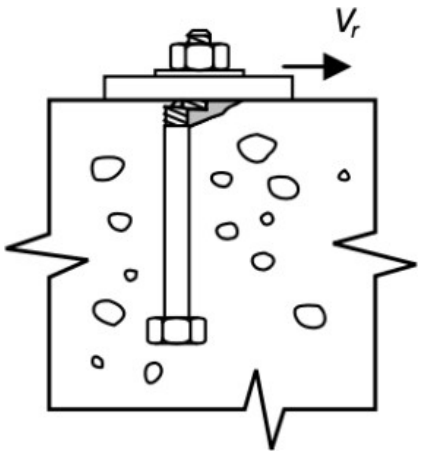

Figure 2.8 – Shear anchor failure (CSA, 2019)

Shear failure is more complex than tensile failure. Since the typical headed stud is rigidly connected to an attachment, such as an anchor plate, the shear load induces a tension- compression couple, shown in Figure 2.9, where shear load, V, is resisted through bearing, V_b, and causes a tensile stress, N, in the stud due to the bearing of the baseplate on the concrete member, C.

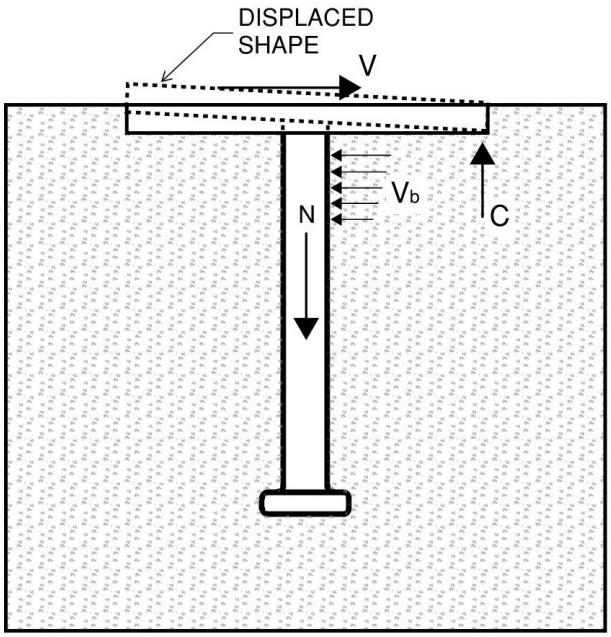

Figure 2.9 – Reaction forces of headed anchor subjected to shear loading
(adapted from Eligehausen et al. (2006))

Researchers have tried to analyze studs using classical theories of beams on elastic founda- tions to determine the combined stress state and predict the failure load, but high coefficients of variation in those results led to unreliable solutions. Instead, Eligehausen and Fuchs (1986) proposed Equation (2.5).

$$V_{sar} = \alpha A_{se,v} f_{uta} \tag{2.5}$$

where V_{sar} = resistance of the anchor in shear (N), α = test-to-calculated ratio of V_{sar}, $A_{se,v}$ = effective cross-sectional area of an anchor in shear (mm^2), and f_{uta} = specified tensile strength of the anchor (MPa).

α depends on the anchor type. Eligehausen and Fuchs (1986) conducted 220 tests on post- installed anchors and proposed $\alpha = 0.68$ when f_{uta} is the nominal steel strength. However,

the true steel strength is likely 10 to 20% larger than the nominal value although this was not tested. Taking this into account, $\alpha = 0.6$ was recommended if true tensile strengths are used rather than nominal strengths. Headed studs typically have larger shear strength com- pared to post-installed anchors that have non-uniform cross sections and are rarely rigidly connected to whatever is applying load. Headed studs have their largest strength in the region of largest shear forces, their connection to the baseplate, due to localized increases in strength associated with welding. Anderson and Meinheit (2000) conducted 328 tests with headed anchors with diameters ranging from 13 mm to 16 mm and embedment depths of 79 mm to 106 mm. Of those tests, 97 experienced anchor failure through either the anchor or the weld between anchor and baseplate. Anderson and Meinheit (2000) proposed $\alpha = 0.76$ for headed studs when using true tensile strength, and $\alpha = 0.92$ when using nominal tensile strength. Of those 97 tests, 17 failed at the weld. If those tests are omitted, and only the shank of the anchor is considered, α becomes 0.86 and 1.0 when using the true and nomi- nal tensile strengths, respectively. Lin et al. (2014) conducted six pushout tests on headed anchors in unreinforced concrete in which all tests failed the anchor, and found that the α value proposed by Anderson and Meinheit (2000) for headed studs is reasonable.

2.2.2.2 Concrete Pryout

Concrete pryout is closely related to concrete tension breakout. First, localized crushing or spalling of concrete directly in front of an anchor causes the anchor to deflect forward, which generates a force couple resolved by the head of the anchor bearing on the concrete behind it. This bearing force causes a breakout cone to form on only one side of the anchor, shown in Figure 2.10.

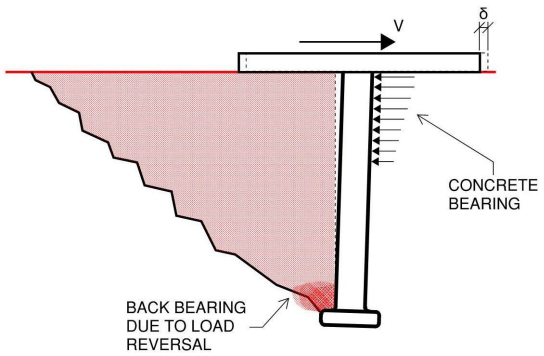

Figure 2.10 – concrete pryout mechanism in headed anchors (adapted from Anderson and Meinheit (2005))

Ollgaard et al. (1971) conducted 48 pushout tests on W200x59 members welded to headed studs embedded in concrete blocks on either side (Figure 2.11).

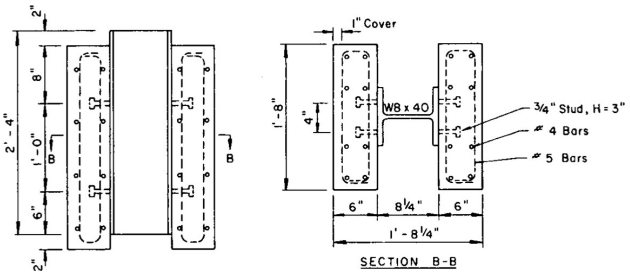

Figure 2.11 – Pushout test setup for examining shear behaviour of headed studs (Ollgaard et al. (1971))

The predominant failure mode was concrete pryout, and Ollgaard et al. (1971) proposed the following empirical equation to estimate pryout capacity, V_{cpr}, of the studs.

$$V_{cpr} = 1.106 A_s (f_c')^{0.3} E_c^{0.44} \tag{2.6}$$

where V_{cpr} is the concrete pryout resistance, A_s is the cross-sectional area of the anchor shank, and E_c is the concrete elastic modulus. Other methods of estimating pryout capacity relate it to concrete breakout. Zhao (1995) proposed that pryout capacity be calculated as the breakout capacity multiplied by a modification factor, as shown in Equation (2.7).

$$V_{cpr} = k_{cp} N_{cpr} \tag{2.7}$$

where k_{cp} = concrete pryout coefficient, and N_{cpr} = concrete breakout strength as per Equa- tion (2.2) (N).

Other researchers indicated that pryout capacity is also affected by factors such as anchor cross-sectional area and concrete density (Ollgaard et al., 1971; Anderson and Meinheit, 2005). This is intuitive given that the preceding spalling/crushing ahead of the anchor caused by the bearing stresses is related to the bearing area of the anchor transmitting the force. Jebara et al. (2016) conducted 45 shear tests on headed anchors welded to baseplates with embedments from 30 mm and 90 mm, and anchor diameters of 8 mm to 44 mm. In all cases the anchors were far from any free edges, or "in the field". From those results, Equation (2.8) was proposed.

$$V_{cpr} = 6 d_a^{1/2} f_{cc,200}^{1/2} h_{ef}^{1.5} \tag{2.8}$$

where d_a = anchor diameter (mm) and $f_{cc,200}$ = concrete cube compressive strength (MPa).

While this may be reasonable for single anchors, tests by Anderson and Meinheit (2005) on anchor groups suggest that anchor spacing may also play a role in the pryout capacity in the case of multiple anchors rigidly connected to a baseplate. This is especially relevant in the case of sandwich panels or other thin precast concrete members, where pryout often governs (Chin, 2021). In these cases, the option does not exist in CSA A23.3:19 Annex D to modify the capacity by changing the anchor diameter, or spacing of an anchor group. For the time being, Annex D defaults to Equation (2.7).

2.2.2.3 Concrete Breakout

The final failure mode, concrete breakout, is the most heavily studied shear failure mode of the three. This is likely because it has been the most difficult to quantify. Concrete breakout tends to occur when headed anchors are loaded in shear perpendicular to a free edge, as shown in Figure 2.12.

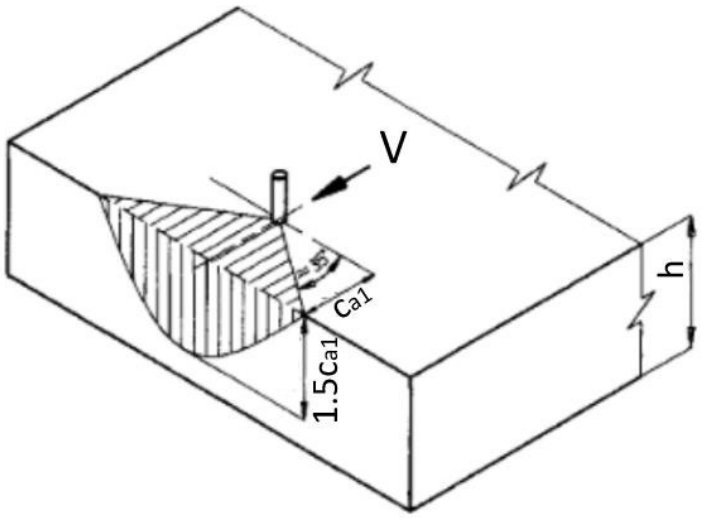

Figure 2.12 – Concrete breakout mechanism in headed anchors (adapted from Fuchs et al. (1995))

As load increases, a failure surface forms at the anchor that eventually propagates to the concrete edge. In general, concrete breakout in shear is similar to concrete breakout in

tension, in that it can be thought of as a half tension breakout cone. However, in tension the capacity is related to the embedment depth, whereas capacity is related to edge distance, c_{a1}, for shear. Equation (2.9) shows the concrete breakout strength that was proposed by Fuchs et al. (1995).

$$V_{cbr} = k_v \left(\frac{l_e}{d_a}\right)^{0.2} \sqrt{\frac{d_a}{c_{a1}}} \sqrt{f'_c}^{1.5} \tag{2.9}$$

where V_{cbr} = concrete breakout resistance in shear (N), k_v = constant equal to 1.0 for headed anchors, l_e = effective embedment depth, taken as h_{ef} for headed studs (mm), d_a = anchor diameter (mm), and c_{a1} = distance from edge of concrete to centreline of the anchor nearest to the free edge (mm).

This is similar to Equation (2.2), but is related to the edge distance rather than embed- ment depth. Similar to the tension breakout equation, Equation (2.9) is semi-empirical and produced from curve fitting test results. Historical attempts at deriving analytical solutions to concrete breakout in tension as described in Section 2.2.1.2 also apply to shear, and have likewise been largely unsuccessful (Eligehausen et al., 2006).

For some anchors, the effective embedment length, l_e, differs from the full length because of changes in stiffness along their length, which affects the bearing stress distribution when loaded in shear (Eligehausen et al., 2006). Headed anchors are relatively rigid compared to other anchor types, especially when welded to baseplates, and can be considered to have constant stiffness over their entire length.

For any anchor type, l_e has an upper limit of $8d_a$. There is little mention of the justi- fication for this limit other than the suggestion that this is the maximum effective load bearing length (Eligehausen et al., 2006). It is logical to assume that for long anchors there is an inflection point somewhere along their length when they deform under shear, with this perhaps coinciding with $8d_a$.

An upper limit was later imposed on Equation (2.9) after Eligehausen and Hofmann (2003) showed that Equation (2.9) overestimates capacity as anchor diameter increases beyond 25 mm, which was not noted earlier as the majority of tests used to generate Equation (2.9)

were conducted on anchors with diameters smaller than 25 mm and embedment depths less than eight times the anchor diameter (Grosser, 2012).

As with tensile breakout, shear breakout cones tend to form at approximately 35˚ angles (Fuchs et al., 1995), as shown in Figures 2.13a and 2.13b. The angle for any given anchor ranges between 30 and 45˚, increasing with edge distances, though 35˚ is considered an av- erage value (Grosser, 2012). For 35˚, the length of the breakout cone along the free edge of the concrete is approximately $3c_{a1}$.

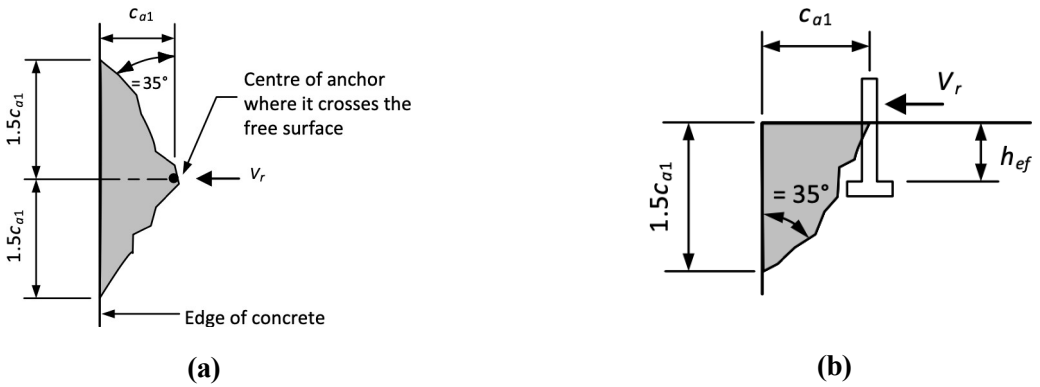

Figure 2.13 – Breakout cone of headed anchor (a) in plan view and (b) section view (CSA, 2019)

The area of the resulting breakout surface, $A_{V\,co}$ is then a function of edge distance, as shown in Figure 2.14.

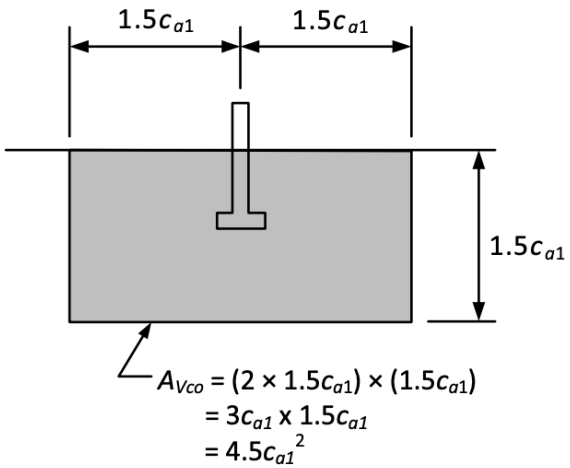

Figure 2.14 – Shear breakout cone area in elevation view (CSA, 2019)

If the depth of the member, h_a is less than $1.5c_{a1}$, the breakout area will be truncated by the bottom surface of the concrete member, thereby reducing anchor capacity relative to a thicker member, discussed further in Sections 2.3.1 and 2.3.2. While this breakout area is not used explicitly in capacity calculations for individual anchors (unless the member is thin), it is important in anchor groups.

2.3 Anchor Groups

Literature presented to this point applies to single headed anchors subjected to shear or tension loading. However, it is common to use multiple anchors located in close proximity to one another, loaded simultaneously by way of a common baseplate that is connected to the studs, as in the case of the embed plate shown in Figure 1.1, which is the connection type of interest in this report. This section summarizes methods used to calculate anchor capacities when multiple anchors are grouped closely together. Certain failure modes are unaffected by the number of anchors. For example, the tensile or shear capacity of the steel studs is simply the summation of individual anchor capacities regardless of spacing.

2.3.1 Anchor Groups Subjected to Tension Loads

When anchor groups are loaded simultaneously, the breakout resistance is not the sum of the strength of each individual anchor, nR_{anchor}. When the centre-to-centre distance between two anchors, s, is less than $3h_{ef}$ and $3c_{a1}$ for tensile and shear failures respectively, the failure surfaces overlap and the capacity of an anchor group will adhere to Equation (2.10).

$$R_{anchor\ group} \leq nR_{anchor} \tag{2.10}$$

where n is the number of anchors. The capacity of an anchor group in tension can be calculated by considering the size of the total failure surface, A_{Nc}, accounting for the overlap between the individual failure surfaces of each anchor (Fuchs et al., 1995), as shown in Figure 2.15.

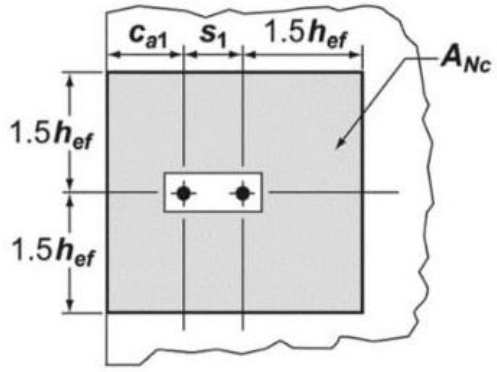

Figure 2.15 – Plan view of concentrically loaded anchor group with overlapping tension breakout cones and a nearby free edge (CSA, 2019)

The resulting capacity is modified by the ratio of total breakout area to the area of a single breakout cone, as follows.

$$N_{cbgr} = \frac{A_{Nc}}{A_{Nco}} N_{cbr} \tag{2.11}$$

where N_{cbgr} = concrete breakout capacity of an anchor group (N), A_{Nc} = breakout cone area of an anchor group (mm^2), A_{Nco} = breakout cone area of a single anchor (mm^2), and N_{cbr} = concrete breakout capacity of a single anchor (N).

From this, the critical spacing, s_{cr}, is $3h_{ef}$. If two anchors are loaded concentrically and the spacing between them, s, is larger than s_{cr}, then the failure surfaces do not overlap and each anchor is unaffected by the other (i.e., capacity can be calculated as nN_{cbr}). This implies that the capacity as predicted by Equation (2.11) is proportional to the projected failure area. These values (e.g., breakout cone size, critical spacing) depend on the assumption that the breakout cone angle is 35°.

2.3.2 Anchor Groups Subjected to Shear Loads

The shear breakout area of anchor groups is treated similarly to the tension breakout areas discussed in Section 2.3.1, and is shown in Figure 2.16.

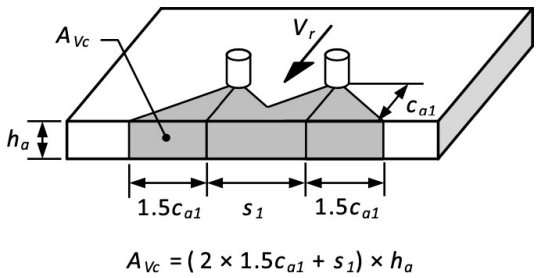

Figure 2.16 – Concentrically loaded anchor group with overlapping shear breakout cones (CSA, 2019)

While the failure surface for a single anchor has an area, $A_{V\,co}$, of $4.5c_{a1}^2$, the failure surface for the group of anchors shown in Figure 2.16 is calculated using Equation (2.12).

$$A_{V\,c} = \min(h_a,\ 1.5c_{a1}) \cdot (1.5c_{a1} + s + 1.5c_{a1}) \tag{2.12}$$

where h_a is the member depth.

If the member is less than $1.5c_{a1}$ deep, the breakout cone is truncated by the bottom surface of the member. Capacity is then modified by the ratio of the total breakout area to the area of a single breakout cone (Equation (2.13)).

$$V_{cbgr} = \frac{A_{V\,c}}{A_{V\,co}} V_{cbr} \tag{2.13}$$

where V_{cbgr} = concrete breakout capacity of an anchor group (N), $A_{V\,c}$ = breakout cone area of an anchor group (mm^2), $A_{V\,co}$ = breakout cone area of a single anchor (mm^2), and V_{cbr} = concrete breakout capacity of a single anchor (N). The critical spacing, s_{cr}, is $3c_{a1}$. If two anchors parallel to an edge are loaded concentrically and the spacing between the two, s_1, is larger than the critical spacing, then the failure surfaces do not overlap and the anchors are not affected by each other, in which case capacity can be calculated as the sum of the individual anchor capacities.

2.4 Summary

In this chapter, a literature review of research conducted on headed anchors was presented. Various failure modes and design equations for calculating anchor capacities were discussed. Considerations for anchor group design were also shown since these are applicable to embeds. Many equations presented in this chapter differ from those in design standards such as CSA A23.3:19 Annex D. The following chapter summarizes the provisions of Annex D as they apply to embeds and highlights why those provisions may differ from research outcomes presented in this chapter.

3 Development of CSA A23.3:19 Design Standard Anchorage to Concrete Provisions

Many equations or coefficients for the various anchor failure modes presented in Chapter 2 are different than what is shown in CSA A23.3:19 Annex D. This section presents the pro- visions as currently written in A23.3:19 and links research outcomes with those provisions.

In the 1970s, the κ method was developed in Germany (Eligehausen, 2017). This is the first known design method for concrete anchorage as far as the author is aware. The κ method predicts the capacity of anchorages based on the capacity of a single stud multiplied by a modification, or κ, factor.

In North America, Cannon et al. (1981) adapted provisions from an appendix of the ACI 349 committee into what is now referred to as the stress cone method. In 1985, the stress cone method was adopted by ACI 349, which is the American code governing the design of nuclear structures.

The κ and cone methods continued to be used in building applications until Fuchs et al. (1995) presented the Concrete Capacity Design (CCD) method. The CCD method is a more transparent and user-friendly version of the κ method. Since then, the CCD method has been incorporated into many design codes and standards with ACI 318 and CSA A23.3, the concrete structural design codes and standards for the United States and Canada, being the most relevant to this report. The CCD method was introduced in CSA A23.3-04. Since then, it has gone from being an informative clause (2004, 2014) to a normative clause as of the 2019 edition. Minor adjustments have been made to methods proposed by Fuchs et al. (1995), but these equations have gone largely unchanged.

In its most recent edition, CSA A23.3:19 provides guidelines for the design of anchorage to concrete subjected to shear, tension, and combined shear/tension cases. Provisions of Annex D apply to a wide variety of anchorages, one of which is headed studs. The standard

provides factors to account for the anchorage location, the number of anchors in a grouping, the nature of the applied load, and reinforcement that is typically present within concrete.

3.1 CSA A23.3:19 Design Provisions

While Annex D covers all anchor types, only equations relevant to embeds are discussed here. Discrepancies between equations in the standard and corresponding equations shown in Chapter 2 are identified and explained where possible to provide the reader with a more comprehensive understanding of Annex D provisions. ACI 318-19 is referred to regularly since their provisions with respect to headed anchors are nearly identical to those of A23.3:19, and their commentary more thorough.

3.1.1 Resistance Modification Factor, R

Every limit state equation in Annex D includes a resistance modification factor, *R*. This fac- tor accounts for the differences in design philosophy between Canadian Limit States Design (LSD) and Load Resistance Factor Design (LRFD) used in ACI 318-19, upon which Annex D is based. ACI 318-19 uses resistance factors that vary depending on the limit state, while Canadian LSD uses constant material and resistance factors regardless of limit state. A modification factor, *R*, is required to align the level of safety in CSA A23.3 with that of ACI 318 by adjusting the material reduction factor accordingly and is defined for a variety of cases in Table 3.1.

Table 3.1 – Resistance modification factor, *R* (adapted from CSA A23.3-19)

a) for an anchor governed by a ductile steel element		
Tension Loads		0.8
Shear Loads		0.75
b) for an anchor governed by a brittle steel element		
Tension Loads		0.70
Shear Loads		0.65
c) for an anchor governed by concrete breakout, side face blowout, pullout, or pryout		
	Condition A	Condition B
Shear Loads	1.15	1.00
Tension Loads	1.15	1.00
CIP headed studs, headed bolts, or hooked bolts	1.15	1.00
Post Installed Anchors	Various	

Conditions A and B are described in §D.5.3 (CSA, 2019):

> "Condition A applies where the potential concrete failure surfaces are crossed by supplementary reinforcement proportioned to tie the potential concrete fail- ure prism into the structural member except where pullout or pryout resistance governs. Condition B applies where such supplementary reinforcement is not provided or where pullout or pryout strength governs."

For concrete failure modes, CSA A23.3 offers a different *R* factor depending on whether the anchorage meets requirements of Condition A or B. Neither ACI 318 nor CSA A23.3 specify the level of supplementary reinforcement sufficient to adequately tie the potential failure cone to the member. ACI 318 mentions in its commentary that the 15% increase accounts for the increased deformation capacity of anchorages with supplementary reinforcement in close proximity. Larger ductility is associated with less severe reduction factors, so ACI 318 permits an increased factor when the potential for increased ductility exists. ACI 318 also suggests that the reinforcement layout should conform to that shown in Figures 3.1a and 3.1b. There are also more clearly defined situations for sufficient reinforcement anchorage, such as hairpin/hanger reinforcement or tieback bars.

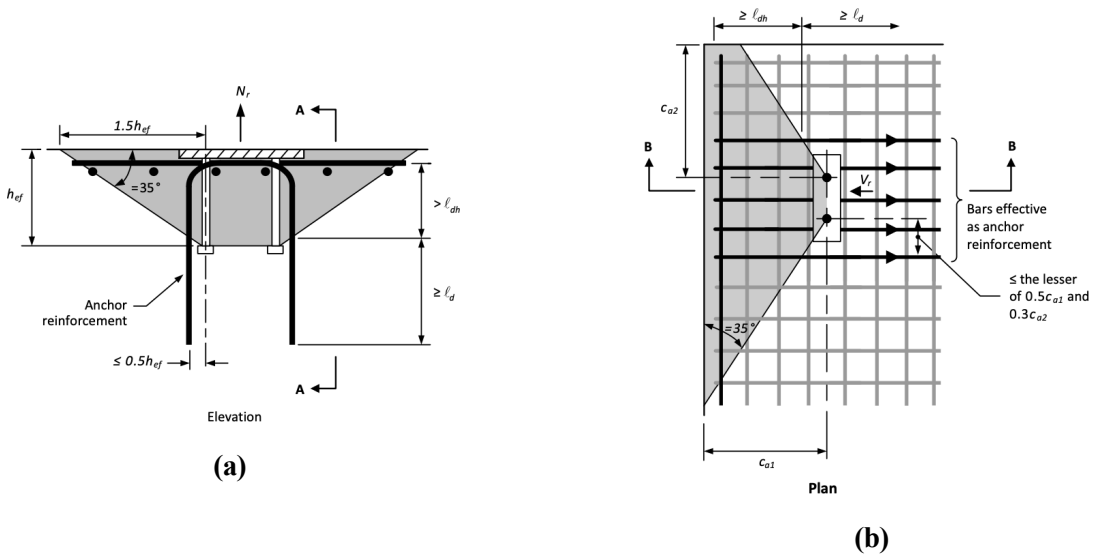

Figure 3.1 – Supplementary reinforcement for anchors loaded in (a) section view of tensile loading and (b) plan view of shear loading (CSA, 2019)

It is implied then that providing reinforcement within $0.5h_{ef}$ of an anchor for tension, or $0.5c_{a1}$ for shear, provides sufficient ductility to warrant a 15% increase in φ_c. Since informa- tion provided by Annex D is limited in this regard, designers consulted during this project said they would use Condition A to be conservative. One justification for this conserva- tive assumption is that there are tolerances and errors during construction regarding embed placement and it is impractical to assume that Condition A criteria are met when there is a chance that embed locations shift during construction. For this reason, Chin (2021) provided embed load tables for standardized plates where Condition B was assumed, so the load tables would be valid regardless of where the embed is located relative to the reinforcement.

3.1.2 5% Fractile

The 5% fractile is a concept applied to concrete failure modes in Annex D that ensures ca- pacities exceed the calculated resistance 95% of the time with a 90% confidence interval. The 50% fractile (i.e., mean) is converted to a 5% fractile as shown in Equation (3.1) (Rodriguez and Moehle, 2021).

$$N_{br,5\%} = N_{br,50\%}(1 - k_{st}\text{COV}) = N_{br,50\%}(1 - (1.65)(0.15)) = 0.75N_{br,50\%} \quad (3.1)$$

where k_{st} is a statistical parameter, summarized by Rodriguez and Moehle (2021), and COV is the coefficient of variation, taken as 15% for anchorage design (Fuchs et al., 1995). This

indicates that a 25% reduction in calculated capacity is sufficient to ensure that 95% of the time the true anchor capacity meets or exceeds the calculated capacity. The 5% fractile is applied independently of material resistance factors, meaning that A23.3:19 Annex D is conservative even when resistance factors are set to 1.0, which is not the case for many other expressions in the standard.

3.1.3 Steel Failure in Tension

The factored steel resistance of an anchor in tension, N_{sar}, is given by Equation (3.2) (§D.6.1.2).

$$N_{sar} = A_{se,N}\varphi_s f_{uta} R \tag{3.2}$$

where $A_{se,N}$ = effective cross-sectional area of the anchor in tension (mm^2), φ_s = material resistance factor for headed anchors (0.85), f_{uta} = specified tensile strength of anchor steel (MPa), and R = resistance modification factor.

For headed anchors loaded in tension, the effective cross-sectional area may be taken as the nominal area of the anchor. The specified tensile strength must be the lesser of 1.9 times the anchor steel yield strength and 860 MPa. The former limit is in place to prevent yielding at service loads, while the latter limit is in place since there is limited testing on anchors with tensile strengths exceeding 860 MPa (Chin, 2021).

3.1.4 Pullout Failure

The factored pullout capacity, N_{cpr} of a headed stud is given by Equation (3.3) (§D.6.3.4).

$$N_{cpr} = \Psi_{c,P} N_{pr} \tag{3.3}$$

$$\text{with } N_{pr} = 8 A_{brg} \varphi_c f_c^t R \tag{3.4}$$

where N_{pr} = factored pullout capacity of a single anchor loaded in tension in cracked con- crete (N), $\Psi_{c,P}$ = 1.4 where analysis indicates no cracking of the concrete member at service loads, and 1.0 otherwise, A_{brg} = bearing area of anchor head (mm^2), φ_c = material resistance factor for concrete (0.65), and f_c^t = concrete cylinder compressive strength (MPa).

A_{brg} is calculated as the total area of the anchor head minus the area of the stud shank, $\frac{\pi}{4}(d_h^2 - d^2)$. $\Psi_{c,P}$ is explained in §D.6.3.6 and addresses the difference in anchorage capacity in cracked versus uncracked concrete, where researchers found that pre-existing cracking causes a significant reduction in pullout capacity.

In Section 2.2.1.2, Equation (2.3) was presented for calculating pullout failures, but used a coefficient of 10 to 15 rather than 8. This coefficient comes from the significant increase in the compressive strength of the concrete just above the anchor head from localized confine- ment. Although research has shown that the peak compressive stress can be as high as 15 times f_c^t, Equation (3.4) places an upper limit of eight times the compressive stress on the bearing stress at the anchor head.

3.1.5 Concrete Side Face Blowout

The factored side-face blowout capacity, N_{sbr}, of a headed anchor close to an edge ($h_{ef} > 2.5c_{a1}$) is given by Equation (3.5) (§D.6.4.1).

$$N_{sbr} = 13.3c_{a1}\sqrt{A_{brg}}\varphi_c\lambda_a\sqrt{f_c^t}R \quad (3.5)$$

For an anchor group:

$$N_{sbgr} = \left(1 + \frac{s}{6c_{a1}}\right) N_{sbr} \quad (3.6)$$

where c_{a1} = minimum distance from centreline of anchor to edge of concrete (mm), λ_a = factor to account for concrete density, and s = distance between outer anchors in the group parallel to the concrete edge (mm).

Equation (3.5) bears resemblance to Equation (2.4), albeit with a lower leading coefficient and modifications to the exponents of c_{a1} and f_c^t. Specifically, Equation (3.5) is consistent with results from Furche and Eligehausen (1991), which have since been improved upon by multiple researchers (DeVries, 1996; Eligehausen et al., 2006).

Equation (3.6) modifies the blowout capacity of a single anchor for situations when two or more anchors are situated within $6c_{a1}$ of each other, parallel to the edge of concrete. No information is given in CSA A23.3 or ACI 318 as to the origin of this equation, but it seems to account for overlap in blowout failure surfaces.

3.1.6 Concrete Breakout in Tension

The factored concrete breakout capacity, N_{cbr}, of a headed stud is given by Equation (3.7) (§D.6.2.2).

$$N_{cbr} = \frac{A_{Nc}}{A_{Nco}} \Psi_{ed,N} \Psi_{c,N} \Psi_{cp,N} N_{br} \quad (3.7)$$

For a group of anchors, the capacity, N_{cgbr} is defined as:

$$N_{cgbr} = \frac{A_{Nc}}{A_{Nco}} \Psi_{ec,N} \Psi_{ed,N} \Psi_{c,N} \Psi_{cp,N} N_{cbr} \quad (3.8)$$

where N_{cbr} = factored concrete breakout resistance in tension of a single anchor in cracked concrete (N), A_{Nc} = area of projected breakout surface (mm^2), A_{Nco} = area of projected breakout surface ($9h_{ef}^2$) of a single anchor loaded in tension sufficiently far from any free edges (mm^2), $\Psi_{ec,N}$ = eccentricity modification factor for anchors loaded in tension, $\Psi_{ed,N}$ = edge distance modification factor for anchors loaded in tension, $\Psi_{c,N}$ = cracked concrete modification factor, and $\Psi_{cp,N}$ = post-installed anchor modification factor (taken as 1.0 for headed anchors). N_{cbr} is calculated in Equation (3.9).

$$N_{br} = k_c \varphi_c \lambda_a \sqrt{f'_c} h_{ef}^{1.5} \quad (3.9)$$

where k_c = 10 for headed anchors. k_c was taken as 16.8 in Chapter 2, which is the 50% frac- tile value from best-fit curves based on tests conducted in uncracked concrete (Fuchs et al., 1995), whereas A23.3:19 uses the 5% fractile resistance, and assumes that concrete is cracked.

Whether or not the concrete is cracked can have a significant effect on breakout strength. Eligehausen and Balogh (1995) analyzed 43 tensile tests on headed anchors loaded in ten- sion where crack inducers were placed in the concrete to ensure that the anchors were either intercepted by or very close to a crack. Concrete was cracked by preloading the specimen, and then anchors were loaded to failure. There was a decrease in breakout strength as crack widths increased. Since CSA A23.3:19 specifies crack width limits of approximately 0.3-0.4 mm for typical applications at service loads, it is sensible to consider a capacity re- duction associated with anchors located in cracked concrete. Eligehausen and Balogh (1995) found a reduction in capacity of ~25% when anchors were situated in cracks that ranged in width between 0.3 and 0.4 mm, in the same range as crack width limits under service loads.

It is reasonable to assume that cracks intercept anchors since anchors are discontinuities that cause stress concentrations. If anchors are located in the tension zone of a member, or where analysis suggests that the concrete is cracked, it is reasonable to assume that a crack will pass through a plane that intercepts the anchor.

k_c is modified (Equation (3.10)) to provide an equation for concrete breakout that con- servatively assumes the concrete is cracked and incorporates the 5% fractile:

$$k_{c,\text{cracked, 5\%}} = k_{c,\text{uncracked,mean}} \cdot 0.75 \cdot 0.75 \tag{3.10}$$
$$k_{c,\text{cracked, 5\%}} = 16.8 \cdot 0.75^2 = 9.45 \approx 10$$

Eccentricity Modification Factor ($\Psi_{ec,N}$)

In-plane eccentric loading of anchor groups causes some anchors to carry more load than others, which reduces the breakout capacity. This effect is accounted for using the eccentricity modification factor, $\Psi_{ec,N}$ (Equation (3.11))

$$\Psi_{ec,N} = \frac{1}{1 + \frac{2e'_N}{3h_{ef}}} \tag{3.11}$$

$$\text{with } e'_N \leq s/2$$

where e'_N is the distance between the centroid of the anchor group and the line of the applied load. Equation (3.11) accounts for the distribution of load for anchors participating in the tension resistance. Depending on the combination of loading on the anchorage, there may be some anchors that are not in tension. In this case only the anchors in tension should be considered in the calculation of $\Psi_{ec,N}$.

Edge Distance Modification Factor ($\Psi_{ed,N}$)

Anchors loaded in tension near a free edge parallel to the applied load experience a capacity reduction from the breakout cone being truncated by the free edge. Since the cone propagates from the head of the anchor at ~35° relative to the horizontal, this factor only affects capacity when the anchor is within $1.5h_{ef}$ of the free edge.

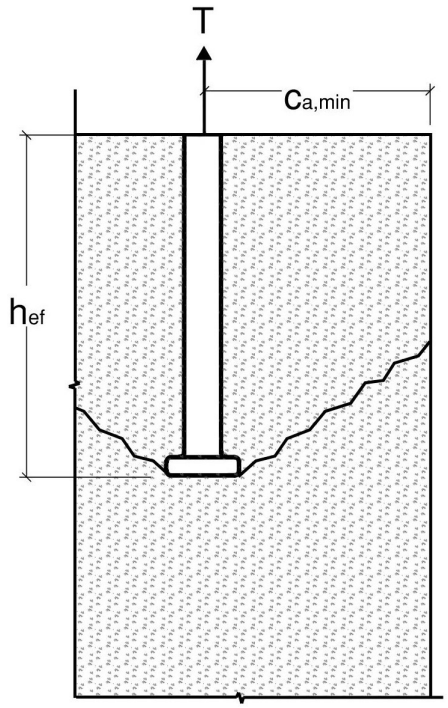

Figure 3.2 – Tension breakout cone truncated by a free edge.

$$\Psi_{ed,N} = \begin{cases} 1.0, & c_{a,min} \geq 1.5h_{ef} \\ 0.7 + 0.3\frac{c_{a,min}}{1.5h'_{ef}} & c_{a,min} < 1.5h_{ef} \end{cases} \quad (3.12)$$

where $c_{a,min}$ is the minimum distance from the centre of an anchor shaft to the concrete edge.

Cracked Concrete Modification Factor ($\Psi_{c,N}$)

When analysis indicates no cracking at service load levels, $\Psi_{c,N}$ may be taken as 1.25 for CIP anchors and 1.0 otherwise. Since Equation (3.9) assumes the concrete is cracked, and reduces the calculated capacity accordingly, A23.3 permits a 25% increase if the designer is certain that concrete is uncracked at service loads.

Post-Installed Anchor Modification Factor ($\Psi_{cp,N}$)

$\Psi_{cp,N}$ is 1.0 for CIP anchors. $\Psi_{cp,N}$ is only relevant for post-installed anchors that induce splitting forces, such as expansion anchors. In this case, anchors are assigned a modification factor of less than 1.0 to preclude potential splitting failures when the anchor is near a free edge.

3.1.7 Steel Failure in Shear

The steel shear capacity of an anchor is given in §D.7.1.2.

$$V_{sar} = A_{se,V} \varphi_s f_{uta} R \tag{3.13}$$

where $A_{se,V}$ is the effective cross-sectional area of the anchor in shear. Anderson and Mein- heit (2000) conducted 328 shear tests on headed anchors and found that when the nominal ultimate strength of the anchor is used, the effective cross-sectional area of the anchor may be taken as the cross-sectional area of the stud shank. This corresponds to $\alpha = 1.0$ as dis- cussed in Section 2.2.2.1. The nominal tensile strength of the anchor must be less than both
1.9 times the nominal yield strength and 860 MPa. Although the shear strength of steel is usually less than the tensile strength by a factor of $1/\sqrt{3}$ (≈ 0.58), effects of strain hardening are notable and accounted for here. Welded headed studs also experience local increases
in strength around the weld, which is beneficial because this is also the region where shear demand is largest. Lastly, the grade of steel used in headed studs (AWS Type B) typically has a larger ultimate strength than the minimum specified. As a result, CSA A23.3 permits designers to calculate the shear strength of a welded headed stud using the ultimate strength and full cross-section area.

In addition to the material reduction factor for steel, φ_s, of 0.85, the standard also specifies an R value of 0.75 for ductile steel elements, as discussed in Section 3.1.1. ACI 318 specifies a material reduction factor of 0.65 for this condition, which is approximately $0.85 \cdot 0.75$.

3.1.8 Concrete Pryout

The factored pryout resistance, V_{cpr} is given by Equation (3.14) (§D.7.3).

$$V_{cpr} = k_{cp}\, N_{cbr}\, R, \qquad k_{cp} = \begin{cases} 1.0 & h_{ef} < 65 \text{ mm} \\ 2.0 & h_{ef} \geq 65 \text{ mm} \end{cases} \tag{3.14}$$

with N_{cbr} determined by Equation (3.7). As discussed in Section 2.2.2.2, pryout resistance is also a function of anchor diameter (Ollgaard et al., 1971; Anderson and Meinheit, 2005; Jebara et al., 2016). CSA S16:19, the Canadian design standard for steel structures, uses the equation provided by Ollgaard et al. (1971) that accounts for the stud area when calculating capacities of shear connectors in composite beams with solid slabs. However, A23.3:19 Annex

D continues to use Equation (3.14), which is some multiple of the tension breakout strength. For concrete pryout, A23.3 specifies an *R* factor of 1.15 and 1.00 for Condition A and B, respectively.

3.1.9 Concrete Breakout in Shear

The factored concrete breakout capacity, V_{cbr}, of a single headed studs is given by Equa- tion (3.15) (§D.7.2.1).

$$V_{cbr} = \frac{A_{Vc}}{A_{Vco}} \Psi_{ed,V} \Psi_{c,V} \Psi_{h,V} V_{br} \tag{3.15}$$

For a group of headed studs, the capacity, V_{cbgr}, is given by Equation (3.16):

$$V_{cgbr} = \frac{A_{Vc}}{A_{Vco}} \Psi_{ec,V} \Psi_{ed,V} \Psi_{c,V} \Psi_{h,V} V_{cbr} \tag{3.16}$$

where V_{cbr} = factored concrete breakout resistance of a single anchor loaded in shear (N), A_{Vc} = area of projected breakout surface (mm^2), A_{Vco} = area of projected breakout surface ($4.5c_{a1}^2$) of single anchor in member with depth and edges perpendicular to the applied load no smaller than $1.5c_{a1}$ (mm^2), $\Psi_{ec,V}$ = eccentricity modification factor for anchors loaded in shear, $\Psi_{ed,V}$ = edge distance modification factor for anchors loaded in shear, $\Psi_{c,V}$ = cracked concrete modification factor, and $\Psi_{h,V}$ = shallow member modification factor.

The only difference between single anchor and multiple anchor capacities is the eccentricity modification factor, $\Psi_{ec,V}$, that is only present for anchor groups because it is impractical to load a single anchor eccentrically.

The factored concrete breakout capacity of an anchor in cracked concrete, V_{br}, is given by Equation (3.17) (§D.7.2.2).

$$V_{br} \leq \begin{matrix} 0.58 \frac{l_e}{d_a} \sqrt{d_a} \varphi_c \lambda_a \sqrt{f'_c} c_{a1}^{1.5} R \\ 3.75 \lambda_a \varphi_c \sqrt{f'_c} c_{a1}^{1.5} R \end{matrix} \tag{3.17}$$

Once again, there is a difference between Equation (3.17) and what was shown in Sec- tion 2.2.2.3 for calculating shear breakout strength (Equation (2.9)). Annex D uses a coef- ficient of 0.58, while Equation (2.9) uses a coefficient of 1.0. Equation (3.17) accounts for the effects of cracked concrete and the 5% fractile adjustment. Each of these applies a 25%

reduction to the anchor capacity.

$$k_{v,\ \text{cracked, 5\%}} = k_{v,\ \text{uncracked, mean}} \cdot 0.75 \cdot 0.75 \tag{3.18}$$
$$k_{v,\ \text{cracked, 5\%}} = 1.0 \cdot 0.75^2 = 0.56 \approx 0.58$$

These values are not identical, likely since the reduction in capacity due to the concrete being cracked varies with crack width. For crack widths of 0.3-0.4 mm, the maximum permitted under service loads, the reduction is ~25%, but it is unknown what amount of cracking was assumed at the time of implementation into the standard. There are stricter crack width limits for prestressed concrete, and architectural concrete, which may justify more lenient reduction in breakout strength, although CSA A23.3:19 does not permit such leniency.

The latter portion of Equation (3.17) imposes an upper limit on anchor diameter effect on capacity. Tests by Eligehausen and Hofmann (2003) showed that for anchor diameters of 25 mm or greater, Equation (3.17) overestimates the anchor diameter contribution to capacity. Lee et al. (2010) conducted 25 shear breakout tests on anchors with diameters ranging from 63.5 to 88.9 mm at an edge distance of 508 mm and confirmed that the CCD method, along with other compared methods, overestimated the capacity by approximately double for these test conditions. This is likely because CCD expressions were calibrated from tests with < 25 mm diameter anchors. However, this limit is not typically a concern in the context of embeds since it is uncommon to see anchors of that size in building construction. If the steel shear strength of an embed is insufficient, it is more sensible to weld additional studs to the baseplate.

Annex D provides one more breakout equation relevant to embeds. §D.7.2.3 states that rather than using 0.58 in Equation (3.17), 0.66 may be used if the headed stud is welded to a steel attachment with a thickness equal to the greater 10 mm or half the anchor diameter (CSA, 2019). ACI 318-19 attributes this increase to the stiffness of the welded connec- tion "clamping" the anchor more effectively. Although ACI 318-19 refers to Shaikh and Yi (1985) in the commentary, this paper makes no reference of the differences in concrete breakout strength between cast-in-place and post-installed anchors. From this, the author is unsure of the origin of this additional clause permitting an increase in capacity that applies to headed studs welded to baseplates.

Thin Member Modification Factor ($\Psi_{h,V}$)

As described by Eligehausen et al. (2006), Zhao et al. (1989) conducted tests on anchors in thin members ($h_a < 1.5c_{a1}$) and found that when the breakout cone is truncated by the bottom surface of the member, Equation (2.13) underpredicts the capacity. Therefore, Zhao and Eligehausen (1992) proposed the following modification factor, $\Psi_{h,V}$.

$$\Psi_{h,V} = \frac{\left(1.5c_{a1}\right)^{1/3}}{h_a} \geq 1.0 \tag{3.19}$$

Eligehausen et al. (2006) showed that Equation (3.19) was still conservative compared to tests (Figure 3.3) and proposed Equation (3.20), which has the same form, but modifies the exponent from one-third to one-half. Equation (3.20) is what can be found in §D.7.2.8. $\Psi_{h,V}$ must always be greater than one.

$$\Psi_{h,V} = \frac{\left(1.5c_{a1}\right)^{1/2}}{h_a} \geq 1.0 \tag{3.20}$$

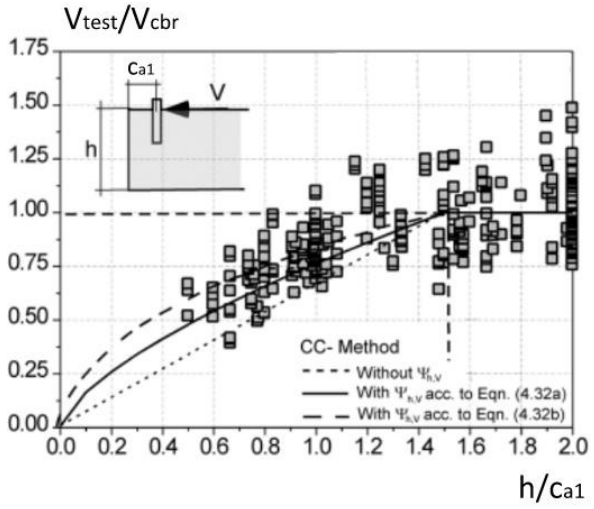

Figure 3.3 – Influence of member thickness on shear capacity (adapted from Eligehausen et al. (2006))

Cracking Modification Factor ($\Psi_{c,V}$)

ACI 318-19 and A23.3:19 provisions assume that concrete is cracked and accounts for the associated reduction in capacity. However, when concrete is uncracked, capacity may be increased accordingly. Several researchers at the University of Stuttgart conducted tests

on both precast and post-installed anchors. Although certain types of post-installed an- chors are of greater interest due to the additional splitting forces they generate, Eligehausen and Balogh (1995) conducted 43 tension breakout tests on headed studs and 362 on under- cut anchors with embedment depths ranging from 40 to 200 mm in concrete with 0.3 mm crack widths and found that the capacity was approximately 75% of the uncracked con- crete breakout capacity. Since A23.3:19 service level crack control requirements correspond to crack widths of 0.3 to 0.4 mm for reinforced concrete (RC), these tests results suggest that at the permissible crack widths, headed anchors have less than 75% of the uncracked capacity. However, there are situations where the capacity may be even lower. Eligehausen and Balogh (1995) suggest that anchors located in two perpendicular cracks (possible in two way slabs) or anchors located in the tension region of flexural members with low ratios of embedment depth to member depth may have capacities as low as 60% of the uncracked concrete breakout strength. In light of this, $\Psi_{c,V}$ is defined by CSA (2019) as follows: if analysis including shrinkage and temperature effects indicates no cracking at service loads, $\Psi_{c,V}$ may be taken as 1.4, meaning that the uncracked concrete strength is 40% larger than the cracked strength. Alternatively, if concrete is expected to be cracked at service load, the value of $\Psi_{c,V}$ is dependent on the reinforcement layout near the anchor. $\Psi_{c,V}$ then may equal:

- 1.0 for anchors in cracked concrete without supplementary reinforcement or with edge reinforcement smaller than a 15M bar
- 1.2 for anchors in cracked concrete with reinforcement of a 15M bar or greater between the anchor and the edge
- 1.4 for anchors in cracked concrete with reinforcement of a 15M bar or greater between the anchor and the edge and with the reinforcement enclosed within stirrups spaced not more than 100 mm apart

This factor does not suggest that the presence of reinforcement in the layouts described is directly providing additional capacity to the anchorage. Rather, this reinforcement is considered sufficient to prevent further crack growth that would normally be detrimental if concrete were unreinforced.

Eccentric Loading Modification Factor ($\Psi_{ec,V}$)

There are instances in design or construction where it is not practical or possible to ap- ply shear concentrically to an anchor group. In this case, uneven distribution of forces to anchors must be taken into account. The accepted method of accounting for the uneven distribution of forces is from an extension of the κ method proposed by Riemann (1985), using Equation (3.21).

$$\Psi_{ec,V} = \frac{1}{1 + \frac{2e_V}{3c_{a1}}} \leq 1.0 \tag{3.21}$$

where $\Psi_{ec,V}$ = eccentric loading modification factor and e_V = eccentricity of applied shear load relative to centroid of the anchors.

Equation (3.21) does not apply if loading is applied at an eccentricity larger than half of the total fixture length. At larger eccentricities, anchor groups must resist moments from the eccentric load with a tension-compression couple, which is not properly accounted for in Equation (3.21).

Edge Effect Modification Factor ($\Psi_{ed,V}$)

When anchors are near two free edges, the breakout cone will be further truncated by the edge that is parallel to the applied shear load (Figure 3.4). The capacity reduction can be accounted for by Equation (3.22), and only applies when $c_{a2} < 1.5c_{a1}$.

$$\Psi_{ed,V} = 0.7 + 0.3 \frac{c_{a2}}{1.5c_{a1}} \tag{3.22}$$

where $\Psi_{ed,V}$ = edge effect modification factor and c_{a2} = distance from centreline of anchor to edge that is perpendicular to c_{a1}.

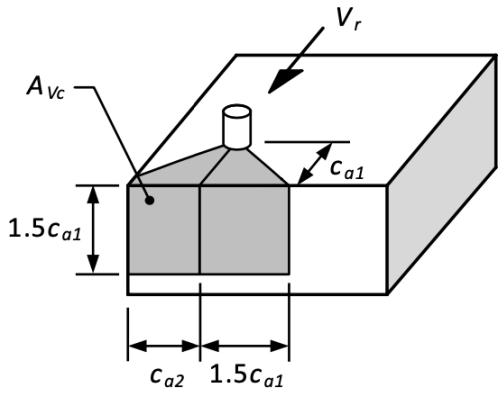

Figure 3.4 – Projected failure area for an anchor near a corner of a member with $c_{a2} < 1.5c_{a1}$ (CSA, 2019)

3.2 Tension Shear Interaction

The behaviour of anchors subject to simultaneous tension and shear is especially complex since any of the previously discussed shear or tension failure modes are possible, and it is possible for these failure modes to combine. For example, the anchor steel may rupture from a combination of tension and shear stress, or concrete could experience a combination of tension and shear breakout (Eligehausen et al., 2006). Combined shear and tension tests are generally conducted by applying shear and tension simultaneously via an inclined load (Figure 3.5).

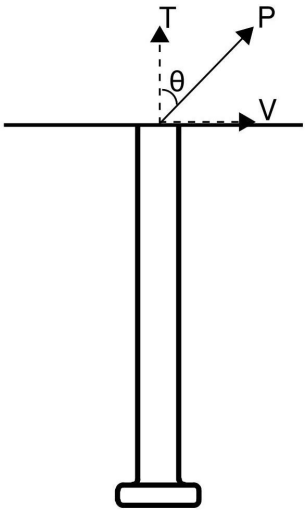

Figure 3.5 – Combined shear (V) and tension (T) load applied to a single anchor resulting from an inclined force (P).

In any case, the capacity of an anchor under combined loading is treated by Annex D using the following interaction equation.

$$\frac{N_f}{N_r} + \frac{V_f}{V_r} \leq 1.2 \tag{3.23}$$

where N_f and V_f are the factored tensile and shear loads, and N_r and V_r are the factored tensile and shear resistances of the anchor, respectively. Additionally, when $N_f/N_r \leq 0.2$ or $V_f/V_r \leq 0.2$, this interaction does not need to be considered. This trilinear interaction equation was proposed by Bode and Roik (1987) as a simplified alternative to the more accurate but cumbersome, Equation (3.24).

$$\left(\frac{N_f}{N_r}\right)^k + \left(\frac{V_f}{V_r}\right)^k \leq 1.0 \tag{3.24}$$

The value of k depends on the type of shear and tension failure mode. k ranges from 1 (linear interaction) to 2 (circular interaction). For steel anchor failure, $k = 2.0$ best approximates test data, while anchors that fail by breakout in both tension and shear are best approximated by $k = 1.2$ (Eligehausen et al., 2006). Alternatively, when test data is considered independent of failure mode, $k = 1.5$ has the most reasonable agreement, though with large scatter (Figure 3.6a). Figure 3.6b shows that when the 5% fractile adjustment is applied, Equation (3.24) provides a conservative estimate of the anchorage capacity.

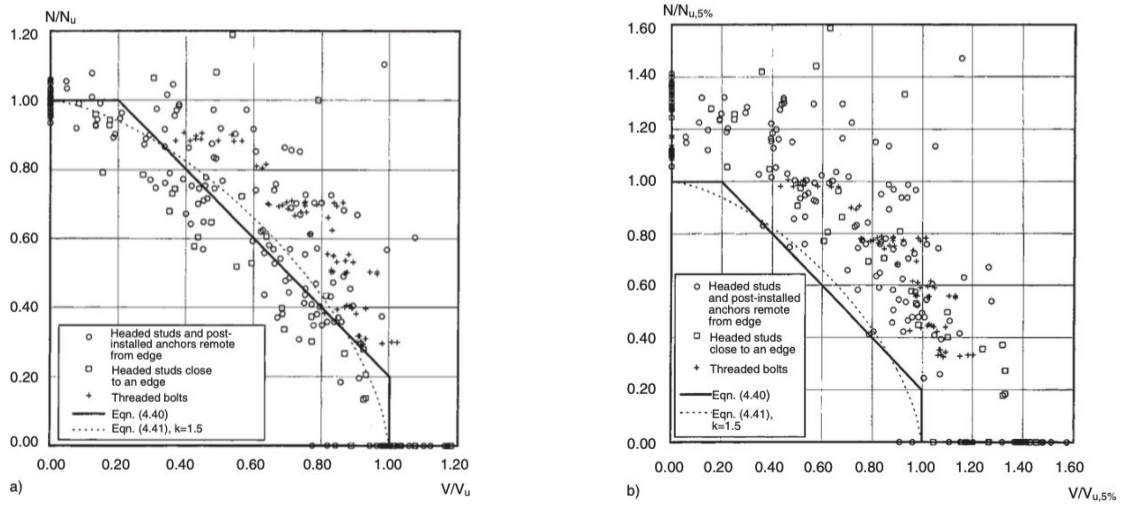

(a) **(b)**

Figure 3.6 – Trilinear interaction curve, and interaction curve with $k = 1.5$ plotted against (a) single anchor test data and (b) the same data adjusted for the 5% fractile (Eligehausen et al., 2006)

Despite showing both the trilinear interaction curve and an elliptic curve with $k = 5/3$, §D.8 explicitly permits use of the trilinear interaction curve, while also referring readers to §D.5.1.4 which states that designers may use any interaction expression provided it is in substantial agreement with test results. This is not necessarily the case with $k = 5/3$ since it is more or less accurate depending on failure mode.

3.3 Limitations in Annex D

This chapter summarizes provisions of CSA A23.3:19 Annex D as they apply to cast-in- place anchors and embeds. Where possible, research outcomes from Chapter 2 were linked to provisions in the standard. Much of the discussion around concrete breakout focuses on the CCD method and its use. A limitation of the CCD method is that it is based on empirical results from tests in unreinforced concrete. The CCD method is unable to quan- titatively account for reinforcement and the effect it has on anchorage strength, resulting in conservative, though inaccurate, estimates of anchorage capacity in even modestly rein- forced concrete. More recently, researchers have began looking at this problem, and have been working to better quantify anchorage capacities in RC, but there is still work to be done.

Another gap in Annex D is the treatment of combined loading. Annex D provides in- teraction equations valid for concentric tension and shear loads on single anchors and anchor groups, but there is no guidance given for the interaction of these forces with out-of-plane moments. Annex D provides Ψ factors to account for torque on anchor groups, but out-of- plane moments and the resulting distribution of forces on studs in an anchor group are not mentioned. Designers are left to their own devices insofar as determining how forces and moments interact, and the reduction in capacity that results.

4 Additional Considerations for the Design of Embedded Plates

4.1 Behaviour of Embedded Plates in Reinforced Con- crete

Anchorage tests in reinforced concrete routinely show that reinforcement near an anchor can increase both the ultimate and deformation capacities of the anchorage. Conversely, one of the key limitations of Annex D is that the provisions are based on the strength of anchors in unreinforced concrete. That said, there are situations where A23.3:19 permits reinforcement capacity to be substituted for concrete breakout capacity. For example, hairpin or hanger reinforcement can be detailed to fully develop within the breakout body, in which case Annex D permits the capacity of those bars to be used (Figure 4.1) in lieu of the concrete breakout strength.

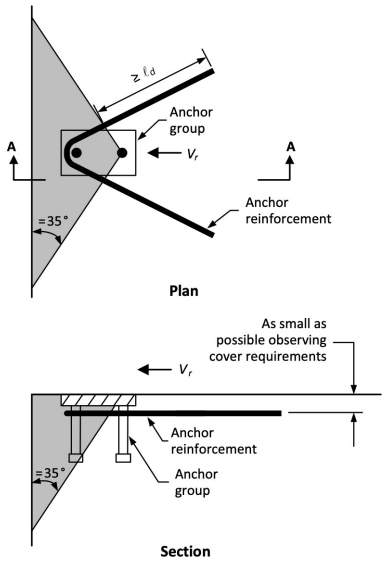

Figure 4.1 – Hanger reinforcement for shear loads permitted by Annex D (CSA, 2019)

Alternatively, a more general reinforcement layout may also be substituted for concrete breakout strength; however, only certain bars that meet strict proximity criteria may be

considered effective in resisting shear loads (Figure 4.2). Specifically, only bars that are within half of the edge distance to the nearest anchor ($0.5c_{a1}$) and are fully developed in both the breakout body and the member can be considered.

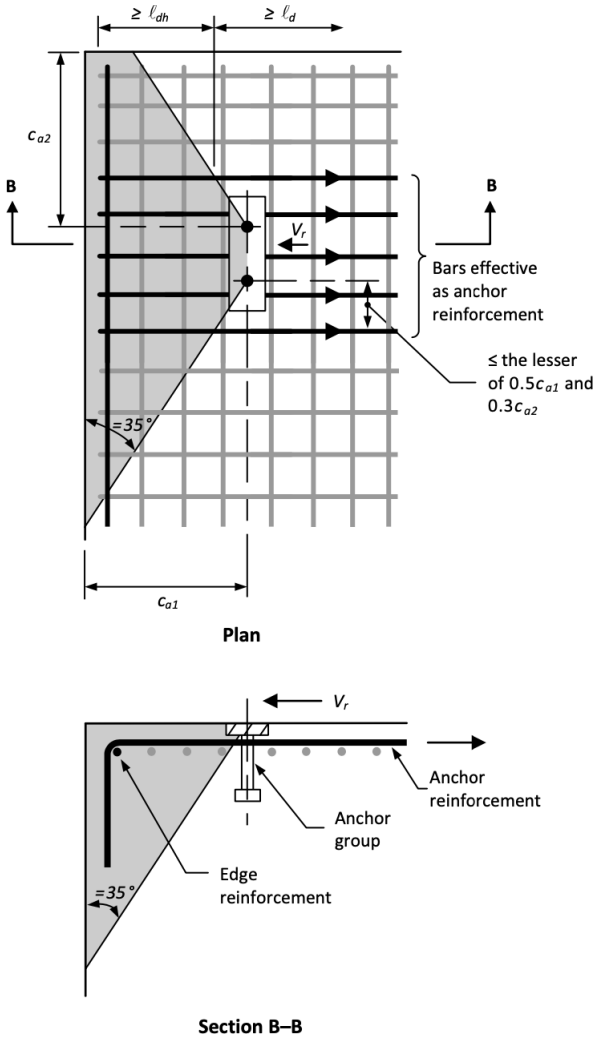

Figure 4.2 – Proximity requirements for bars to be considered effective in resisting shear load (bar is in tension) (CSA, 2019)

Currently, breakout capacity is limited to the greater of concrete breakout or reinforcement capacity. The standard makes no mention of reinforcement that is within the breakout body but does not meet development length or proximity requirements shown in Figure 4.2. Sharma et al. (2017b) provided further discussion of tests presented in their earlier paper (Sharma et al., 2017a), indicating that bars further than $0.5c_{a1}$ from an anchor can pick up load, even to the point of yielding. EN1992-4, the European code for the design of fastenings

in concrete, currently considers bars within $0.75c_{a1}$ of an anchor to be effective at resisting load (CEN, 2019). The intent of these limits is to provide assurances that the reinforcement being considered is close enough to the anchorage to be well anchored, in addition to the requirements that reinforcement be fully developed.

Although standards only acknowledge reinforcement that is generally parallel to the applied load, even surface reinforcement intended for serviceability requirements, such as mitigating temperature and shrinkage cracking, can have a considerable effect on anchorage behaviour. Nilsson et al. (2011) tested single anchors loaded in tension with and without surface rein- forcement (ρ = 0% to 1.2%) and found that the presence of surface reinforcement resulted in increases in capacity from the code predictions of 23% to 54% in pre-cracked concrete. In uncracked concrete, when the capacity was not limited by the flexural strength of the member, the code predictions were exceeded by 14%. While this may be reassuring from an Ultimate Limit States (ULS) perspective, the deformation required to engage reinforcement in dowel and/or catenary action occurs well past the point that the connection would be considered to have failed. In fact, Nilsson et al. (2011) mention that the more heavily rein- forced specimen had a lower capacity than the more lightly reinforced specimen in cracked concrete and attributed this to the larger deformations that were seen in the latter test. This suggests that crack width limits govern design long before surface reinforcement is engaged to resist load.

Chin (2021) conducted eight shear tests on four- and six- stud embeds with front stud edge distances ranging from 75 to 250 mm in lightly reinforced concrete (longitudinal 10M bars with a 250 or 300 mm spacing and one transverse 15M bar at the top and bottom of the 400 mm deep block around the perimeter). The test setup included a loading arm bolted directly to an embed shear tab and the loading arm was pinned to a hydraulic jack. The jack was supported at both ends, preventing rotation of the jack and to some extent the loading arm and embed, discussed later (Figure 4.3). Chin (2021) compared test results to Equation (2.9), the concrete breakout resistance provided by A23.3:19, and reported test- to-predicted ratios from 1.55 to 1.91, with a mean of 1.74. If material resistance factors for concrete were included, test-to-predicted ratios would be 2.68 and 1.71 for the 5% fractile and mean predictions, respectively. Compared to Equation (2.9) from the CCD method, which

uses the mean equation most accurately predicts breakout strength, the test-to-predicted ratio was 1.11. This suggests that for relatively lightly reinforced concrete, Equation (2.9) provides a reasonable and conservative estimate of shear capacity. However, to produce a conservative test-to-predicted ratio the reduction in capacity due to eccentricity of the shear load needed to be considered, otherwise the test-to-predicted ratio is a slightly unconserva- tive 0.92. It is unclear if the reduction in capacity calculated from the eccentric shear load is accurate in this case, where the rigidity of the loading arm limited the negative effects of the eccentric shear load. The consideration of eccentric loading requires further investigation, and is discussed in Section 4.2.

Load displacement curves from Chin (2021) show that peak load occurs after a significant loss in stiffness takes place. The loss of stiffness typically correlated to the point where cracks first propagated to the edge of the concrete, after which the load redistributed to reinforcement. It follows that an increase in reinforcement density would likely result in an increase in capacity. In the context of shear reinforcement, density can be increased in two ways: decreasing bar spacing and/or increasing bar size.

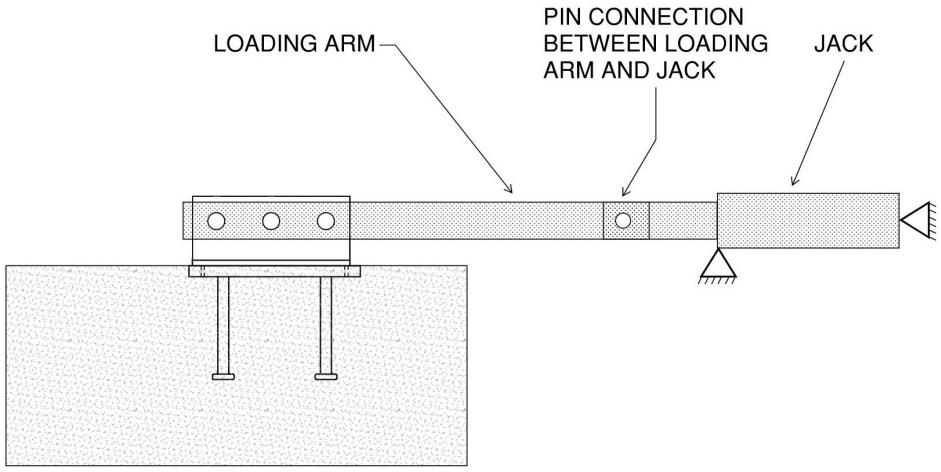

Figure 4.3 – Depiction of the test setup used by Chin (2021). Note the pin supports at the front and back of the jack.

Sharma et al. (2017a) investigated effects of increasing reinforcement density on the capacity of embeds subjected to shear loads towards a free edge. Tests were conducted with embeds at an edge distance to the back anchors, $c_{a1,n}$, ranging from 85 to 535 mm, and a constant

stirrup spacing of 200 mm, while stirrups diameters varied between 12 and 16 mm stirrups as well as 12 and 16 mm bundled stirrups, or no stirrups at all. Strain gauges were placed on reinforcement where the predicted concrete breakout cracks were expected to cross reinforce- ment. Strains were converted to equivalent bar forces, and the total load in the reinforcement was compared to the anchorage capacity to assess the stirrup contribution. At peak loads, when the concrete was fully cracked (defined as the point where cracks fully propagated from the back row of anchors to the edge of the concrete member), reinforcement was responsible for around half of the anchorage capacity, suggesting that the concrete is still able to resist a large portion of load after cracking. This differs from unreinforced concrete, where concrete is no longer able to resist load shortly after breakout cones fully form. An important dis- tinction in this test program is that the researchers designed their test setup to ensure that a pure shear was applied, with no other effects present to affect anchorage behaviour. To do this the researchers provided uplift restraint on the loading arms to prevent rotation of the anchorage (Figure 4.4). Furthermore, the researchers had embeds fabricated with threaded holes in the baseplate so the loading arm could be bolted directly to the baseplate, meaning there was essentially zero eccentricity between the applied load and the top of concrete.

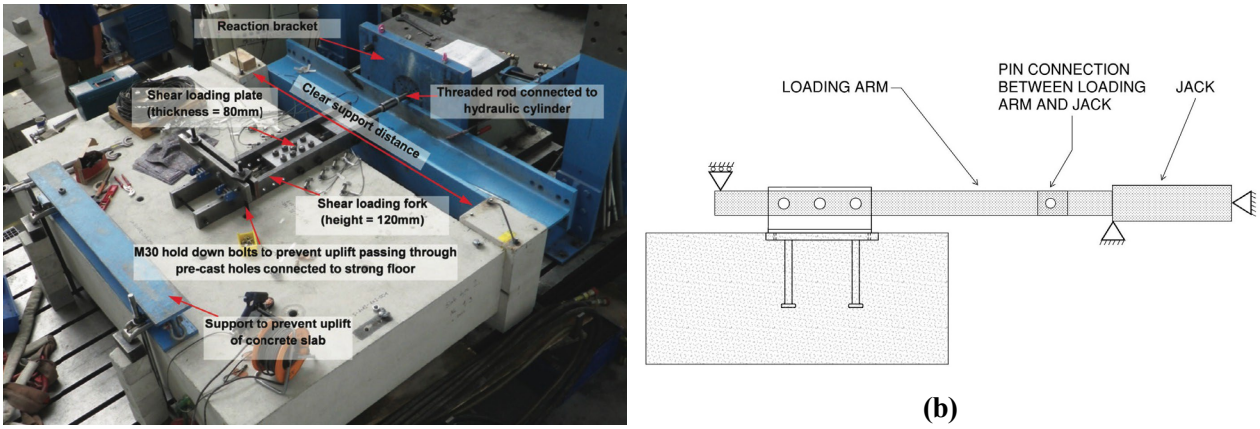

(a) **(b)**

Figure 4.4 – (a) Test setup used by Sharma et al. (2017a) (adapted from Sharma et al. (2017a)) and (b) illustration of test setup boundary conditions from Sharma et al. (2017a)

Sharma et al. (2017b) found that the peak load occurred at a point when the reinforcement closest to the anchors yielded, and that concrete still contributed an amount similar to the unreinforced concrete breakout capacity. However, they acknowledged that this was likely the

case because the setup included uplift restraint, which eliminates the tendency of embedded plates to pry out of the concrete under moment. This prying effect is best understood from Chin (2021). Despite the fact that Chin (2021) did not provide intentional uplift restraint, the bolted connection between the loading arm and the embed, paired with the support conditions on the jack shown in Figure 4.3, led to an appreciable amount of rotational restraint. The restraint was significant enough that in the final test of their program, the loading arm was yielded in flexure. Even in the tests where the loading arm did not yield, plate rotations of 0.01-0.02 rad at peak load were observed, suggesting that the tendency for embedded plates to pry out of the concrete under eccentric shear loading is significant and must be considered. In one of their tests, Sharma et al. (2017a) noted that the uplift

restraint failed, and this test had a lower peak load than the other tests with the same edge distance and reinforcement size (~575 kN versus ~725 kN), confirming the suspicion that the prevention of plate rotation under moment is beneficial to shear capacity.

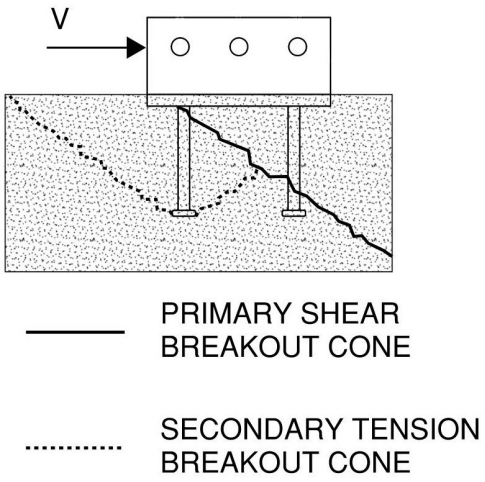

Figure 4.5 – Primary shear and secondary tension cracking due to the prying effect of an eccentric shear load (adapted from Sharma et al. (2017b))

Sharma et al. (2017a) noted that this effect requires further investigation, and theorized that without uplift restraint prying effects may result in a secondary breakout cone that may prevent concrete from carrying additional load after it forms (Figure 4.5). Although this is discussed further in Section 4.2, the concept is introduced here as it is relevant to the development of new models for predicting concrete breakout capacities of anchorages in reinforced concrete.

In a subsequent paper that presents a new model for calculating anchorage capacities, Sharma et al. (2018) seem to indicate that when uplift restraint is not present, the concrete is only able to provide around half of its breakout strength to the peak load. Short of one figure, there are no details provided in their paper to indicate that tests were conducted without uplift restraint to confirm this. However, given that research group's history studying an- chorage to concrete, it is possible that this equation was calibrated from previous test data. Eligehausen et al. (2019) later clarified that the presence of uplift restraint warrants the use of the full concrete breakout strength rather than half.

A number of researchers have noted that concrete is fully cracked and experiences a large reduction in stiffness at a displacement that is around half of what is required to reach the ultimate load (Sharma et al., 2017a, 2018; Chin, 2021). Beyond peak load, however, it was shown that even small amounts of reinforcement provide a significant increase in ductility, which is desirable at the ULS. This behaviour has been shown in a number of test pro- grams (Bui et al., 2018; Chin, 2021). Studies since the early 2000s have tried to identify how reinforcement affects embed capacity, although discussions have been qualitative until recently. To the author's knowledge, few studies have attempted to quantify the additional capacity typical reinforcement provides in addition to concrete breakout strength (Sharma et al., 2017a; Vita et al., 2019; Park et al., 2017).

Park et al. (2017) presented an alternative approach during their work on analyzing the effects of dynamic loading on anchors. They conducted shear tests on large diameter, single anchors, under monotonic and cyclic loading to assess their behaviour under seismic loading. Using results from the monotonic tests, Park et al. (2017) subtracted the nominal (calcu- lated) concrete breakout strength from the peak load, and divided the remainder by the total capacity of the reinforcement (adjusted for development lengths) to obtain a reinforcement efficiency, or contribution, factor, γ. The proposed formula for the shear resistance of an anchorage is shown in Equation (4.1).

$$V_r = V_{cgbr} + \gamma V_s \tag{4.1}$$

where V_s is the reinforcement shear resistance. From their tests, Park et al. (2017) found that γ = 0.68 gave reasonable estimates of anchorage capacity. Note that this value is based

on single anchor tests with little to no prying effects to consider and far larger anchor di- ameters and edge distances than what is usually found in typical buildings due to this work focusing on nuclear structures. Regardless, the same principle can be applied to multiple anchor groups with smaller diameter anchors by proposing a different γ value.

Sharma et al. (2018) also proposed equations to define concrete breakout strength of an- chors loaded in tension or shear in RC. Sharma et al. (2018) conducted 46 tests on embeds where strain in the reinforcing bars was measured and converted to an equivalent force. This force was subtracted from the applied load to determine the contribution from the concrete. After noting that concrete seemed to be resisting ~50% of the calculated concrete breakout strength at peak load, their proposed equation took the following form, adapted from the work of one of their doctoral students, K. Schmid:

$$V_r = \Psi V_s + 0.5 V_{cgbr} \tag{4.2}$$

where Ψ is a placeholder to account for a group of factors that modify V_s, (e.g., location factors, whether or not reinforcement around the embed yields). A detailed explanation of Sharma et al. (2018)'s model is presented in Section 4.1.1. Eligehausen et al. (2019) modified Equation (4.2) such that the 0.5 in front of V_{cgbr} can be changed from 0.5 to 1.0 if uplift restraint is present, while 0.5 is for a general case where there is no uplift restraint and tension breakout cones can form from the back studs (Figure 4.5)

Application of proposed equations by Park et al. (2017) and Sharma et al. (2018) in de- sign is relatively impractical. V_s is a summation of each reinforcing bar's contribution within the breakout cone, with each bar having its own modification factors to calculate. To apply these equations, the location of each reinforcing bar needs to be known in the design phase. Chin (2021) dedicated efforts to standardizing embed design and construction, with one of the impetuses for this work being that that there are often adjustments during construction that cannot be accounted for in design. Additionally, some designers feel Annex D is too complicated, if anything, and requiring designers to calculate individual contributions of each reinforcing bar is impractical.

What is lacking in literature is an effort to describe the behaviour of anchorages embedded in RC more generally. Much like shear design of concrete beams and slabs, it is perhaps more sensible to define anchorage capacity as a function of reinforcement area or spacing. In this manner, both the concrete resistance and reinforcement resistance can be more easily quantified. To the author's knowledge, only one research program has compared their results to these breakout models. Bujňák et al. (2019) presented results of six tension breakout tests on four stud embeds in RC with reinforcement layouts shown in Figure 4.6.

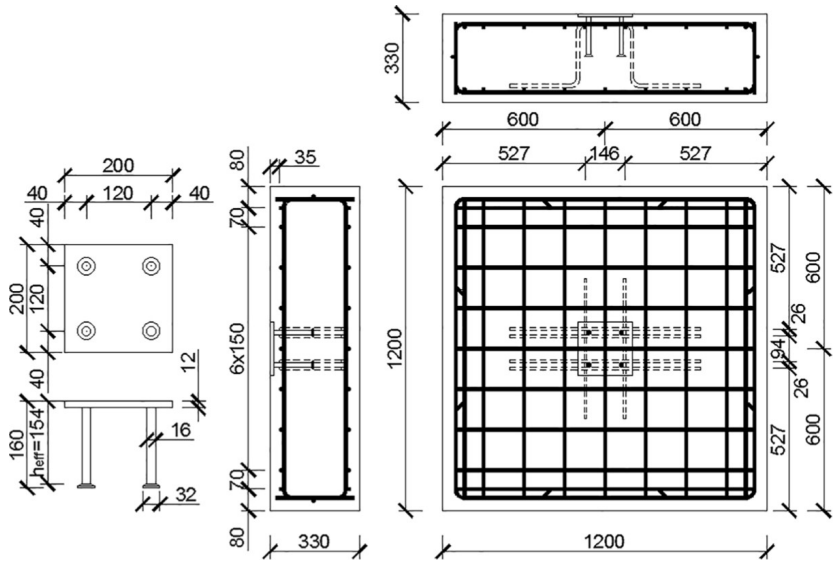

Figure 4.6 – Embedded plate design and reinforcement layout for tension tests conducted by Bujňák et al. (2019)

When comparing their test results to the equations presented by Sharma et al. (2018), they saw test-to-predicted ratios ranging from 0.99 to 1.05, suggesting excellent agreement in all cases. Supplementary reinforcement consisted of four hooked U-bars with a 10 mm diameter that were all within 13 mm of a stud (Figure 4.6). Without performing any calculations, it is reasonable to assume that the supplementary reinforcement is in such close proximity to the anchors that it is able to develop its yield strength. Additionally, the dense top mat of reinforcement is a variable that was not considered in their calculations of capacity. Bujňák et al. (2019) used 12 mm diameter bars at 150 mm on centre in both directions, which is sig- nificant enough to affect the behaviour of the tests based on the earlier discussion of Nilsson et al. (2011). Thus, though Sharma et al. (2018)'s expressions predicted capacity of these tests very well, the tests are not representative of the intent of these expressions, which is to

consider the influence of all reinforcement in the breakout body, not just those within prox- imity limits that are already used by North American design codes and standards. In this situation designers would likely just substitute the reinforcement capacity for the concrete breakout strength as permitted by CSA A23.3:19 rather than spend time working through these expressions.

In summary, although it is well recognized that reinforcement contributes to the load and deformation capacity of anchorages, there is still no practical method for designers to account for this effect reliably in design. To the author's knowledge, no research program has been conducted on embedded plates that directly evaluates the effect of varying reinforcement spacing, which is a limitation of proposed models. Until a wider array of reinforcement lay- outs are tested, it is difficult to say whether these equations are representative of the broader behaviour of anchors in RC.

4.1.1 Sharma et al. (2018) Reinforced Concrete Breakout Model

Sharma et al. (2018) presented the following equation to estimate the breakout capacity of an anchorage in RC.

$$V_r = 0.5V_{cgbr} + V_s \tag{4.3}$$

where V_r is the total breakout resistance, V_{cgbr} is the unreinforced concrete breakout resis- tance, which can be calculated using methods shown earlier in this report, and V_s is the reinforcement resistance. Equation (4.3) was initially presented without the factor of 0.5 in front of the concrete breakout strength. This has since been attributed to the uplift re- straint provided in the tests (i.e., the embed was unable to rotate as shear load was applied). Uplift restraint increases capacity via increased shear resistance in the concrete (i.e., less separation of the breakout cone from the specimen and smaller crack widths). Eligehausen et al. (2019) subsequently found that in tests without uplift restraint concrete contribution was around half of the concrete breakout resistance at peak load, hence the 50% reduction applied in Equation (4.3). As discussed in Section 4.2, it is clear that load eccentricity generates moment on the connection that plays a notable role in capacity.

Sharma et al. (2018) breaks down the reinforcement capacity into two components: the bond strength of the bars and the capacity of the hook. The capacity of a single bar is given as

$$N_{r,bar} = N_{r,hook} + N_{r,bond} \leq A_s F_y \tag{4.4}$$

The contribution of the hook, $N_{r,hook}$, is given as

$$N_{r,hook} = \Psi_1 \Psi_2 \Psi_3 A_s F_y \left(\frac{f'_{cc}}{30}\right)^{0.1} \tag{4.5}$$

where f'_{cc} is the concrete cube strength, assumed in these calculations to be to $f'_c/0.80$. Cylinder-to-cube strength ratios vary between 0.65 to 0.9 with the higher ratios usually belonging to higher strength concrete (Elwell and Fu, 1995). Ψ_1 considers the location of the stirrup. For the first bar(s) crossed by the breakout cone, usually closest to the embedded plate, Ψ_1 is 0.95. For subsequent bars, if the preceding bar yielded, Ψ_1 is 0.95. If the previous bar did not yield, it is 0.16. Ψ_2 considers the presence of edge reinforcement. This factor is
equivalent to $\Psi_{c,V}$ as presented in A23.3:19, and calculated in Equation (A.22)

$$\Psi_2 = \frac{\left(d_L\right)^{2/3}}{d_b} \leq 1.2 \tag{4.6}$$

where d_L is the diameter of the transverse or edge reinforcement and d_b is the diameter of the stirrup. Ψ_3 considers the influence of bond length, l_1, of the stirrup. Bond length is the length of the bar within the breakout body, which is the distance from the primary breakout cone crack to the edge of concrete, less clear cover.

$$\Psi_3 = \left(\frac{l_1}{c_{a1}}\right)^{0.4} \left(\frac{10}{d_b}\right)^{0.25} \tag{4.7}$$

The bond contribution of one stirrup is given as

$$N_{r,bond} = \frac{\pi d_b (l_1 - l_{1,min}) f_{bm}}{\alpha_2} \tag{4.8}$$

where $l_{1,min}$ is the minimum anchorage length of $4d_b$, f_{bm} is the bond stress, and α_2 is defined as

$$\alpha_2 = 1 - \frac{0.15(c_c - d_b)}{d_b} \tag{4.9}$$

where c_c is the clear cover. α_2 accounts for the influence of the clear cover on bond strength. The smaller the clear cover, the weaker the bond strength. The total resistance of all bars in the breakout body is then

$$N_r = \text{L} N_{r,bar} \quad (4.10)$$

N_r needs to be adjusted to account for the eccentricity of the applied loading. Sharma et al. (2018) provides Equation (4.11)

$$V_s = \frac{N_r}{x} \tag{4.11}$$

where V_r is the total shear resistance of the stirrups, and x is defined as

$$x = 1 + \frac{e_s}{z} \tag{4.12}$$

where e_s is the perpendicular distance between the reinforcement and the point of the applied load, and z is the internal lever arm of the concrete member, approximately equal to $0.85d'$. Here, d' is:

$$d' = min(d, 2h_{ef}, 2c_{a1}) \tag{4.13}$$

The internal lever arm concept is borrowed from EN1994-2, shown in Figure 4.7.

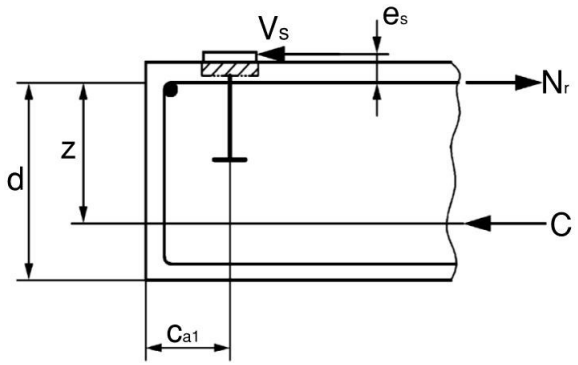

Figure 4.7 – Free body diagram offered by EN1994-2 (adapted from Sharma et al. (2017b))

$$\circlearrowleft M_C = 0 \rightarrow N_r z = V_s(z + e_s) \tag{4.14}$$

$$\therefore V_s = \frac{N_r}{1 + \frac{e_s}{z}} \tag{4.15}$$

$$\left\{ x \right\}$$

4.1.2 Park et al. (2017) Reinforced Concrete Breakout Model

Park et al. (2017, 2016) conducted five static and eight dynamic shear tests in cracked and uncracked concrete to evaluate the effects of seismic loading on large-diameter anchors

(d_s = 36 mm). After considering seismic effects, they turned their attention to anchor capacity and attempted to quantify it using Equation (4.16).

$$V_r = V_{cgbr} + \gamma V_s \tag{4.16}$$

γ is termed a contribution coefficient for the stirrups, calculated using Equation (4.17).

$$\gamma = \frac{V_{test} - V_{cgbr}}{V_{s,i}} \tag{4.17}$$

where V_{test} is the peak load from their experiments, and $V_{s,i}$ is the capacity of stirrup i, calculated using Equation (4.18)

$$V_{s,i} = A_s F_y \frac{(1.5c_{a1} - s_i)}{c_{a1}} \leq A_s F_y \tag{4.18}$$

where s_i is the perpendicular distance from the anchor to the stirrup. Calculating γ for each test, the authors found a mean value of $\kappa = 0.68$. Thus, Equation (4.16) takes the form

$$V_r = V_{cgbr} + 0.683 \sum V_{s,i} \tag{4.19}$$

For V_r to represent the 5% fractile, γ can be taken as 0.5.

4.1.3 Summary

Researchers have been working to quantify reinforcement contribution to fill the gaps in design codes and standards that neglect reinforcement contribution to breakout capacity. CSA A23.3:19 permits qualitative consideration of reinforcement and allows for the substi- tution of concrete breakout strength with reinforcement capacity. However, it is still overly conservative when 5% fractile expressions are used with the CCD approach, which assumes concrete is unreinforced. New methods that account for reinforcement capacity are cum- bersome in their application, and may be challenging to implement into design. However, these equations do have the potential to better predict capacity of anchorages in RC, though more testing is required to verify the expressions against embeds in a variety of reinforce- ment spacings/layouts. Properly accounting for the reinforcement capacity will make embed design more efficient in situations where the breakout strength is the governing limit state, allowing increased loads at smaller edge distances than what is currently permitted.

4.2 Effect of Moment Transfer into Embedded Plates

Embeds are a versatile means of connecting steel and concrete in structures. A common application for embeds is to provide end support for steel beams. It is common in this sit- uation to design the connection between the embed and the steel beam as a simple shear connection. Although simple shear connections such as shear tabs and double angles are often thought to transmit only shear from a beam to the supporting element, eccentricity of the applied load generates moment on the supporting member. This eccentricity affects the capacity of embeds by inducing tension in the most critical studs in the connection (Chin, 2021). Additionally, there is rotational demand on the connection caused by end rotation of the supported beam. For shear connections to be considered simple supports in design, the American Institute of Steel Construction (AISC) 360-16 structural steel design code for buildings requires that shear connections be designed to transmit less than 20% of the beam plastic moment capacity at a rotation of 0.02 rad (AISC, 2016b), meaning that even simple shear connections possess sufficient stiffness to transfer moment into the support.

A typical four stud embed resists applied moment, M_a, that comes from load eccentric- ity and end rotation with a tension compression force couple, as shown in Figure 4.8. Note that a key assumption in this strain diagram is that the baseplate is sufficiently stiff such that plane sections remain plane, and the strain distribution below the baseplate is linear.

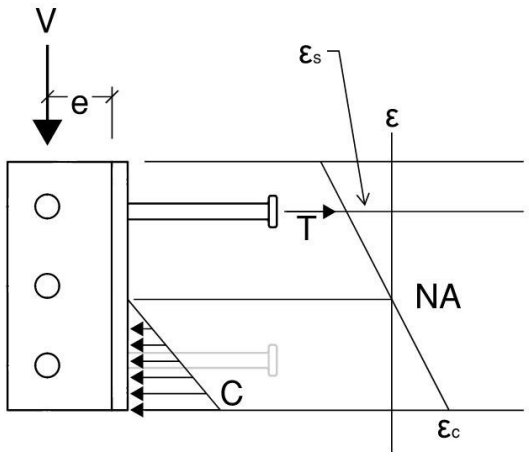

Figure 4.8 – Tension (T) and compression (C) force couple induced by an eccentric shear load (V) and corresponding linear strain diagram if the baseplate is assumed to be rigid.

It is common for designers to calculate the tensile force in the back studs, T, then use Equation (3.23) provided by CSA A23.3:19 for tension shear interactions to verify that the connection resistance is sufficient. However, since the tensile force in the back studs is a function of the applied shear, it is an iterative process to find the maximum shear, V_r, that the connection can resist.

If the anchor plate is sufficiently rigid such that there is no appreciable bending defor- mation, the tensile force in the critical studs can be determined using traditional flexural theory, where plane sections are assumed to remain plane (Figure 4.8). Analogous to RC beams, the back studs act as tensile reinforcement while at the opposite end of the plate that bears against the concrete is the compression block. Since the compressive stress is rel- atively small, less than 40% of the concrete compressive strength, a linear force distribution can be assumed. This assumption is more or less accurate depending on factors such as the plate thickness, the stiffness of the overall connection, and the failure mode. A shear tab that is continuously welded to the base plate is effectively a stiffener, while angles welded along their toe will contribute less stiffness to the baseplate. The rigid baseplate assumption should be used with caution, since it is unconservative with respect to the steel studs. The assumption of a rigid baseplate provides the largest possible moment arm to resist moment. If the baseplate deforms appreciably under moment the centroid of the compressive reaction moves towards the critical studs, reducing the moment arm and increasing the tensile stress in the studs.

Equation (3.23) should be used with caution for this application since its accuracy depends on tension and/or shear failure modes. Section 3.2 summarized the range of exponents that could be applied to Equation (3.24) which are more or less accurate depending on the failure mode. k values up to 2.0 are associated with steel failures, while $k = 1.2$ is more accurate when the failure modes in shear and tension are concrete breakout (Figure 4.9).

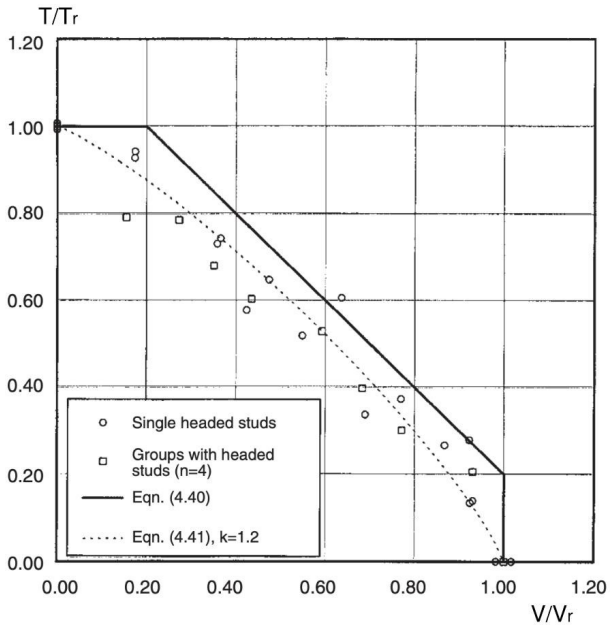

Figure 4.9 – Trilinear interaction curve, and interaction curve with $k = 1.2$ plotted against single and multiple anchor test data where the governing failure mode is concrete breakout in shear (adapted from Eligehausen et al. (2006))

This method fails to account for the stress distribution near critical anchors for certain types of loading. For embeds with closely spaced anchor rows subjected to bending moments, the tension breakout cone that forms from the critical studs intersects the compressive reaction at the other end of the embed (Figure 4.5). The compressive reaction partially confines the breakout cone, resulting in an increase in the tension capacity of the back row of anchors. As cited by Eligehausen et al. (2006), in an unpublished paper from 2003, Eligehausen and Fichtner proposed the following modification factor to account for the increase in tension breakout strength:

$$\Psi_{m,N} = \begin{array}{ll} 1.0 & z/h_{ef} \geq 1.5 \\ 2.5 - z/h_{ef} & z/h_{ef} \leq 1.5 \end{array} \tag{4.20}$$

where z is the perpendicular distance between the critical studs in tension and the centroid of the compression reaction. Tests from a number of authors are shown in Figure 4.10.

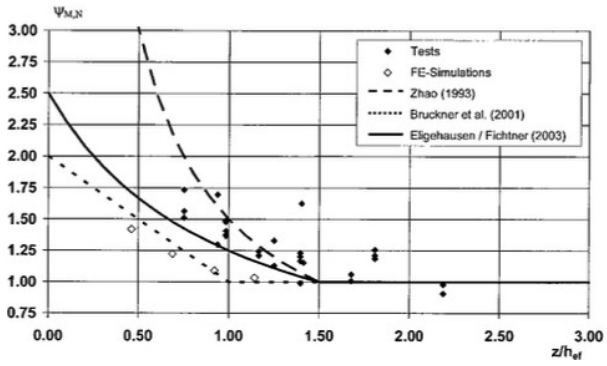

Figure 4.10 – Influence of baseplate compressive force on tension breakout capacity (adapted from Eligehausen et al. (2006))

Tests on anchorages with $z/h_ef \leq 1.5$ saw increases in capacity up to 75%, although finite element analyses show a less beneficial effect. For the purposes of implementation into EN1992-4, $\Psi_{m,N}$ has been proposed using the relationship shown in Equation (4.20).

4.2.1 Tension Shear Interaction

Anchors loaded in both shear and tension experience reductions in capacity due to the interaction of the tension and shear failure modes. The introduction of a tensile force to an anchor loaded in shear will reduce the shear capacity and vice versa. The behaviour of interaction loading is complex, and combinations of shear and tension failure modes can be expected. Interaction loads are most commonly dealt with by using an interaction equation, such as the tri-linear approach proposed by Bode and Roik (1987), shown in Figure 4.11.

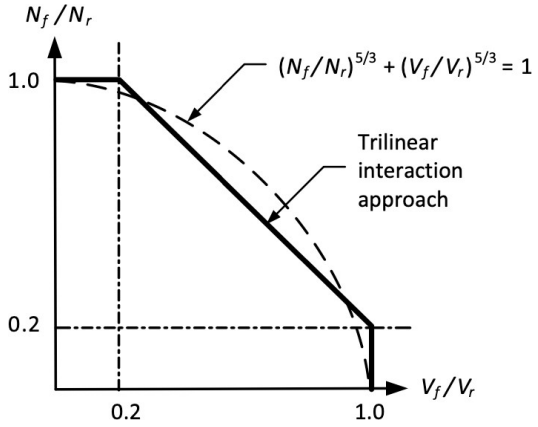

Figure 4.11 – Tension shear interaction diagram shown in CSA A23.3:19 that includes the trilinear interaction curve proposed by Bode and Roik (1987) (CSA (2019)).

The interaction equations in CSA A23.3:19 are based upon tests where the shear and tension was applied by loading the specimen through a range of angles from zero degrees (tension) to 90° (shear) and plotting the results. Eligehausen et al. (2006) recommends an equation of the following form.

$$\left(\frac{N_f}{N_r}\right)^k + \left(\frac{V_f}{V_r}\right)^k \leq 1$$

where k varies depending on the expected failure mode anchor type (e.g., precast or post- installed). CSA A23.3:19 provides the trilinear interaction curve discussed in Section 3.2 rather than elliptic curves, although it does permit the use of elliptic curves with any k provided it is in substantial agreement with test results.

In the context of shear on embeds, tensile forces come from two different effects. The first is from eccentricity in the connection. Typical shear connections will detail a bolt or weld line that is a non-zero distance from the face of the baseplate. Eccentric shear load induces a moment that is resisted by a tension compression couple in the embed. Tension can also come from partial fixity inherent in any connection. Although simple shear connections are typically considered to be simple supports (i.e., zero moment), this is an idealization. All connections are partially fixed with some amount of moment transferred to the support. Moment due to eccentricity of the applied load is unavoidable though designers can alleviate the moment transfer from partial fixity by uncoupling the rotation of the beam end from the rotation of the plate (i.e., provide a more flexible connection). This is often achieved using a double angle detail as opposed to a shear tab. The angles in the double angle connection are welded to the embedded plate along their toes, allowing the portion connected to the beam to flex away from the embed when the beam end rotates (Section 4.2.1). For simplicity, the total moment can be reported as a percentage of the bending moment on a uniformly loaded beam.

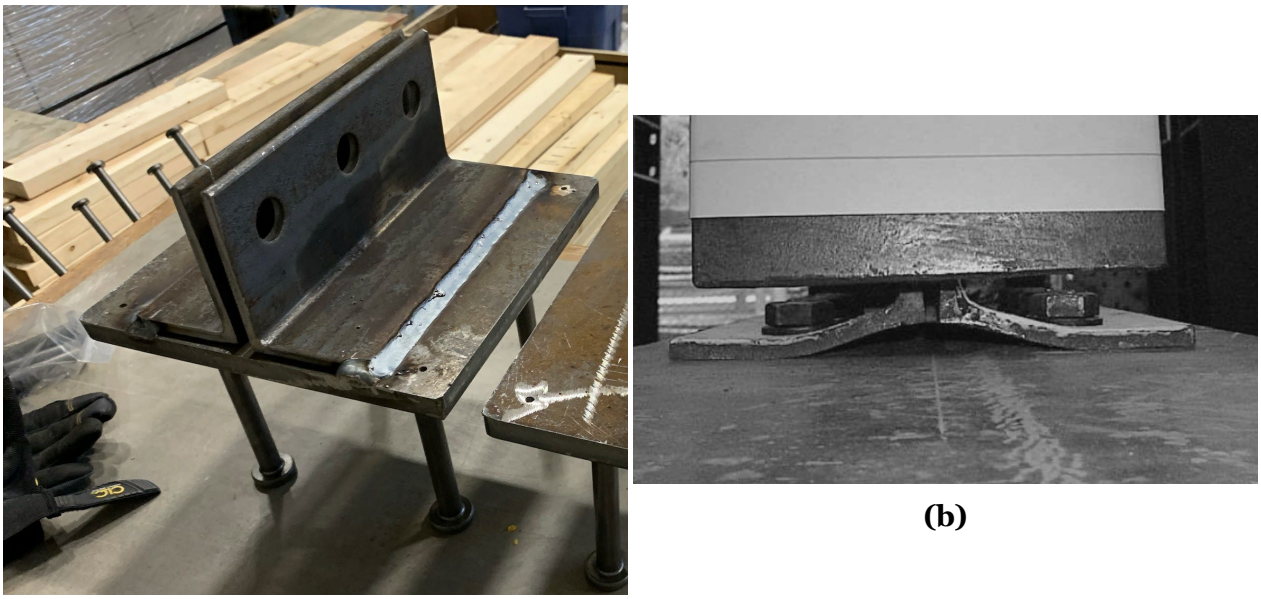

(a) **(b)**

Figure 4.12 – (a) Embed with angles welded to the baseplate along their toes, and (b) bolted double angle connection prying away from baseplate (adapted from Hong et al. (2002))

.

While there is a lack of research on embeds with simple shear connections, semi-rigid con- nections have been a heavily researched topic in the field of steel design over the last half century.

4.2.2 Semi-Rigid Connections

In structural design, it is common to see supports classified as simple or continuous. In prac- tice, all connections are somewhere between these extremes. Connections that easily rotate attract little moment and are classified as simple or pinned connections. Stiff connections attract larger moments due to their inability to rotate, and are classified as rigid or fixed connections. There are many connections lying between these two extremes that are referred to as intermediate, or partially restrained connections. A well known means of analyzing and classifying connection types is the beam-line method, proposed by Batho and Rowan (1934), and shown in Equation (4.21).

$$M = M^F - \frac{2EI\varphi}{L} \tag{4.21}$$

where M = moment in semi-rigid connection (Nm), M^F = fixed end moment (Nm), E = elastic modulus (N/m^2), I = beam moment of inertia (m^4), φ = angle of rotation of semi- rigid connection (rad), and L = beam length (m).

When the beam line given by Equation (4.21) is plotted over the moment rotation curve of a connection, the point where the two lines intersect represents the moment and rotation that can be expected from that connection type under the current conditions (Figure 4.13). In other words, the intersection point of the beam line and the moment rotation curve, P, is the equilibrium position for a given set of material and geometric parameters (E, I, L).

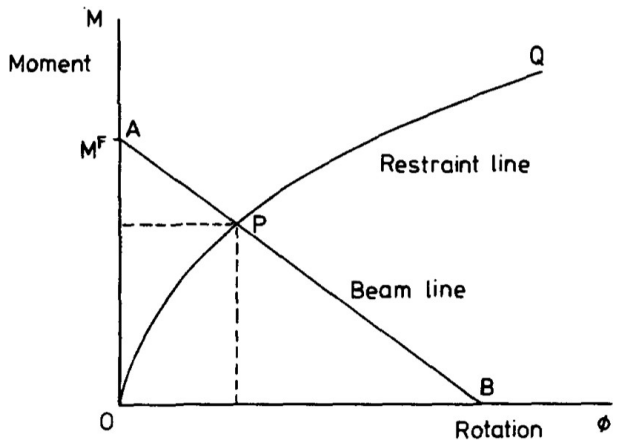

Figure 4.13 – Beam line AB and a typical moment rotation curve OQ (Jones et al., 1983). Point A is the maximum or fixed end moment, and point B is the rotation that would occur if the connection were a perfect pin

A simple or pinned connection would be represented by a perfectly horizontal restraint line emanating from the origin, while a fixed connection would be represented by a vertical line.

Beam lines are straightforward to determine. For a given system they are a function of the geometry and material. The fixed end moment (point A) and the simply supported end rotation (point B) can be determined using structural analysis. The moment rotation curve, or the restraint line, is more difficult to determine since the stiffness of the connection must be known beforehand. There are analytical and empirical means of achieving this. Richard et al. (1988) presented an analytical solution for the moment rotation behaviour of double angle connections and compared it to test data from other published results. This procedure

may be used to generate moment rotation curves for double angle connections with a variety of different angle leg lengths and thicknesses. Similar moment rotation curves also exist for different connection types such as shear tabs or single angles. Most of these are based on test results rather than analytical equations. Nethercot et al. (1998) proposed a system of classifying connection types that considers connections transmitting less than 20% of the beam's plastic moment capacity as simple, and over 70% as rigid. Shear tabs and double angles are both considered simple connections under this classification.

Morris and Packer (1987) summarized tests for a variety of connections, including shear tabs and double angle connections, indicating that both connection types are relatively flex- ible, but double angles exhibit superior flexibility and ductility. They reported that double angle connections only attract 5-15% of the total moment, and are able to rotate up to 0.08 rad prior to failure. In contrast, Astaneh et al. (1989) conducted five tests on three, five, and seven bolt shear tabs, finding that they were able to reach 0.05 rad of rotation prior to failure, consistent with AISC 341-16, the American seismic design code, which states that shear tabs are inherently stiffer than double angle connections (AISC, 2016a). Astaneh (1989) found that shear tabs reached yield plateaus at 0.02 rads, while double angles reached yield plateau much later, around 0.05 rad. Although both connections are simple shear connections, there are still notable differences in flexibility; however, both connection types meet the require- ment set out by AISC 360-16 that shear connections must accommodate the end rotation of a simply supported beam (AISC, 2016b). 0.03 rads is usually taken as the minimum permitted end rotation, approximately equal to the that of a simply supported beam at the plastic moment capacity under uniform loading with a span 24 times the depth (Muir and Thornton, 2011).

The stiffness of double angle connections is proportional to the square of the angle thick- ness (Morris and Packer, 1987). For this reason, designers may specify a maximum angle thickness when delegating connection design to ensure that connections behave as flexibly as possible to align with design assumptions. Whether a connection is bolted or welded also has an effect on the stiffness. Welding the outstanding leg of the angle to the beam web is stiffer than the equivalent bolted connection since bolt slip is eliminated (Morris and Packer, 1987). Deeper beams with longer connections tend to behave more rigidly than shallow beams with

shorter connections (Astaneh et al., 1989).

Shear connections have non-zero rotational stiffness, and transmit moment into the support- ing member. There are distinct differences in connection stiffness even within this category, with single and double angles being more flexible than shear tabs. Although moment that is transmitted to the supporting member from eccentric shear loading is mostly immutable, designers have the freedom to select the shear connection, which will determine how much further the point of zero moment shifts away from the support. To that end, designers usually seek to minimize the stiffness of shear connections when their goal is to provide a simple shear connection to minimize the distance between the point of zero moment and the supporting member.

4.2.3 Summary

Shear tabs or angles are commonly welded to embeds to provide shear connections to support steel framing. The behaviour of beam-to-beam or beam-to-column connections has been studied extensively for structural steel framing, and the concept of semi-rigid connections was introduced to describe the spectrum that connections exist on which classifies their rotational stiffness. Shear connections, often classified as simple or pinned supports transmitting only shear to the supporting member, have varying degrees of rotational stiffness and transfer moments to the supporting member in addition to moment coming from the eccentricity of the shear load. The total moment applied to an embed produces tensile forces in the back or top row of anchors. These tensile forces are transmitted to the concrete and interact with the shear forces, resulting in a reduction in shear capacity. Chin (2021) showed that neglecting this effect results in unconservative estimates of capacity even for simple shear connections and a test setup that included some degree of rotational restraint beneficial to the shear capacity of the embed. The interaction of tension and shear forces is usually accounted for using tension shear interaction equations developed for use in situations of concentric shear and tension loading. Whether the existing interaction equations are still appropriate for the stress state generated by shear connections has yet to be determined.

5 Experimental Program

5.1 Introduction

Few recent studies estimated the capacity of anchorages in RC (Park et al., 2017; Sharma et al., 2018). The majority of research used to generate equations shown in Annex D pro- visions is not necessarily representative of embeds, or more generally, anchor groups with multiple rows of anchors. Most research is based on single anchor tests, many of which are loaded in pure shear using uplift restraint that prevented rotation of the loading apparatus and by extension, the anchorage (Sharma et al., 2017b). Some researchers placed teflon sheets between the baseplate and the concrete to minimize friction to isolate anchorage ca- pacity (Grosser, 2012). In reality, embeds often use multiple anchors with the load applied eccentrically through a shear connection. Even tests that applied combined shear and tension loads do not accurately represent loads applied to simple shear connections, which are sub- ject to shear load and moment generated load eccentricity and fixity inherently present due to connection stiffness. Concentrically applied tension loads are distributed evenly amongst all of the studs of an embed, whereas eccentric shear produces tension only in a few of the studs. The interaction of the tension and shear failure modes may not be accurately assessed by the existing method of calculating tension shear interactions.

Full-scale tests were used to (1) study the behaviour of embeds as a whole, rather than just headed anchors or embeds under pure shear, in concrete containing various levels of re- inforcement; and (2) investigate the effects of connection flexibility on the concrete breakout strength of typical embeds. The tested plates were loaded in shear perpendicular to a free edge, with load applied at a fixed eccentricity through a shear tab or double angle connec- tion. These tests build off of work by Chin (2021) who conducted similar tests examining embeds at various edge distances with minimal reinforcement.

5.2 Test Program

Embeds with two different connection details, all placed at a constant edge distance of 150 mm to the centre of the nearest studs (i.e., $c_{a,1}$ = 150 mm), were loaded in shear towards the concrete edge. This edge distance was selected because it is large enough to allow for variation in the reinforcement spacing to have an effect, but not so large that stud shear failure would be the governing failure mode.

Eight tests were completed with varying connection types and reinforcement layouts with the test matrix shown in Table 5.1. Rationale behind the presented parameters is given later in this section. Tests are identified with a two-term description. For the first six tests, the test name establishes whether the embedded plate utilizes a shear tab (ST) or a double angle (DA) connection, as well the reinforcement spacing. For example, DA-175^{P} is a test with a double angle connection, and a reinforcement layout of 10M stirrups at 175 mm on centre with a 15M perimeter bar at top and bottom. For the last two tests, where perimeter reinforcement (PR) is varied, the terms indicate the type of perimeter reinforcement. PR- UR^{P} indicates that there is no perimeter reinforcement, while PR-20M^{B} contains four 20M perimeter bars, with both tests having identical stirrup layouts of 10M bars at 250mm on centre and shear tabs for their shear connectors. ^{P} and ^{B} relate to the conditions of the test program, discussed later.

Table 5.1 – Test matrix

Test Number	1	2	3	4
Test Name	ST-250[P]	DA-250[P]	ST-215[B]	DA-215[B]
Reinforcement	10M @ 250	10M @ 250	10M @ 215	10M @ 215
Layout	2 - 15M Caps	2 - 15M Caps	2 - 15M Caps	2 - 15M Caps
Connection Type	Shear Tab	Double Angle	Shear Tab	Double Angle
Edge Distance, $c_{a1,1}$	150	150	150	150
Embed	4SEP-150	4SEP-150	4SEP-150	4SEP-150

Test Number	5	6	7	8
Test Name	ST-175[P]	DA-175[P]	PR-UR[B]	PR-20M[B]
Reinforcement	10M @ 175	10M @ 175	10M @ 250	10M @ 250
Layout	2 - 15M Caps	2 - 15M Caps	No Caps	4 - 20M Caps
Connection Type	Shear Tab	Double Angle	Shear Tab	Shear Tab
Edge Distance, $c_{a1,1}$	150	150	150	150
Embed	4SEP-150	4SEP-150	4SEP-150	4SEP-150

Notes:

[P] *denotes test completed with pinned loading configuration*

[B] *denotes test completed with bolted loading configuration*

Two concrete blocks were cast with dimensions of 1750 × 1750 × 400mm, with four embeds cast in each block at the centre of each edge. Block dimensions were selected so that supports would not interact with the expected concrete breakout cone based on the size of the plates and the distance from the edge of the block to the furthest anchors ($c_{a1,n}$). Block depth was selected to represent widths found in typical RC beams. Longitudinal reinforcement, in this work defined as being placed in the direction of the applied shear load, is analogous to stirrups if each edge is assumed to be the bottom of an RC beam, consisted of 10M bars with spacings of 175 mm, 215 mm, and 250 mm on centre. Transverse edge reinforcement, defined as being perpendicular to the direction of the applied shear load, was kept constant at two 15M bars when the stirrup spacing was varied (six tests) though there were two tests where the stirrups were kept at a constant spacing of 250mm on centre and the edge reinforcement was either four 20M bars or unreinforced entirely. Drawings of the test specimens are shown in Figure 5.1, indicating plate placement and reinforcement layout.

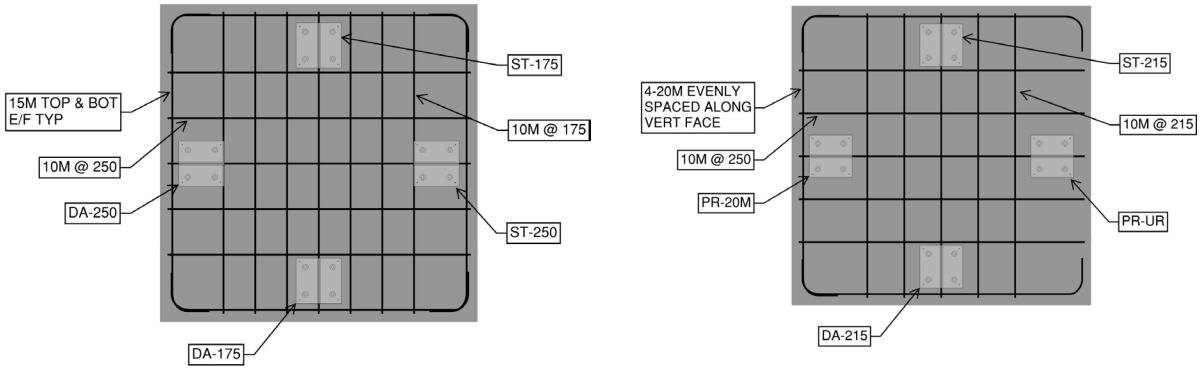

Figure 5.1 – Plan drawing of block used for (a) ST-175^{P}, DA-175^{P}, ST-250^{P}, DA-250^{P}, and (b) ST-215^{B}, DA-215^{B}, PR-20M^{B}, PR-UR^{B}

.

5.2.1 Embedded Plate Design

Aside from the shear connection, the baseplate size and thickness, and the stud size, length, and layout, are consistent with the Four Stud Embedded Plate (4SEP) proposed by Chin (2021), and identified accordingly. 4SEP includes four headed studs with a shank diameter of 16 mm and an effective embedment length of 150 mm. The anchors are welded to a 250 mm × 250 mm × 16 mm anchor plate. Chin (2021) provided load tables based on Annex D of CSA A23.3:19 that can be referenced to ensure that, at minimum, the standardized embeds exceed the requirements of Annex D.

Two connection details were considered. The first, a double angle connection, consists of two L102×76×7.9 mm angles with the short leg welded to the anchor plate along their toe. Load was applied through three 22 mm diameter ASTM A325 bolts at an eccentricity of 65 mm from the face of the baseplate. This eccentricity was selected to be consistent with typical gauge lengths for angle connections of this type. Drawings of this plate are shown in Figure 5.2a.

The second connection detail is a 16 mm thick shear tab with three 22 mm diameter ASTM A235 bolts at an eccentricity of 65 mm from the face of the baseplate. This is analogous to the shear tab used in the tests conducted by Chin (2021), with the exception being that the bolt line was moved from 75 mm to 65 mm to be consistent with the double angle connection.

The shear tab was welded to the anchor plate with a continuous 10 mm fillet weld on both sides, while the angles were welded continuously along their toe with a 6 mm weld. The shear tab was the same depth as the anchor plate (250 mm), while the angles were only 230 mm long, leaving space for weld returns. This is a necessary feature for the angles, since it is expected that there will be plastic hinging near the weld and returns help to preclude weld tearout. Drawings of this plate are shown in Figure 5.2b.

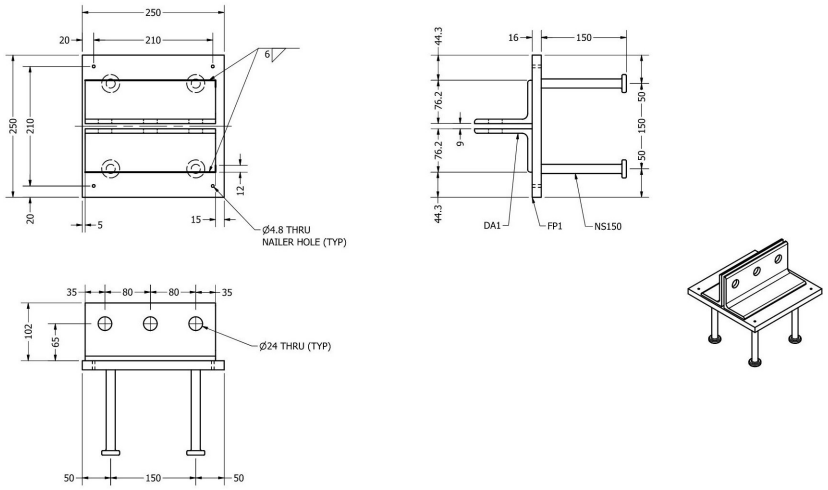

(a)

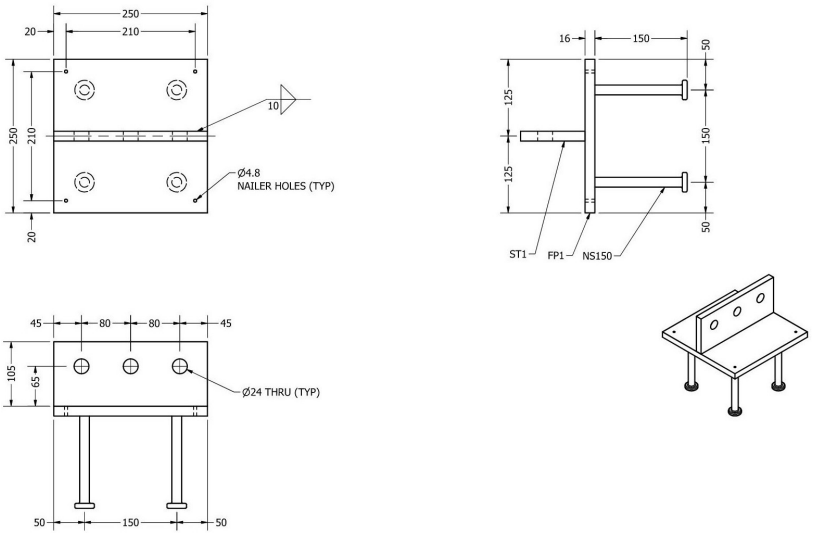

(b)

Figure 5.2 – Shop drawings for embedded plates with (a) double angles and (b) shear tabs. ST1, DA1, FP1, and NS150 are item marks for fabrication purposes.

5.2.2 Reinforcement Details

Stirrup spacings were selected to represent a range of spacings found in RC beams. 250 mm, while a relatively small amount of reinforcement, was chosen as a baseline to match experi- ments by Chin (2021). Chin (2021) tested four-stud and six-stud embeds in RC at various front stud edge distances (75 mm, 125 mm, 150 mm, 250 mm) with 10M stirrups at 250 mm on centre. Chin (2021) concluded that even with minimal reinforcement embeds distribute load to all studs, rather than relying only on the most critical studs, typically those in the row furthest from the edge. In all eight of their tests, Chin (2021) found that peak load exceeded the capacity of the critical studs, despite multiple tests having a stud-spacing-to- edge-distance ratio, $s/c_{a1,1}$, of greater than or equal to 0.6, which ACI 318-19 suggests is the maximum value where all studs can contribute to shear capacity. When this ratio is greater than 1.0 it is increasingly likely that a breakout cone will form from the front studs and they will no longer be able to carry any meaningful load.

A difference in the proposed test program from Chin (2021) is that they placed stirrups on either side of the plate, whereas in the current program the first stirrup was located between studs. For the parameters chosen, the latter configuration is expected to have in- creased resistance. The stirrup between the anchors has the largest anchorage length with the breakout body, and the next nearest stirrups are almost always within $0.5c_{a1,n}$ of the nearest anchor, so they are expected to develop their full yield strength as well. Stirrups outside of the anchors have a development length within the breakout body proportional to the distance from the embed and the angle of the breakout cone, assumed to be 35°. In all cases it is assumed that stirrups are adequately anchored outside of the breakout body in the concrete block. This is a reasonable assumption for closed stirrups in general.

The smallest stirrup spacing of 175 mm was selected as a lower limit since plate capac- ity for stirrups spaced this tightly was expected to coincide with the shear strength of four headed studs. Therefore, it is possible that failure would shift from concrete breakout to steel shear in the most heavily reinforced tests. The largest spacing of 250 mm was selected to be consistent with Chin (2021) so some of the test results could be directly compared.

5.2.3 Perimeter Reinforcement

The last two tests focused on the effect the edge reinforcement has on embed behaviour. PR-20M^{B} included four 20M bars along the vertical face and was intended to provide a level of reinforcement representative of what might be found in the tension face of an RC beam. CSA A23.3:19 permits a 20% increase in concrete breakout strength if at least one 15M bar is provided as edge reinforcement, but it is possible that increasing this reinforcement may have a beneficial effect which would be worth including if it is common to have much more than a 15M bar, as is the case with most RC beams. Previous research suggests that the contribution of perimeter reinforcement is unreliable and unpredictable as it depends on catenary action between perpendicular reinforcing bars (Sharma et al., 2017a; Chin, 2021).

5.3 Fabrication Process

Two concrete blocks were cast in separate forms. Each form had a footprint of 2400 × 2400 mm to accommodate diagonal braces that supported form walls, but also as a matter of convenience since plywood comes in ~2400 mm lengths. Braces were set at 400 mm spacing along each wall and corners were secured with steel strapping. Screws were used where fas- teners were required so that the larger intact pieces of material would be salvageable, and where possible fasteners were driven from outside of the formwork so that forms could be easily dismantled once the concrete had cured.

Next, reinforcement cages with 400R rebar were assembled using wire ties at every joint. Longitudinal reinforcement consisted of closed 10M stirrups, while perimeter bars varied in size and quantity depending on the test, and always had the appropriate hook length on both ends to ensure adequate anchorage per A23.3:19. 10M lifting hooks were included to allow the specimen to be lifted via crane. Once constructed, the cages were set in place with 32 mm reinforcement chairs.

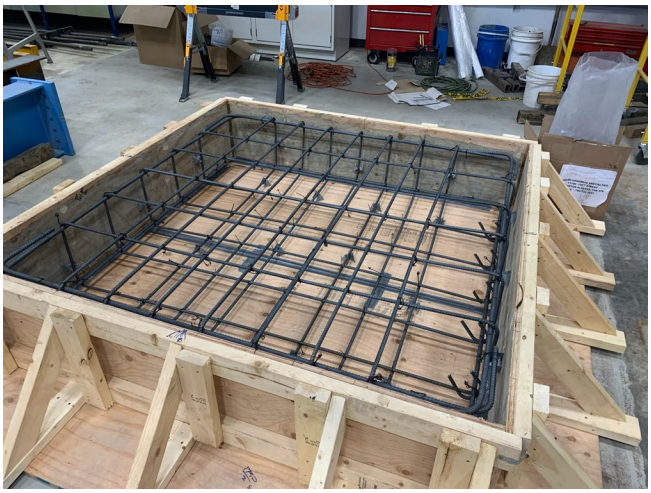

Figure 5.3 – Reinforcement cage prior to embed placement and concrete pour (lifting hooks not shown).

The embeds were screwed to 38 × 89 mm ("2×4") wood pieces using nailer holes on the baseplate. The 2×4's were supported by the form walls on either end which ensured that the embeds were flush with the top of concrete. Consolidators were used to ensure that there were no voids left in the concrete, specifically around studs and underneath the baseplate. Cylinders were poured for compressive tests, and beams were poured for Modulus of Rupture (MOR) tests. Finally, the surface was left watered for 7 days, until the forms were stripped, and concrete was allowed to cure for at least 28 days prior to testing.

5.4 Materials

Three 100 mm × 200 mm concrete cylinders and three 150 mm × 150 mm × 450 mm MOR beams were tested 35 days following the pour. Compressive strength was determined per ASTM C39 (ASTM, 2018a), while the rupture strength was determined according to ASTM C78 (ASTM, 2018b). The elastic modulus was calculated using the stress and strain at 40% of the peak compressive stress per ASTM C469 (ASTM, 2014). These results are shown in Table 5.2. The concrete slump was ~100 mm and the maximum nominal aggregate size was 20 mm. The experimental program was conducted approximately 90 days after concrete was poured.

Table 5.2 – Concrete cylinder and MOR 35 day strengths

Cylinder	Compressive Strength, f_c^t (MPa)	Rupture Strength, f_r (MPa)	Elastic Modulus, E_c (MPa)
1	37.4	4.21	26.4
2	40.6	4.83	26.7
3	43.8	4.08	25.4
Mean	40.6	4.37	26.2
Std. Dev.	3.20	0.40	0.67
CoV	7.9%	9.2%	2.6%

Three samples were taken from each of the three different reinforcement sizes and tested in uniaxial tension, in general conformance with ASTM A370 (ASTM, 2021). Results are shown in Table 5.3.

Table 5.3 – Reinforcement properties

Reinforcement Size	Yield Strength, f_y (MPa)	Ultimate Strength, f_u (MPa)	Elastic Modulus, E (GPa)
10M	468 ± 5.1	681 ± 1.2	204 ± 4.6
15M	462 ± 2.3	690 ± 1.2	204 ± 4.6
20M	410 ± 4.6	597 ± 5.6	198 ± 4.0

± indicates standard deviation

Finally, three Nelson studs were machined into dogbone specimens and tested in general con- formance with ASTM A370 (ASTM, 2021) to determine their yield and ultimate strengths. Results are shown in Table 5.4 and stress strain curves are shown in Appendix C.

Table 5.4 – Nelson stud properties

Stud Number	Yield Strength, f_y (MPa)	Ultimate Strength, f_u (MPa)
1	415	503
2	421	510
3	421	505
Mean	419	506
Std. Dev.	3.78	3.26
CoV	0.8%	0.5%

5.5 Test Setup and Instrumentation

The embeds were loaded in shear towards an edge using a hydraulic jack anchored to a strong wall (Figure 5.4a). The actuator was bolted to a 38 mm thick plate that was bolted to the strong wall at the level of the shear connection (Figure 5.4b). Vertically slotted holes were included in the plate to give flexibility in the final elevation of the actuator. The jack was connected to the plate through two 25 mm thick pieces of flat bar. The concrete block was supported by a few pieces of wide-flange beams and HSS. The two supports bore on a transfer beam that spanned between two columns bolted to the strong floor. The clear span between the supports on the block was approximately 1400 mm, which left room for the predicted breakout cone width of 1050 mm. A tie down strap at the opposite end of the block was secured to the strong floor to prevent block uplift.

(a) **(b)**

Figure 5.4 – (a) Test setup prior to instrumentation installation and (b) pin connection between the jack and the strong wall

The instrumentation is shown in Figures 5.5 and 5.6. Two cable transducers were connected to the back corners of the baseplate using fishing line to measure its displacement in the direction of the applied load. Two clinometers were used to measure rotations: one placed on the baseplate, and the other on top of the wide-flange section that applied load to the embed (Section 5.6). LVDTs were placed on each side of the block to capture movement as the specimen was pulled into bearing by the loading arm. Finally, a Canon Rebel T6i

DSLR was placed above the specimen capturing 4000 × 6000 pixel photos for Digital Image Correlation (DIC) using VIC 2D (Correlated Solutions, 2009) of the surface of the block. All sensors collected data at 2 Hz, while the DIC camera captured photos at 0.33 Hz.

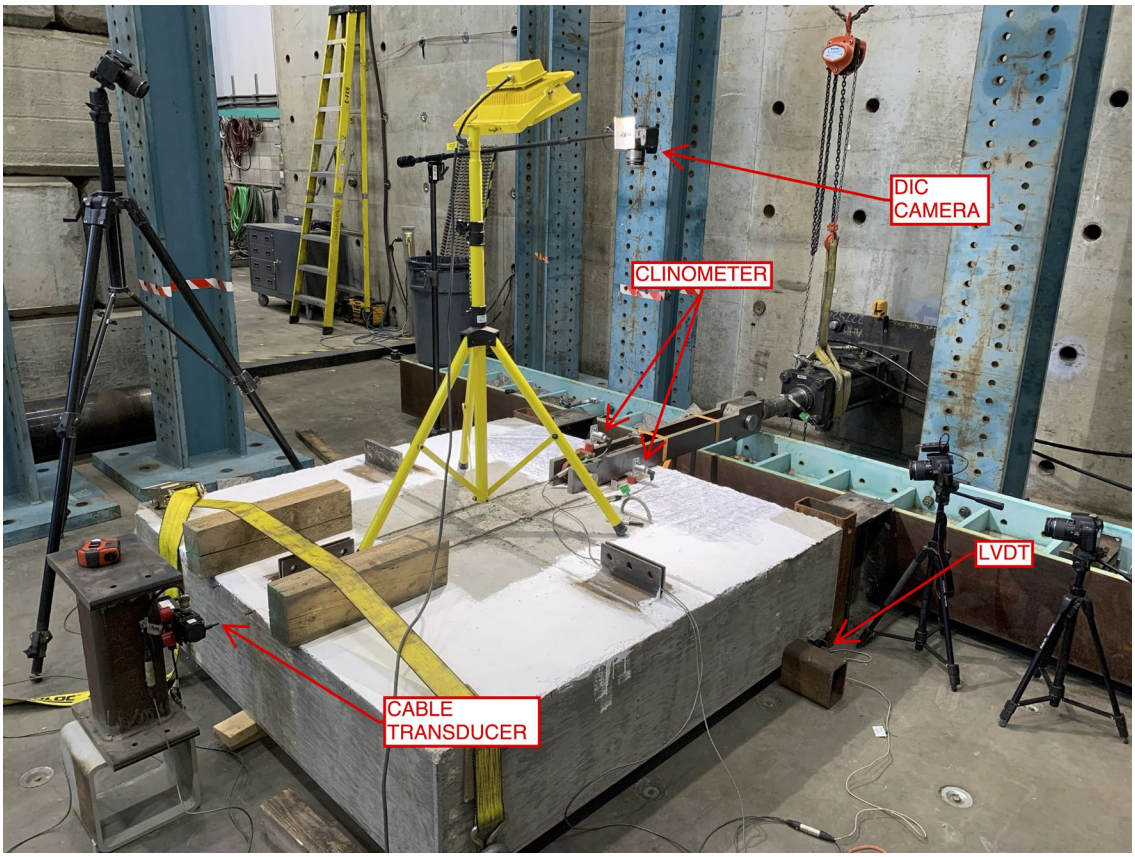

Figure 5.5 – Test instrumentation

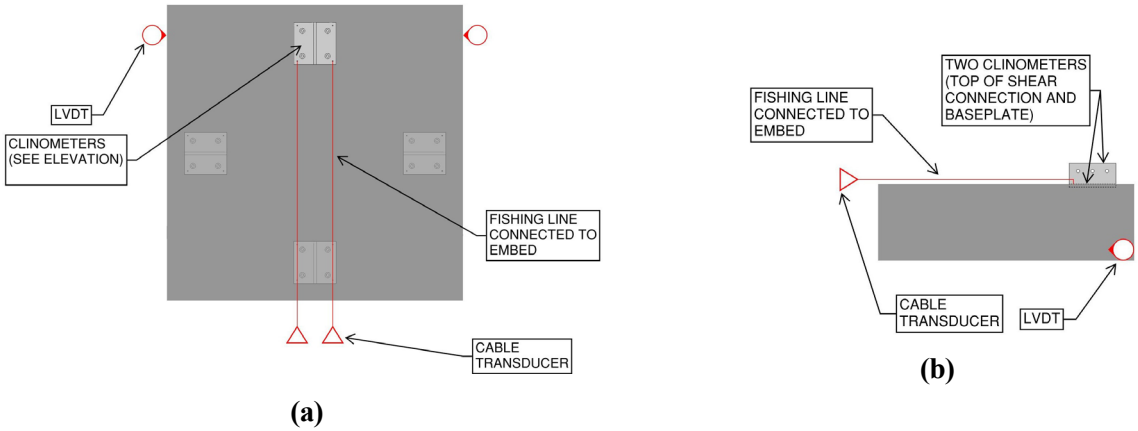

Figure 5.6 – Schematic of instrumentation used in the test program. (a) Plan view and (b) section view

Prior to testing to failure, a pre-load of ~30 kN was applied to pull the block tight to the supports. This load was large enough to move the block against the reaction beams but was well below the load at which any damage (e.g., cracking) occurred for all tests. After setting the block, the connection was unloaded then tested to failure.

The definition of failure depended on the test. For tests that failed by concrete breakout, load was applied until the load dropped below 50% of peak, or when displacement exceeded 25 mm, which was well past the peak load for all tests. For tests that failed by weld rupture (DA-175^{P} and DA-250^{P}), the specimen was unloaded immediately after the drop in load associated with rupture. The load rate was controlled manually during tests and averaged
0.7 kN/s from 30% of peak load up to the peak load. After peak load, loading continued at an average rate of 2.8 mm/min.

5.6 Loading Arm

A major focus of this test program was the method of load application. How load is applied to the embed and what restraints are imposed by the loading arm have an impact on connec- tion behaviour. Many test programs consider pure shear or tension loads but a typical shear connection, where there is a load rotation relationship that needs to be considered is not so straightforward (as discussed in Section 4.2). This behaviour cannot be properly assessed when uplift restraint is provided.

Sharma et al. (2017a) conducted tests where vertical restraint was provided to the con- nection opposite the loading arm (Figure 5.7a). This enabled them to determine the shear capacity increase gained from increased reinforcement around the anchorage. Sharma et al. (2017a) specifically mentioned that the behaviour of embeds under shear load without uplift restraint requires further investigation. They theorized that without uplift restraint failure may be a combination of shear and tension breakout, and that this prying effect would likely reduce the shear capacity of the anchorage (breakout pattern shown in Figure 5.7b).

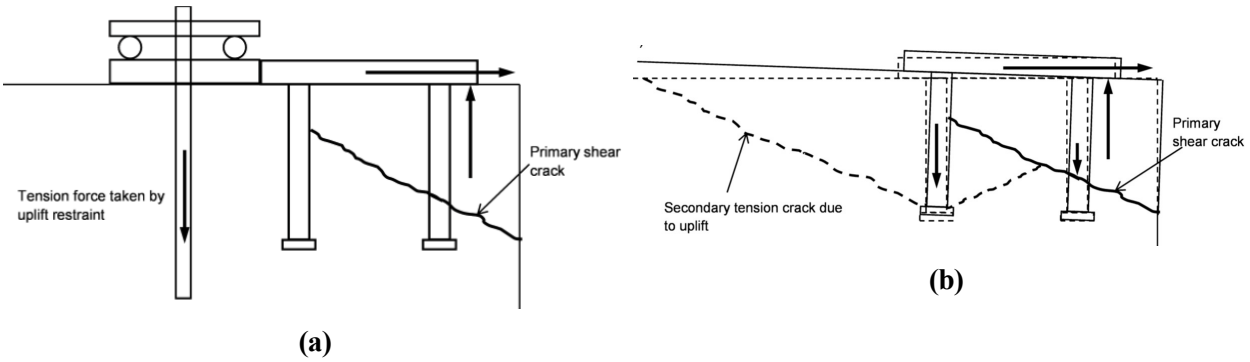

Figure 5.7 – Embedded plate loaded (a) with uplift restraint and (b) without uplift restraint (Sharma et al., 2017b)

The extent to which tension breakout reduces shear capacity is often estimated using the tension shear interaction equations from CSA A23.3:19 and is discussed in Section 4.2.1. However, this equation is intended for combined shear and tension loads, which usually results in tension being equally distributed to each stud. Under an eccentric shear load, the tension is applied to studs furthest from the edge (in the simplest case of two rows of anchors), and the compressive force underneath the front of the plate provides a beneficial effect by preventing tension breakout cones from fully developing. This is analogous to baseplates subjected to bending moments. EN1992-4 includes a factor, Ψ_M , that modifies the tension breakout strength of baseplates to account for this effect (Equation (4.20)). Chin (2021) noted that when loading arms are bolted to the shear connection, moments are generated in the loading arm, restraining some rotation of the embed. In addition to bolting the loading arms to the shear tab, Chin (2021) placed a pedestal underneath the jack that prevented the jack from rotating about its rear pin support (Figure 5.8b). These constraints provide complete uplift restraint in theory; in reality, play in bolt holes and flexural deformation of

the loading arm allowed for notable embed rotation. Other test programs, such as that of Sharma et al. (2017a), eliminated the shear connection by tapping holes in the baseplate and bolting the loading arm directly to the baseplate, which effectively eliminated the eccentricity of the applied load. In addition to this, uplift restraint was provided behind the embed, shown schematically in Figure 5.8c, which resulted in complete rotational restraint.

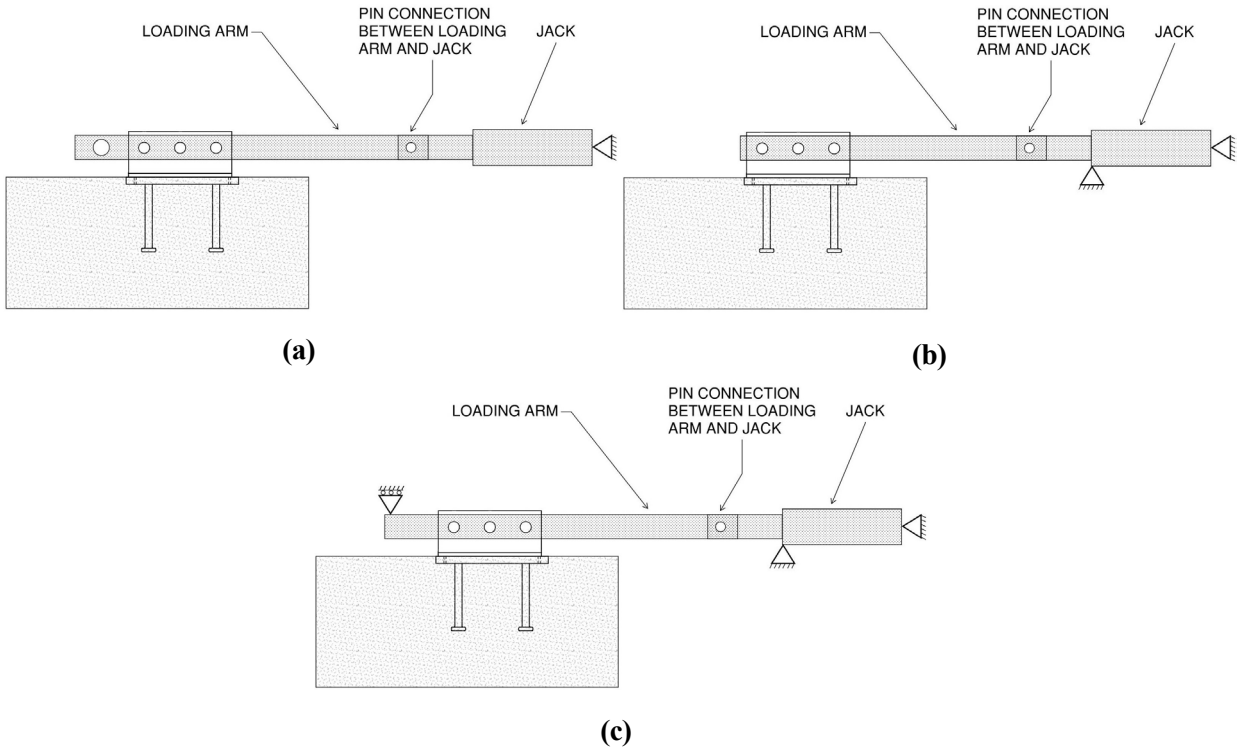

Figure 5.8 – Depictions of researcher's test setups indicating the degree of uplift restraint used. Restraint used in (a) the current test program, (b) by Chin (2021), and (c) by Sharma et al. (2018). Note that for (c) the shear load was not applied through a shear tab but is shown similar to (a) and (b) for consistency.

If a similar method of load application were used in this test program it would limit the two types of shear connections from behaving differently. To address this, a W310×67 was bolted to the shear connection with three 22 mm diameter ASTM A325 bolts and the loading arm applied the load to the wide flange stub through a clevis plate. Since the thickness of the jack's clevis was 76 mm, the flanges of the W310×67 were trimmed down to 76 mm so that a 76 mm shear pin could be used to connect the loading arms to the jack, and a 51 mm pin could be used to connect the loading arms to the embedded plate assembly. (Figure 5.9).

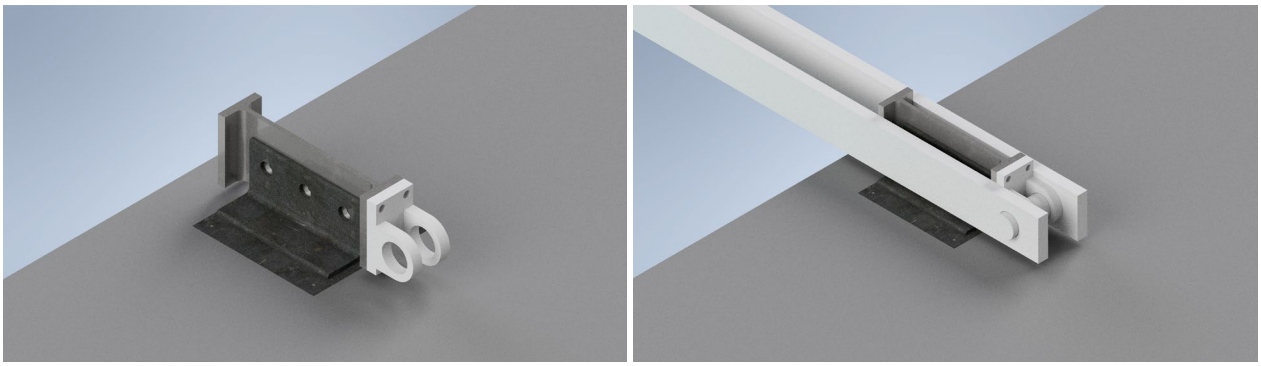

(a) **(b)**

Figure 5.9 – Rendered image of embedded plate with (a) wide-flange stub and clevis plate attached, and (b) with loading arms attached.

The intent of this connection was to decouple rotation of the embed from the loading arm, which would allow the more flexible angles to flex away from the baseplate while the shear tab would remain effectively rigid.

The first four tests (ST-250^{P}, DA-250^{P}, ST-175^{P}, DA-175^{P}) were completed using this pinned connection detail. However, for the last four tests (ST-215^{B}, DA-215^{B}, PR-20M^{B}, PR-UR^{B}) the connection was modified to eliminate the pin at the embedded plate, and the loading arms were bolted directly to the shear tab or double angles with spacers to fill the gaps between the embed's shear tab/angles and the loading arms (Figure 5.10). This decision was made due to undesirable behaviour in the first four tests, discussed in Chapter 6. This bolted connection at the embed is analogous to that from Chin (2021). However, there was no pedestal placed under the front of the jack, so the jack was still able to rotate freely.

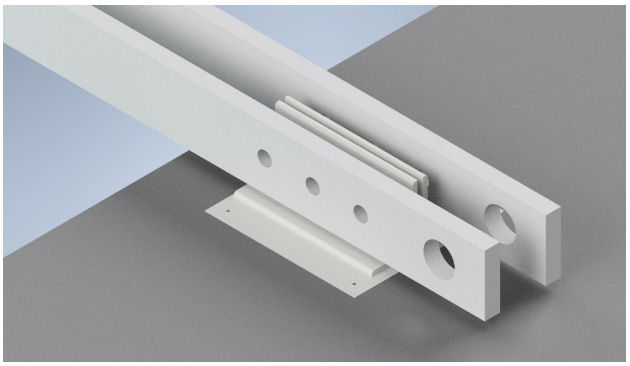

Figure 5.10 – Rendered image of an embed with loading arms modified to include three bolts to connect loading arms directly to the angle legs or shear tab

6 Results and Discussion

Table 6.1 summarizes the results for all eight tests, and the load displacement curves are shown in Figures 6.1a and 6.1b. The reported net plate displacement was calculated by av- eraging the LVDT readings that recorded the displacement of the specimen and subtracting that from the average value of the two cable transducers that were measuring the displace- ment of the embed. The difference between transducer readings was typically less than 6% of the larger of the two values until beyond peak load. In all tests the specimen was pulled into bearing against the supports with a preload of 10-20% of the expected maximum load prior to the test to minimize sliding of the block following processes used by Chin (2021). ST-250^{P} was stopped earlier than other tests due to excessive cracking that unexpectedly extended into areas that conflicted with the breakout cones of other tests in the same block (see Figure 6.1a). Inspection of the block following this test suggested that these cracks were superficial at the points where they crossed into the breakout cones of subsequent tests, and therefore it is believed that they did not affect the capacities of the adjacent embeds. The load displacement curves of ST-175^{P} and PR-20M^{B} are shown up to the point that the load decreased to approximately half of the peak load. The load displacement curves for ST-215^{B}, DA-215^{B}, and PR-UR^{B} are truncated at 20 mm of net plate displacement, which was well beyond the peak load, and there were no notable changes in behaviour past this point. Figure 6.1b includes the curves for DA-175^{P} and DA-250^{P}, tests that failed suddenly due to weld rupture (Figure 6.7c) and these tests were stopped and unloaded immediately following this failure. The distinction between tests completed with the pinned and bolted loading configurations is indicated by a ^{P} and ^{B}, discussed later.

Table 6.1 – Test results

Test Name	Peak Load (kN)	Net Displacement at Peak (mm)	Baseplate Rotation at Peak (rad)	Connection Rotation at Peak (rad)	Failure Mode
ST-250^{P}	277.2	6.71	0.013	0.017	C
DA-250^{P}	231.3	4.48	0.006	0.053	W
ST-215^{B}	278.0	4.40	0.011	0.013	C
DA-215^{B}	276.2	4.72	0.009	0.024	C
ST-175^{P}	286.8	7.01	0.022	0.022	C
DA-175^{P}	229.9	2.49	0.007	0.038	W
PR-20M^{B}	276.1	6.18	0.010	0.019	C
PR-UR^{B}	254.1	2.69	0.003	0.008	C

Notes: Failure mode 'C' refers to concrete breakout, while 'W' refers to a weld failure

^{P} denotes that test was completed with pinned loading configuration

^{B} denotes that test was completed with bolted loading configuration

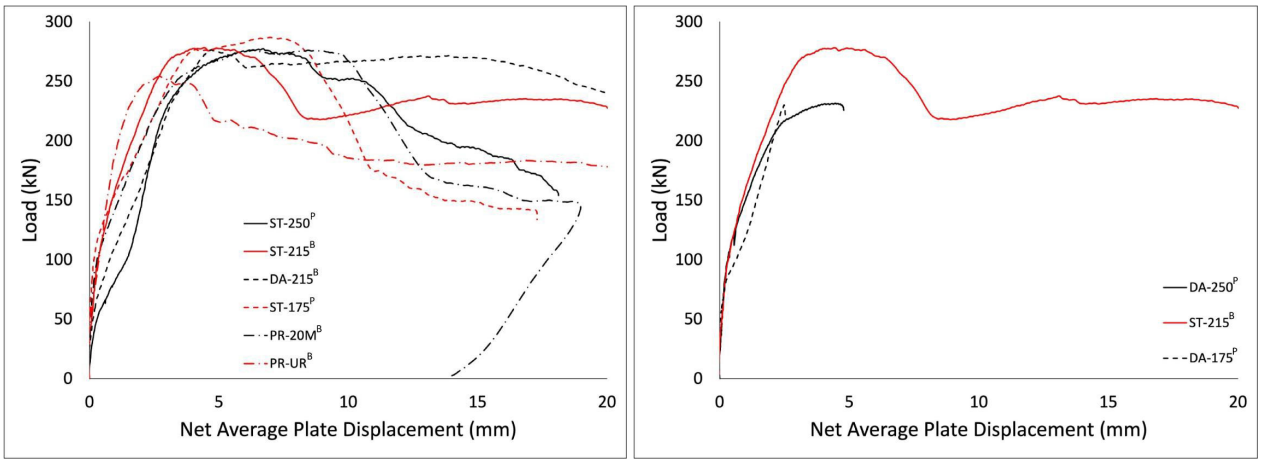

(a) **(b)**

Figure 6.1 – Load versus net plate displacement curves calculated from LVDT and transducer data for (a) the six tests that failed by concrete breakout and (b) the two tests that failed by weld rupture, plus ST-215^{B} for reference.

The load displacement curves for all eight tests show a stiff, mostly linear progression up to 100-150 kN, at which point there is a change in stiffness, and the curve continues linearly, although with a slight reduction in stiffness, up to the peak load.

Although there is some variability in the stiffness between 50 kN and 150 kN, this is not attributed to parameters examined in this program. The facility the blocks were fabricated

at was not same facility as where they were tested, and the floor at the fabrication facility had a slight slope. Although formwork walls were plumbed during construction, the verti- cal faces were out of plumb when the block was placed on a level surface. For some tests the bottom of the block beared against the supports but there was a gap between the sup- ports and the block at the top of the front face (closing of this gap shown in Figures 6.2a and 6.2b). Since uplift restraint at the back of the block was not fully rigid, the block could rotate about the bottom of the front face until the top of the front face came into contact with the supports. Although LVDTs were connected to the block to account for translation, these LVDTs were located at the bottom of the block and did not measure rotation-induced displacement at the top of the block. The test most affected by this was ST-250^{P}. ST-250^{P} exhibited what appears to be a loss in stiffness greater than any other test at around 50 kN, and then stiffness increases again around 100 kN. Comparing the time-lapse video of this test the load-displacement curve, it is clear that the block rotated, and this rotation occurred mainly between 50 kN and 100 kN, and confirmed by the baseplate rotation measurements (Figure 6.12a), that show ST-250^{P}'s baseplate rotating more than any other test from 50 kN to 100 kN. Beyond this point, the test carried on to the peak load with a stiffness con- sistent with the other tests. Note that this effect was not present in all tests depending on the presence of a gap at the top of the bearing surface. The DIC imagery, which captured displacements of the top surface of the block, was able to address this affect.

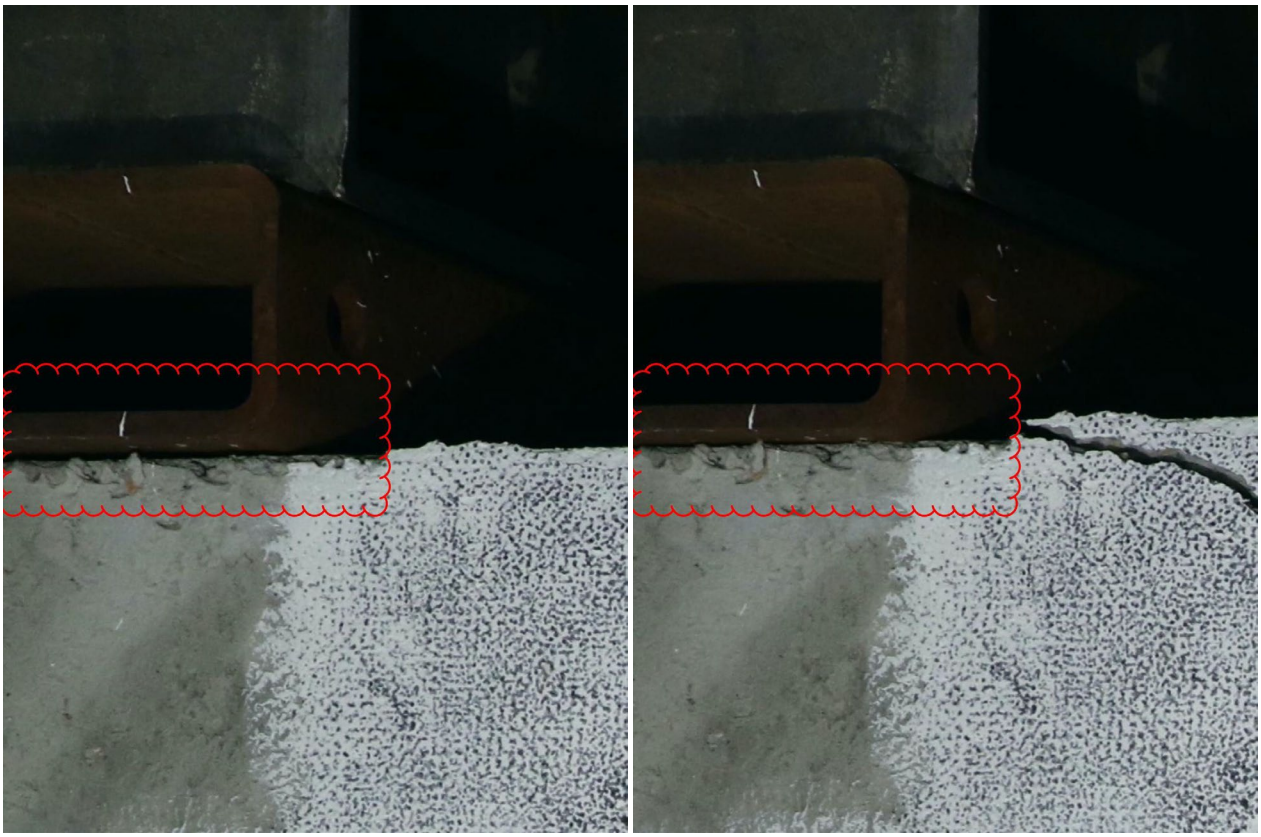

(a) **(b)**

Figure 6.2 – (a) Gap between top of concrete block and bearing support at beginning of test, and (b) at peak load when the gap was closed.

Another factor that impacts stiffness of some tests is how the failure surfaces of previous tests may interfere with the bearing at supports. Although expected shear cracks were contained to the predicted region of $\sim 1.5c_{a1,n}$ on either side of the embed, cracking from behind the embed propagated beyond this region towards supports on either side of the block. When subsequent tests were conducted, there was deformation in regions near the supports that may have contributed to increased displacements. Once again, because the displacement only took place near the upper surface of the block, it could not be captured by the LVDTs at the base of the block. To that end, variation in the stiffness leading up to peak load was not necessarily indicative of actual differences in embed stiffness. This conclusion is consistent with observations from other embed test programs (Sharma et al., 2017a; Chin, 2021) where initial stiffness remained essentially the same regardless of the amount of reinforcement present.

To address these issues encountered with LVDT and cable transducer displacements, a second method of determining net embed displacement was used. Digital Image Correlation (DIC) software is capable of analyzing a series of pictures and tracking displacements of different points within an Area of Interest (AoI) as tests progress. DIC can be used for tests on RC to calculate displacements, rotations, and strains (Gehri et al., 2020). Using the DIC software VIC 2D (Correlated Solutions, 2009), two points on the block directly in front of the embed were used to calculate a new embed displacement, and two more points outside of the failure surface were used to calculate the block displacement Figure 6.3.

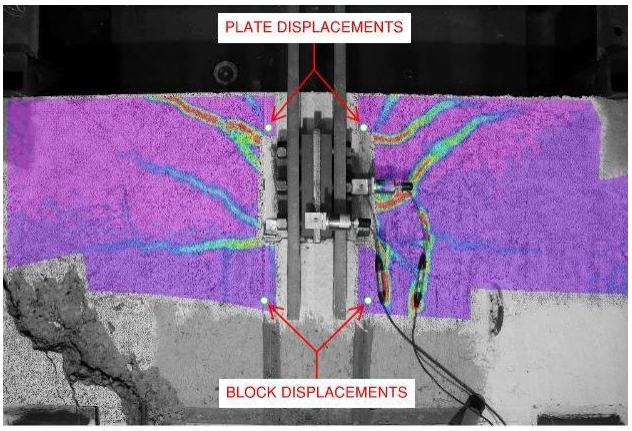

Figure 6.3 – Locations of the points used in VIC 2D to calculate plate and block displacements (principal strains for ST-215 shown).

Since VIC 2D tracks displacements on the block's top surface, it is capable of capturing the additional block displacement not measured by the LVDTs. Since VIC 2D is two-dimensional tracking software that assumes the surface is at a constant distance from the camera, it is unable to account for out-of-plane rotations, though vertical block displacements are likely small enough that this effect is insignificant until after peak load. Note that this method of calculating embed displacement assumes that the concrete directly in front of the embed has a displacement equal to that of the embed. This assumption is reasonable because the baseplate is cast into the concrete rather than sitting on top of it. Since the vertical edge of the baseplate bears directly on concrete, the displacement of the concrete in front of the embed will be almost identical to that of the embed provided that there was no initial gap and that the concrete does not strain significantly. This is reasonable since the majority of load is transferred to concrete through the anchors rather than bearing of the vertical face of the baseplate. Figure 6.4 shows the load displacement curves for ST-250^{P}, and the difference

in behaviour is apparent, particularly from 0-150 kN. The DIC-generated curve does not fall victim to the issues noted with the LVDTs and cable transducers. The DIC curve shows linear stiffness up to cracking, which is consistent with previous experimental programs.

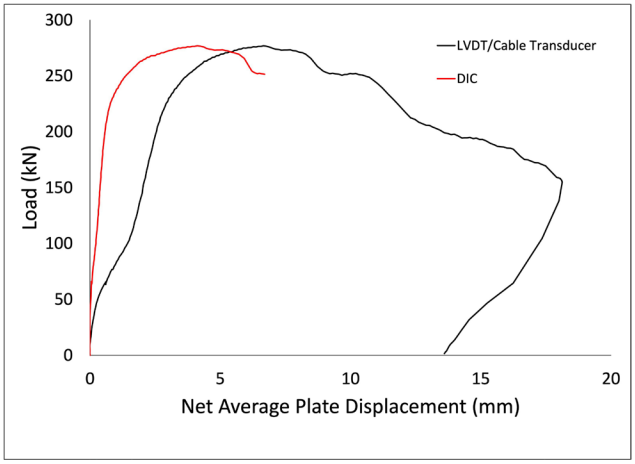

Figure 6.4 – Comparison of the load displacement curves generated from LVDT and cable transducer data, and the DIC data (ST-250^{P} shown).

The load displacement curves generated using VIC 2D are shown in Figure 6.5. These curves are truncated earlier than those shown in Figure 6.1. After the front breakout cone is fully cracked and the plate has displaced 5 to 10 mm, VIC 2D loses the ability to track the points used to calculate plate displacement. Since most of the differences between the two methods occurred in the uncracked range, the post-peak behaviour can still be examined using the LVDT/transducer displacements.

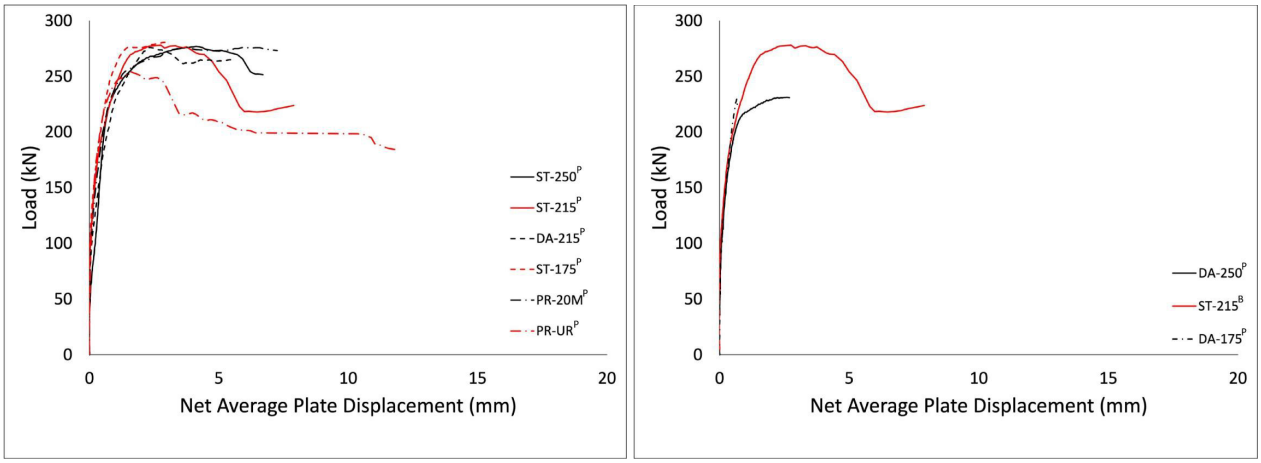

(a) **(b)**

Figure 6.5 – Load versus net plate displacement curves calculated using VIC 2D for (a) the six tests that failed by concrete breakout and (b) the two tests that failed by weld rupture, plus ST-215^{B} for reference. Curves plotted up to the point that DIC was no longer able to track displacements in front of the embed.

The first four tests (ST-250^{P}, DA-250^{P}, ST-175^{P}, and DA-175^{P}) were conducted with the fully pinned connection described in Chapter 5. Although this method of load application has an inherent destabilizing effect, test programs such as Chin (2021) showed such small rotations up to peak load that this was not expected to cause any issues. However, in these tests the pinned connection resulted in cases where the eccentricity of the load alone was enough to cause a combination of shear and tension concrete breakout that can be best described as a pryout effect. This is not the same as the shear pryout failure mode discussed in Sections 2.2.2.2 and 3.1.8. The pryout strength for 150 mm long studs is twice the tension breakout capacity, which far exceeds peak load in these tests. Concrete pryout as a standalone shear failure mode is usually a concern for shorter anchors.

Figure 6.6 – Side view of ST-175^{P} at peak displacement, displaying a combination of tension and shear breakout, or a pryout style failure

The pinned connection had a significant impact on the behaviour of the double angle con- nections in particular. The angles did not have sufficient stiffness to prevent large rotations from occurring and were pried off the baseplate for both DA-250^{P} and DA-175^{P}. Figure 6.7a shows DA-250^{P} at the beginning of the test, and Figure 6.7b shows the last image taken before the welds ruptured. At peak load there is very little shear cracking in the concrete, but a large rotation of the W310x67 stub.

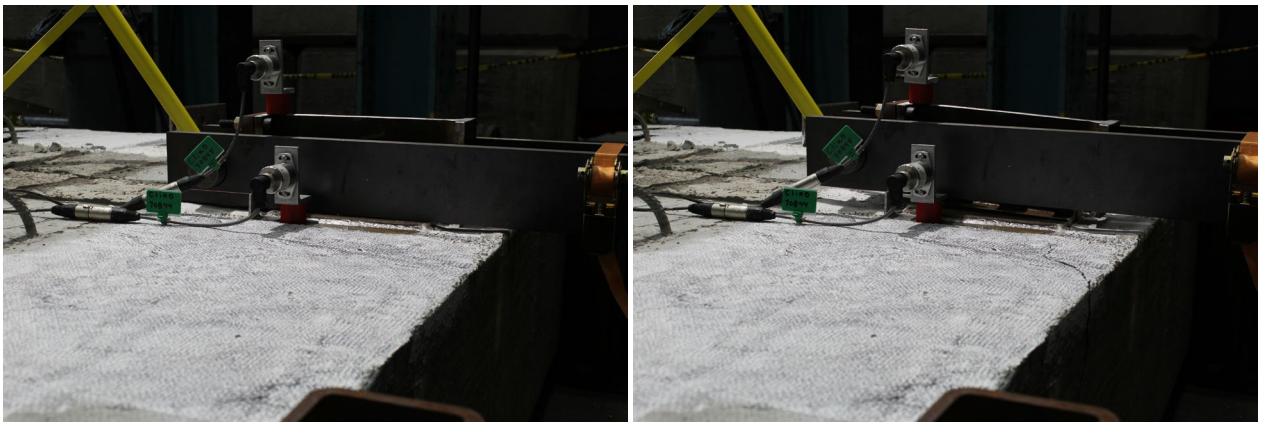

(a) **(b)**

(c)

Figure 6.7 – Side view of DA-250^{P} (a) at the beginning of the test, (b) just before weld rupture, and (c) weld rupture on the angle connection

For the last four tests (ST-215^{B}, DA-215^{B}, PR-20M^{B}, and PR-UR^{B}), the loading scheme was modified by drilling three holes in the loading arms that were used to bolt them directly to the shear tab or double angles (Figure 5.10). The intent of this change was to provide rotational restraint similar to Chin (2021) so the remaining test with a double angle detail (DA-215^{B}) would not also fail by weld rupture. This change was expected to reduce the severity of the pryout effect for all remaining tests. Although it was successful in preventing weld rupture in DA-215^{B}, the remaining tests still exhibited pryout effects similar to the first four tests completed with the pin connection. That this behaviour persisted after the

change in loading arm connection suggests that the destabilizing effect of top-flange loading was not as problematic as initially suspected. This behaviour is instead attributed to the relatively low tension breakout strength of the back row of studs, discussed later. Aside from the final double angle test, DA-215^{B}, failing by concrete breakout, there is no indication that the modified loading configuration provided beneficial effects up to peak load. Beyond peak load, ST-215^{B} and DA-215^{B} showed superior behaviour, maintaining larger loads as displacement increased. This is attributed to the stabilizing effect that this configuration has as rotations increase (Figure 6.8). As the embed rotates the loading arm must also rotate. At large displacements this results in an inclined force on the loading arm coming from the actuator, the vertical component of which has a stabilizing effect as it counteracts embed rotation. The load displacement curves based on DIC displacements show that there was no quantitative effect (i.e., no benefit to peak load) from the change in loading arm.

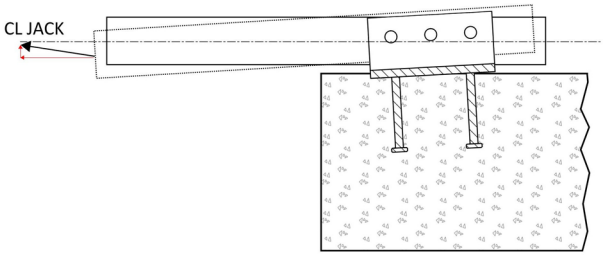

Figure 6.8 – Stabilizing effect of the bolted loading arm connection

6.1 Concrete Breakout Failure

Six of the eight tests failed in concrete breakout (Figure 6.9), with the onset of non-linear behaviour (from concrete cracking and load redistributing to stirrups) occurring above 90% of the peak load. In all eight tests the first crack to propagate from the embed to the concrete edge originated roughly at the first stud row, or 150 mm away from the concrete edge. In some cases, superficial cracks first formed at the front corners of the embed, but as the load increased the primary shear breakout cone formed from the first row of studs.

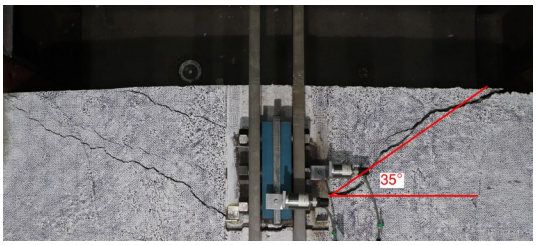

Figure 6.9 – Typical concrete breakout cone for an anchorage loaded in shear towards a free edge (ST-215^{B} shown).

Pictures from the overhead camera, taken in plan view, do not capture the combined tension and shear breakout failure observed in most of the tests. The shear breakout cone is apparent in all pictures, but the tension breakout cone is more visible in Figure 6.10.

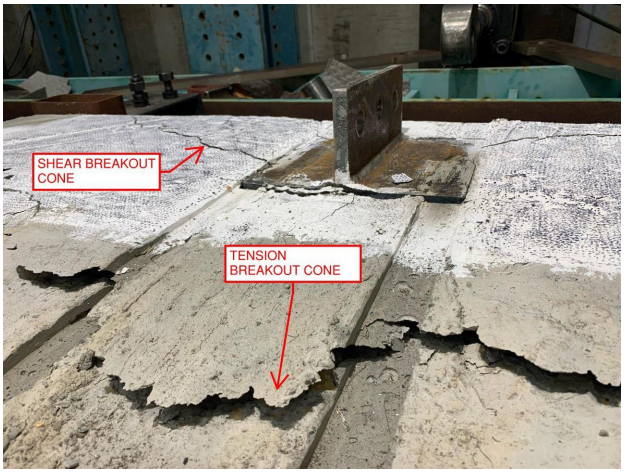

Figure 6.10 – ST-250^{P} breakout cone. Note the shear breakout cone forming from the embed, while the tension breakout cone extends past the back of the embed.

6.2 Considerations for Anchor Group Design

All eight tests greatly exceeded the shear breakout strength calculated using only the front anchor row (54 kN per A23.3:19 with material reduction factors set to 1.0 and 94 kN per the mean CCD expression), despite moment prying effects. The peak load also exceeded the shear strength of two studs (170 kN using the measured ultimate tensile strength and $\alpha = 0.86$) in all tests, indicating load was carried by both rows of anchors. CSA A23.3:19 only permits designers to calculate the steel shear strength based on the back row of studs in all

cases, which differs from ACI 318-19 which permits multiple anchor rows to be considered depending on the ratio $s/c_{a,1}$. Once a failure cone develops at the front row of anchors, only the back row of anchors can be relied upon to resist shear loading. This is a reasonable assumption for unreinforced concrete. However, even in the most lightly reinforced test (PR- UR^B), reinforcement was able to tie the initial shear breakout cone to the secondary shear breakout cone, and distribute load amongst all of the anchors. Since none of the peak loads approached the shear strength of all four studs (340 kN), it is unclear if load was distributed evenly between both stud rows. Figure 6.11 shows one of the back studs from DA-215^B, which exhibited both bending and shear deformations. There was no observed deformation where the weld connects the stud to the baseplate, but shear deformation is large just below that location. This is consistent with research indicating that local increases in strength around welds cause failures to preferentially take place in the weaker, unaffected metal just beyond the weld (Anderson and Meinheit, 2000). Given the extent of the shear deformation, it is advisable to carry on with the conservative assumption that shear load is only resisted by the back anchor row at smaller edge distances (i.e., observing the recommendations from ACI 318-19 discussed in Section 5.2.2) regardless of the reinforcement, since the true distribution of forces amongst studs is too difficult to determine at this time.

Figure 6.11 – Back stud of DA-215^B which yielded due to bending, but also experienced notable shear deformation just below the weld that connected it to the baseplate.

The baseplate and connection load rotation curves are shown in Figures 6.12 and 6.13. These load rotation curves are based on readings from the clinometers, which captured the rotation of the block in addition to the rotation of the baseplate or shear connection. The behaviour of the DA-250^{P} is attributed to the clinometers shifting during the test.

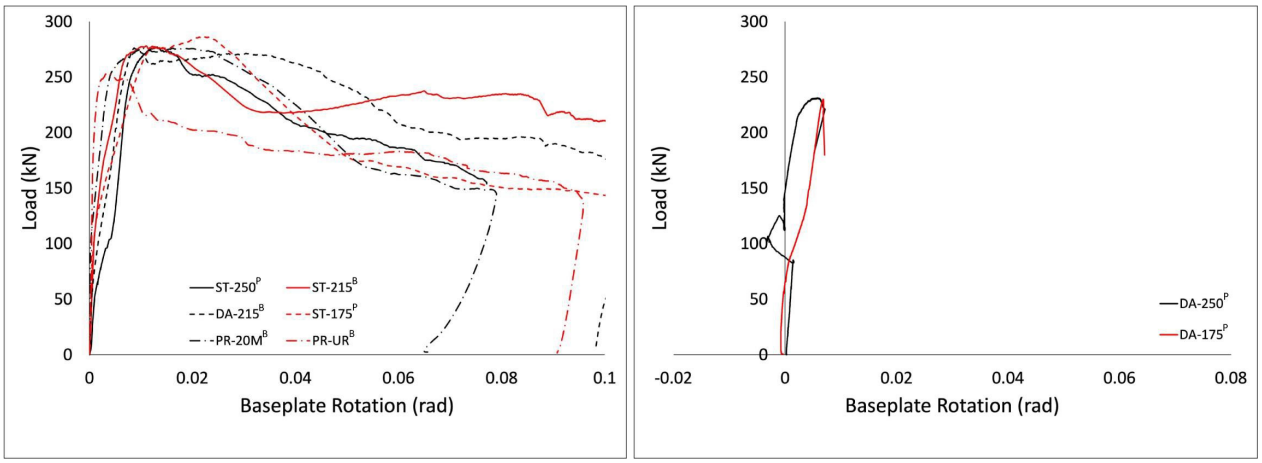

(a) **(b)**

Figure 6.12 – Load versus baseplate rotation curves for (a) the six tests that failed by concrete breakout and (b) the two tests that failed by weld rupture.

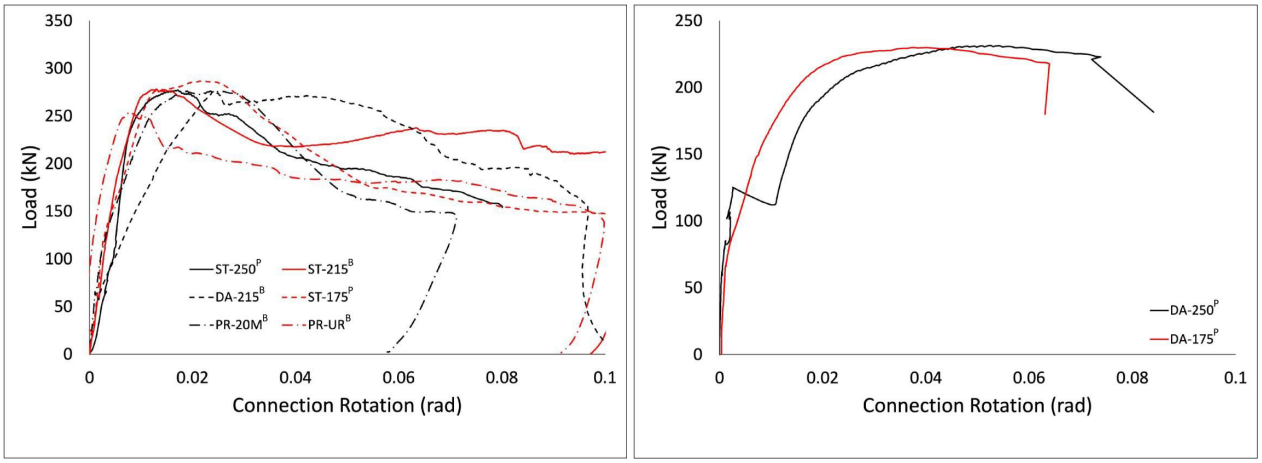

(a) **(b)**

Figure 6.13 – Load versus connection rotation curves for (a) the six tests that failed by concrete breakout and (b) the two tests that failed by weld rupture.

6.3 Effect of Reinforcement on Embedded Plate Capacity

The six tests that failed by concrete breakout had similar peak loads, with an average of 274.7 ± 10.9 kN (± indicates standard deviation). Of the six, only PR-UR^{B}, which was the only test without perimeter reinforcement, had a notably different peak load of 254.1 kN, 21 kN below the average failure load of the tests that failed in concrete breakout.

For the five tests that failed by concrete breakout with perimeter reinforcement, the av- erage peak load was 278.9 ± 4.5 kN. Although a variation of up to 100 kN was expected between the least and most heavily reinforced tests based on preliminary estimates using expressions from Sharma et al. (2018), stirrup spacing had virtually no impact on the peak load. One possible explanation is the transition of the failure mode from shear dominated to tension dominated. Although prying was observed due to the lack of rotational restraint in all tests, the more lightly reinforced tests had more shear cracking while more heavily reinforced tests had more significant prying or tension effects. Figure 6.14 shows ST-250^{P} and ST-175^{P} at their peak displacements (18.1 and 17.3 mm calculated using the LVDT and cable transducer data, respectively). ST-250^{P} displayed more shear deformation as ev- idenced by wider cracks propagating from the embed to the concrete edge, while ST-175^{P} had visibly smaller shear cracks but more rotation. ST-250^{P} had a baseplate rotation at peak load of 0.013 rad while ST-175^{P} was at 0.022 rad, despite ST-250^{P} capturing more additional rotation from the block than any other test (evidenced by the apparent loss in rotational stiffness between 50 and 150 kN). Despite having the highest peak load of all tests, ST-175^{P} had the worst post peak performance, aside from tests that failed by weld rupture, reaching 50% of peak load at a smaller displacement than any other test. Taken with the load rotation curves (Figure 6.12a), this suggests that ST-175^{P} failed primarily in tension breakout and experienced less shear deformation. It is reasonable to conclude that tightly spaced shear reinforcement was successful in resisting shear and the governing failure mode shifted towards tension breakout as a result.

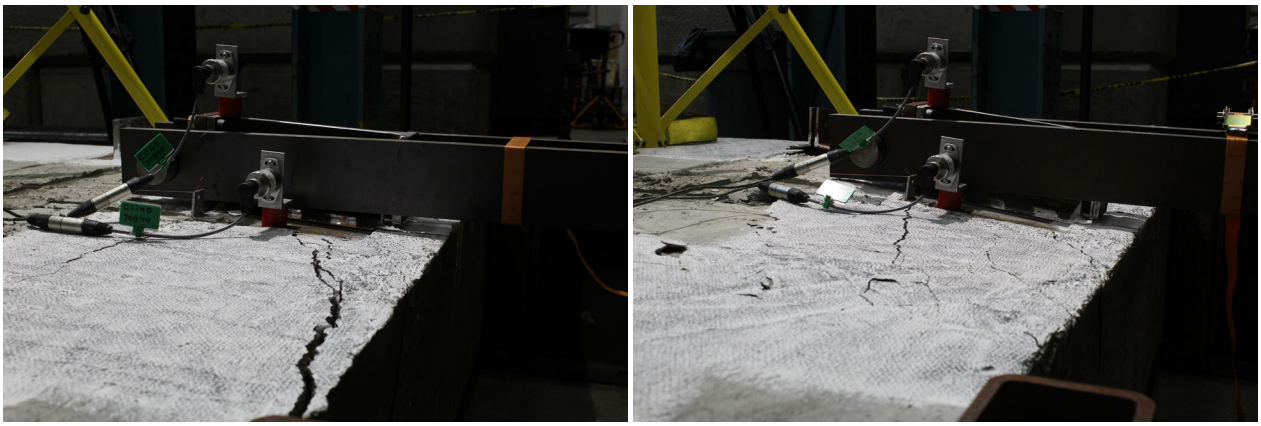

(a) **(b)**

Figure 6.14 – (a) ST-250 and (b) ST-175 at maximum displacement of 18.1 and 17.3 mm calculated using the LVDT and cable transducer data, respectively.

6.4 Effect of Connection Type on Embedded Plate Behaviour

Due to the unexpected weld failures in DA-250^{P} and DA-175^{P}, there is little data to assess the effect of connection detail on plate behaviour. Figure 6.15 compares the load-rotation curves for both the baseplates and connections for ST-215^{B} and DA-215^{B}.

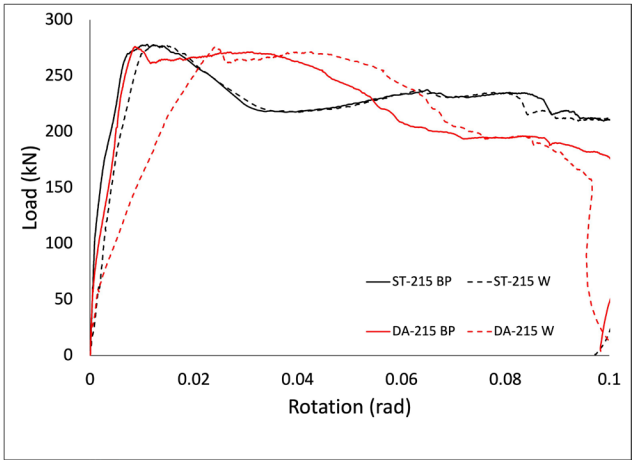

Figure 6.15 – Load-rotation curves for the baseplates (BP) and connections (W) for ST-215^{B} and DA-215^{B}

While baseplate rotations were similar, the tests displayed very different crack patterns, shown in Figure 6.16.

(a) **(b)**

Figure 6.16 – Failure surfaces of (a) ST-215^{B} and (b) DA-215^{B}

ST-215^{B} (Figure 6.16a) exhibited a combination of tension and shear breakout consistent with other tests while DA-215^{B} (Figure 6.16b) had a much less obvious tension breakout surface form. Since the response of DA-215^{B} primarily consisted of shear deformations, the shear reinforcement was better able to contribute to post-peak behaviour, evident in that DA-215^{B} maintained 97% of its peak load up to 15 mm of displacement, while the other five tests ranged from 52% to 85%.

How ST-215^{B} and DA-215^{B} had such different failure surfaces is speculative given the lim- ited amount of tests available. Figure 6.15 shows DA-215^{B} had a connection rotation more than twice that of the baseplate, while ST-215^{B} had near equal connection and baseplate rotations. One explanation is that the rotation needed for the stabilizing effect from the bolted connection (Figure 6.8) to become meaningful is reached earlier for the double angle connection. Interestingly, for both tests load increases following a decrease after peak around a similar connection rotation (0.035 rad) attributed to the stabilizing force allowing stirrups to carry load. If this is what was happening, then DA-215^{B} experienced some amount of uplift restraint much closer to peak load than ST-215^{B}.

6.5 Comparison to CSA A23.3:19

Figure 6.17 compares peak loads from the tests to the provisions from CSA A23.3:19. A23.3:19 provisions are shown for two different cases: the first (Case 1) is how designers

would usually calculate concrete breakout strength. This includes $k_{v,5\%} = 0.58$, the concrete material resistance factor set to 0.65, and $\Psi_{c,V}$ taken as 1.2 for all tests except PR-UR, where it is taken as 1.0. Although concrete was uncracked, which permits $\Psi_{c,V}$ to be taken as 1.4, designers are not usually comfortable making the assumption that concrete remains uncracked. The second case (Case 2) is intended to be a true prediction of embed capac- ity, meaning that the material resistance factor is set to one, $\Psi_{c,V}$ is taken as 1.4 since the concrete is uncracked, and $k_{v,50\%} = 1.0$, to estimate the breakout capacity. Although A23.3 allows designers to use $k_{v,5\%} = 0.66$ for welded headed studs, the author was unable to find supporting evidence for this clause, despite searching through references in the commentary of ACI 318-19. In both cases, the "allowable" shear capacity was calculated through an it- erative process that involves calculating the tension and shear breakout strengths separately and using the tension-shear interaction equation (Equation (3.24)) to estimate the reduction in shear resistance due to combined loading.

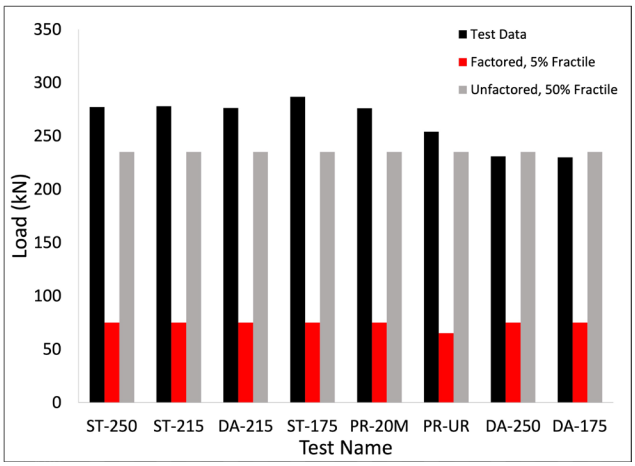

Figure 6.17 – Comparisons of the test results with predictions from CSA A23.3

Clearly Case 1 predictions are extremely conservative with an average test-to-predicted ratio of 3.75, and would be even more so in a limit state design where loads would be factored as well. The average test-to-predicted ratio for Case 2 is 1.17 which is more reasonable but attributed to the fact that reinforcement was not able to be properly engaged due to the transition of failure mode from shear breakout to tension breakout. The test-to-predicted ratios neglect the two tests that failed by weld rupture, since steel strength is not comparable to predicted concrete breakout strength.

6.6 Discussion on Tension Shear Interaction

Earlier discussions posited that the tension-shear interaction equation is unsuitable for use for cases of combined shear and moment. Although moment induces tension forces on some studs, the distribution of forces is not the same as when a tension is applied concentrically to an anchor group, which is what the interaction equation is based on. The tension-shear interaction equation was developed by analyzing a large bank of test data and fitting curves to the data. Many of these tests were conducted on single anchors which are not subject to effects being considered, and since the focus of the tests was not the shear connection but rather the embed itself, those tests did not consider any load-rotation behaviour, rather focusing on pure shear and tension loads.

The development of a more accurate method, or the verification of the efficacy of the current method, is beyond the scope of this project, and to that end the existing interaction equation is used throughout this report to calculate anchorage capacities. The interaction equation is an appropriate approach for the time being because it gives a conservative solution, provided that all sources of tension are considered (eccentric loading, partial fixity, and/or directly applied moments). This is because the beneficial effect of rotational restraint is neglected in the calculation of moment that is applied to the embed, as is the effect of the increased con- finement from the compression zone adjacent to the back stud tension breakout cone. Just how conservative this assumption is varies depending on the amount of rotational restraint as well as the distance between the back studs and the centroid of the compressive reaction. Since the test program did not provide any meaningful rotational restraint, the results are well suited for comparison against predictions using the tension-shear interaction equation, discussed later. A similar implementation of the tension-shear interaction may be less accu- rate for experimental programs that provided uplift restraint (Chin, 2021) because a portion of the moment that is assumed to act on the embed is being resisted elsewhere in the system.

For the standardized Four Stud Embedded Plate (4SEP) with a bolt line 65 mm above the top of the baseplate, Figure 6.18 shows the variation of the available shear strength plotted against the calculated shear resistance.

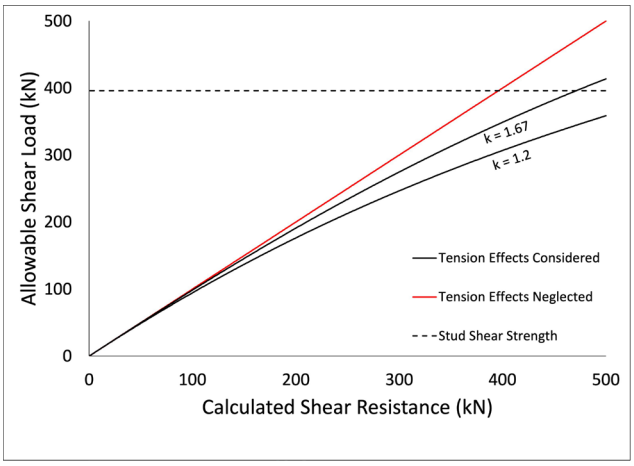

Figure 6.18 – Reduction in shear resistance due to interaction effects for the 4SEP. The unfactored stud shear strength is included and would be an upper limit. Curves shown for $k = 1.2$ and 1.67.

As shear resistance increases, achieved by increasing edge distance or adding reinforcement, tension demand also increases since the tension load is proportional to the shear load, and this results in a relative decrease in the available shear capacity. For example, for a cal- culated shear resistance of 400 kN, Figure 6.18 indicates that the theoretical failure load accounting for tension effects is only 306 kN when $k = 1.2$. Thus, if tension resistance is not increased, the available shear will be proportionally less as the calculated shear resistance increases. This effect is relevant even under current design provisions in A23.3:19. The shear capacity can still be increased by adding local reinforcement, though concrete strength must be neglected.

6.6.1 Design Aid for Calculating Anchorage Capacities

One of the most tedious parts of calculating the capacity of embeds loaded in shear is deter- mining the maximum design load, V_f, which is less than the calculated shear resistance, V_r, due to the tension-shear interaction. As discussed in Chapter 4, the tensile force in the back row of anchors is calculated using RC flexural theory. This was accounted for in the load tables provided by Chin (2021) for their standardized four, six, and eight stud embedded plates. However, these tables are limited to conservative assumptions made by Chin (2021) to keep applicability as broad as possible. For example, these tables assume that $\Psi_{c,V} = 1.0$. In situations where there is a 15M perimeter bar present and stirrups spaced at less than 100 mm on centre, these tables would be overly conservative since $\Psi_{c,V}$ may be taken as 1.4.

Unfortunately it is not as simple as increasing the tabulated values by 40%, since Figure 6.18 predicts that the increase in allowable shear will be less than that. In these situations, it is beneficial to have a design aid that can be used for any calculated shear and tension resis- tance. Another example is a situation where the capacity is increased by substituting the reinforcement resistance with the concrete breakout resistance, in which case these tables could not be used.

To eliminate the need to work with the tension-shear interaction equations, the ratio of V_f to V_r is plotted for various eccentricities of applied shear load, e (Figure 6.19a). Design- ers can calculate the governing shear and tension failure modes, and the maximum permitted shear load can be determined by multiplying the V_f/V_r ratio by V_r for a given eccentricity. For example, if V_r and T_r are calculated such that $V_r/T_r = 2$, then for an eccentricity of 75 mm, $V_f/V_r = 0.68$, meaning that the shear capacity of the connection is only 68% of the calculated shear resistance in this case.

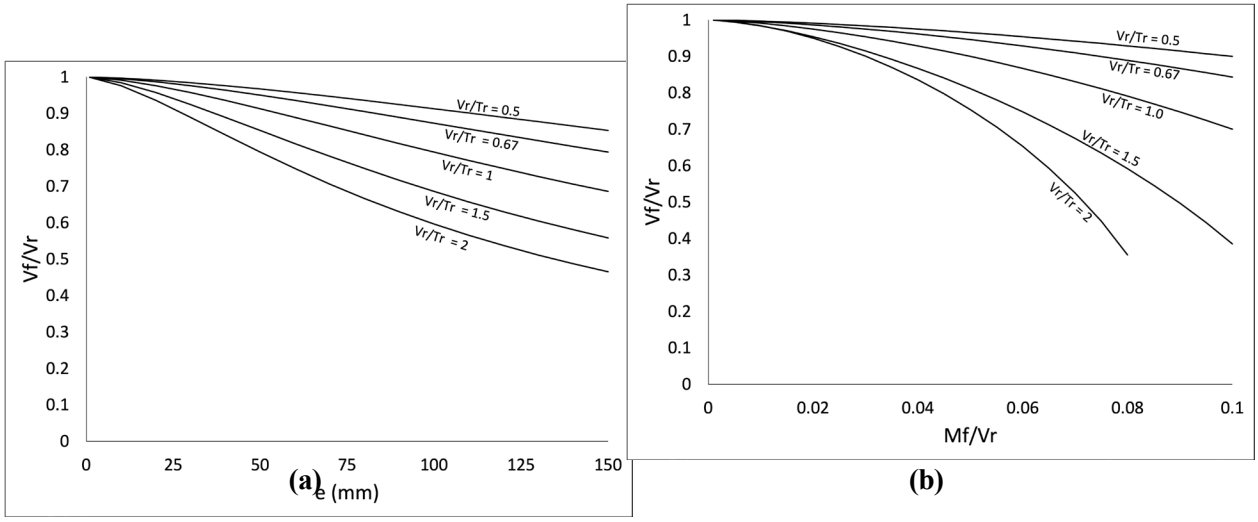

Figure 6.19 – Interaction curves for the 4SEP designed by Chin (2021) plotted as a function of (a) eccentricity of shear load and (b) applied moment.

These curves are limited to the standardized 4SEP proposed by Chin (2021), and make use of the rigid baseplate assumption. More general curves encompassing a wider variety of embedded plates are possible but are outside of this project's scope.

The curves in Figure 6.19a are limited to the assumption that the applied moment is gen- erated only by the eccentricity of the shear load, $V \cdot e$, and no other sources of moment

or rotational restraint are present. Figure 6.19b shows a similar set of design curves where the ratio of V_f/V_r is plotted against the ratio of moment, M_f, to V_r, which would apply in situations where the moment differs from $V \cdot e$.

The curves in Figure 6.19a and Figure 6.19b behave differently. Specifically, Figure 6.19a shows a sharp decrease followed by a gradual plateau, whereas Figure 6.19b shows curves that decrease more rapidly as applied moment increases. This is because the moment de- creases proportionally to V_f/V_r when it comes from eccentric shear loading, whereas M_f/V_r in Figure 6.19b is independent of the shear ratio, and is therefore more similar to the ellip- tical tension-shear interaction diagrams shown in Annex D.

These design curves only consider the failure modes discussed in Chapter 2, and other limit states pertaining to the connection between the embed and supported member should be considered separately. The rigid plate assumption allows for a simplified determination of force distribution to the back anchor and Chin (2021) indicates that the baseplate thickness of the standardized embeds is thick enough to justify this assumption. This is especially the case when shear tabs are used, as they act as a stiffener to the baseplate. The curves use $k = 1.5$ when calculating the elliptic interaction of tension and shear forces, since this exponent most closely matches the trilinear interaction diagram given by CSA A23.3:19.

6.7 Comparison to Sharma et al. (2018)

Section 4.1.1 summarized a new model presented by Sharma et al. (2018) for calculating the tension and shear capacity of embeds in RC. These expressions were used to calculate the shear resistance of the tested embeds and detailed calculations are shown in Appendix
A. To estimate capacity, first the Sharma et al. (2018) model was used to calculate shear resistance, then the tension-shear interaction equation, which predicts the most severe effect from the eccentric shear load (i.e., for a pinned connection) was applied to determine the available shear capacity. The test results are compared to the predictions in Figure 6.20a.

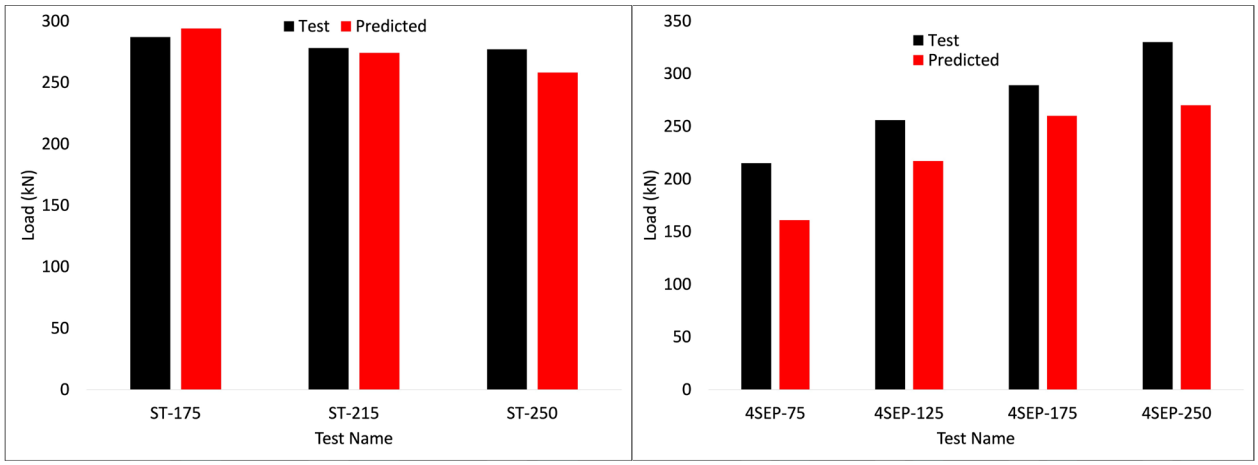

Figure 6.20 – Comparisons predictions from Sharma et al. (2018) with test results from (a) this report and (b) Chin (2021)

The test-to-predicted ratio for the three tests shown ranges from 0.98 to 1.07, suggesting rea- sonable agreement between Sharma et al. (2018)'s expressions and the experiments. Perhaps these ratios are slightly conservative because the case of concentric tension (i.e., the intended use of the interaction equation) is more severe than that of moment. When these predic- tions are compared to the tests on four stud embeds by Chin (2021), the test-to-predicted ratio ranges from 1.11 to 1.34, meaning that those tests consistently outperformed what the model from Sharma et al. (2018) predicts. Comparison of Sharma et al. (2018)'s expres- sions to Chin (2021)'s tests is shown in Figure 6.20b. One interpretation of the discrepancy is that Chin (2021) saw larger test loads due to the partially restrained loading configura- tion, which reduces tension/prying forces and increases available shear strength. However, if tension-shear interaction is neglected in the estimation of the connection strength, the test-to-predicted ratio ranges from 0.89 to 1.2, which is a better estimate than when prying effects are considered. The rotational restraint provided by Chin (2021) was likely effective in preventing the tension breakout failure that was observed in the current test program. If the loading arm used by Chin (2021) had a yield strength of 300 MPa, the plastic moment capacity through a section that includes a bolt hole is 33 kNm. A 200 kN shear load applied at a 75 mm eccentricity generates a moment of 15 kNm about the face of the baseplate. Al- though the loading arm that had plastic deformation in the test program likely yielded well beyond peak load, even if a portion of the plastic moment capacity was activated as peak load was approached, this would have an effect since the moment from eccentric shear is not

very large. This is consistent with findings from Eligehausen et al. (2019), who concluded that $V_r = \Psi V_s + \Phi V_{cgbr}$ and Φ is either 1.0 or 0.5 depending on whether uplift restraint is provided. In all cases Φ was taken as 1.0 when comparing test results to these expressions. This is because the tension-shear interaction equation is responsible for accounting for the reduced capacity associated due to tension (i.e., prying effects associated with a lack of rota- tional restraint), so applying $\Phi = 0.5$ to the shear strength is not required. The interaction equation is likely a more accurate approach than taking $\Phi = 0.5$ because this factor is based on results from tests by Sharma et al. (2017a), discussed in Section 4.1, which were loaded in such a way that there was basically zero eccentricity between the load and the baseplate.

The expressions presented by Sharma et al. (2018) provided good estimates for tests in this program when the calculated values were reduced to account for tension-shear interac- tion. Comparison of these predictions with tests from this test program and others suggests that increased rotational restraint produces increasingly conservative results if the tension- shear interaction equation is used to calculate reduced shear capacity. Although the method presented by Sharma et al. (2018) is rather cumbersome for design, breaking down the contri- bution of the reinforcement into a hook and bond model and assigning modification factors to each bar, it is fairly straightforward to implement with the help of spreadsheets or numerical software packages.

6.8 Discussion of Park et al. (2017)

Park et al. (2017) proposed methods for calculating anchor capacities in RC that involved calibrating a reinforcement "effectiveness factor," γ, against a series of single anchor tests in RC:

$$V_r = V_c + \gamma \overset{\mathbf{L}}{} V_s \tag{6.1}$$

Where V_c is the concrete breakout strength of unreinforced concrete, and V_s is the summation of the capacity of each piece of reinforcement, adjusted to account for its proximity to the embed. This model assumes that reinforcement within $0.5c_{a1}$ of an anchor can develop its yield strength, and reinforcement further from an anchor has a reduced capacity linearly proportional to the distance from the anchor. For the large diameter, single anchor tests

that were conducted, Park et al. (2017) found that $\gamma = 0.683$ provided accurate predictions of test results. However, when γ is calibrated with test results from other authors, γ varies from 0.2 to 0.75. Such a spread suggests that this model is not suitable for calculating embed capacities in general at this time and is likely related to the fact that the development length of the reinforcement is not considered in the model. The model assumes reinforcement within $0.5c_{a1}$ of an anchor is able to yield which is only true if the reinforcement is fully developed in the breakout cone, which may not be the case for anchors with small edge distances. Consequently, small γ values correspond to tests with small edge distances and larger values of γ are calculated for larger edge distances. Due to this variability, Park et al. (2017)'s model is not compared to the test results or used to estimate capacity.

6.9 Serviceability Considerations

Checking for cracking at service loads is not a requirement of Annex D. Test on embeds with multiple anchor rows show that multiple breakout cones form, with the first to form often from the front anchor row. In addition to reporting cracking loads and peak loads, Chin (2021) provided Digital Image Correlation (DIC) results of their tests at different points throughout. Chin (2021) defined cracking load as the point that the first cracks reached the edge of concrete with these cracks typically originating from the front anchor row. For their four stud embed tests the cracking load, which typically coincided with a meaningful loss of stiffness, ranged from 61% to 100% of peak load. In the test where peak load was approxi- mately equal to the cracking load, the first crack deviated from the expected 35° breakout cone angle and instead travelled parallel to the concrete edge before propagating to the edge. The load at the point that stiffness changed meaningfully was ~88% of peak load. The ratio of cracking load to peak load tended to increase as edge distance increased. This is because the displacement required for concrete to fail to the extent that load can be redistributed to reinforcement is large enough that the cracks from the front studs are fully formed before this can occur. At larger edge distances the reinforcement is engaged prior to the first cracks reaching the concrete edge. This differed from what was observed in this test program, where peak load approximately coincided with the point that cracks first propagated to the concrete edge. This behaviour is attributed to the combination of shear and tension failure observed, and if rotational restraint was present the tests likely would have cracked prior to peak load.

The cracks that formed from the back row of anchors began to form around peak load as well, eventually propagating to the edge of the concrete after a decrease in load was observed.

The overhead images taken with the Canon Rebel T6i DSLR were post processed in the DIC software VIC 2D (Correlated Solutions, 2009), and crack widths on the top surface of the block were measured by placing points on either side of the crack and tracking their relative displacement. Crack width, w_c, was found by calculating the relative displacement between two discrete points on either side of the crack, *A* and *B*. It is assumed that these two points are sufficiently close to the crack such that the relative displacement between *A* and *B* is approximately equal to that of *C* and C^t (Figure 6.21). As shown in Figure 6.21, the crack width in this project is defined as the perpendicular distance across the crack and that cracks were assumed to form at 35°.

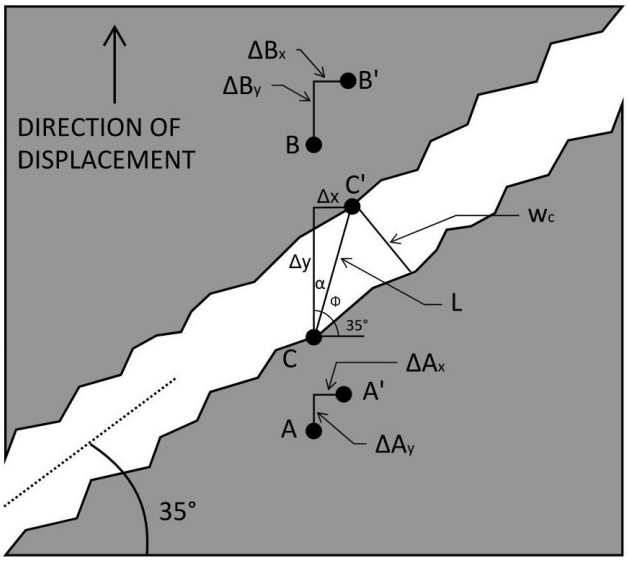

Figure 6.21 – Schematic showing how crack widths were estimated using two points, *A* and *B*, on either side of, and in close proximity to, the crack.

Using the displacement at points A and B, the crack width was calculated as follows.

$$\Delta x \approx \Delta B_x - \Delta A_x, \ \Delta y \approx \Delta B_y - \Delta A_y \tag{6.2}$$

$$L = \sqrt{\Delta x^2 + \Delta y^2} \tag{6.3}$$

$$w_c = L \sin(\varphi) \tag{6.4}$$

$$\varphi = 55 - \alpha \tag{6.5}$$

$$\alpha = \arctan\left(\frac{\Delta x}{\Delta y}\right) \tag{6.6}$$

Substituting Equations (6.3), (6.5) and (6.6) into Equation (6.4):

$$w_c = \sqrt{\Delta x^2 + \Delta y^2}\, \sin\left(55 - \arctan\left(\frac{\Delta x}{\Delta y}\right)\right) \tag{6.7}$$

Cracks widths were calculated at three locations, identified in Figure 6.22. The first two locations are at the start and end of the first crack that originated from the front studs. These are locations of interest because Location 1 captures the onset of cracking, and Location 2 is the point at which the first cracks propagate to the concrete edge, which typically coincided with the peak load. Location 3 is at the start of the crack that forms from the rear studs, which is usually the last to form for shear breakout failures. In this test program, the crack at Location 3 typically became visible at peak load. No other crack widths along the breakout cone forming from the back row of anchors were measured because the propagation of the back crack occurred almost completely following peak load, and does not provide any meaningful information in the context of serviceability.

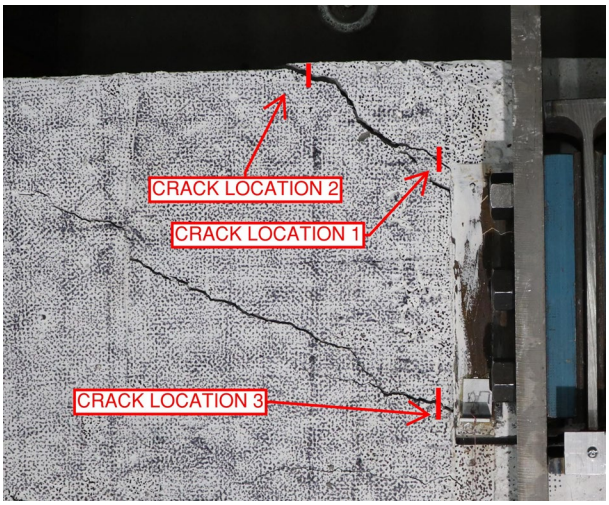

Figure 6.22 – Locations where crack widths were measured

Crack widths for ST-250^{P} are shown in Figure 6.23 and represent behaviour that was typically observed in each test. The cracks at the front of the plate begin to open up first, followed by the secondary shear breakout cracks that form from the back of the plate. The primary cracks temporarily close up as peak load is approached and the secondary cracks open, then both sets of cracks continue to open as peak load is approached. This behaviour is attributed to reinforcement's ability to tie the breakout cones together; without reinforcement, the primary crack would form and the cracks would likely not temporarily close. The crack width data was smoothed using a five point rolling average.

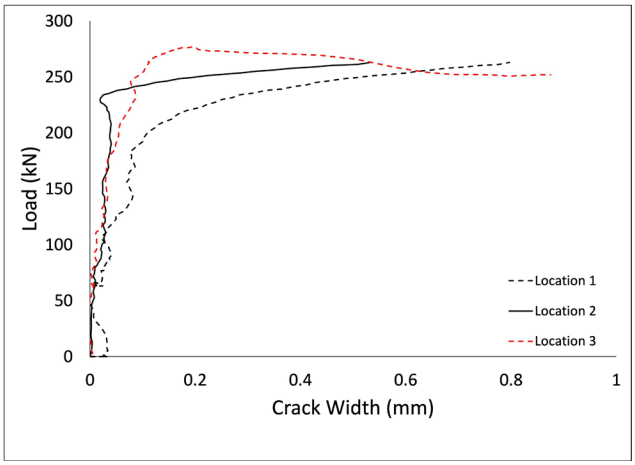

Figure 6.23 – ST-250^{P} crack widths

Crack widths at Location 1 and 2 for ST-175^{P} and ST-250^{P} are compared in Figure 6.24a, demonstrating the difference in cracking between two tests with more or less reinforcement. Location 3 is omitted because the crack widths cannot be relied on for qualitative com- parisons between tests. The out of plane rotation that was observed during the pryout failures inevitably has an effect of crack widths, but cannot be properly assessed by the two-dimensional DIC software that was used.

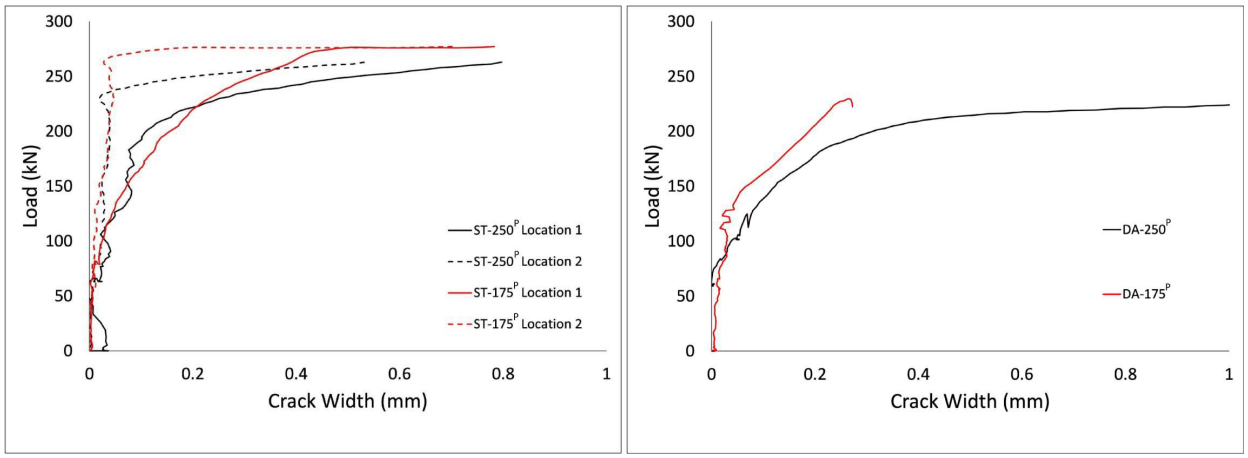

(a) **(b)**

Figure 6.24 – (a) Comparison of crack widths at Location 1 and 2 for ST-175^{P} and ST-250^{P} and (b) comparison of crack widths at Location 1 for DA-175^{P} and DA-250^{P}.

The initial formation of the cracks at the plate are similar until crack widths reach 0.2 mm, at which point the cracks in ST-250^{P} grew more rapidly. Shortly after this point, the ST-250^{P} cracks reach the edge of the concrete and the curve begins to plateau around 235 kN. The propagation of the cracks is clearly delayed by the increased reinforcement in ST-175^{P}, with the front cracks propagating to the edge later, evidenced by the curve plateauing around 270 kN.

Figure 6.24b compares the crack widths at the front of the plate (Location 1) for DA-250^{P} and DA-175^{P}, the two tests that failed by weld rupture. Prior to the welds rupturing on DA-250^{P}, cracks originating from the front anchor row were able to propagate to the concrete edge, while they stopped short of the edge in DA-175^{P}. The load versus crack width curves for all eight tests can be found in Appendix B.

Embeds loaded in shear towards a free edge will typically form a breakout cone first from the front studs, followed by the back studs. The first set of cracks can potentially be a concern at SLS because they form prior to peak load in the typical case of an embed with some degree of rotational restraint. In this test program it was observed that increased reinforcement resulted in smaller crack widths near peak load, but no meaningful difference at service load. This is attributed to the lack of rotational restraint causing the formation of the first cracks

to coincide with peak load. In tests with partial uplift restraint, Chin (2021) found that cracking load was reached as early as 61% of peak load, however it is possible that local increases in reinforcement could delay the point that cracking load is reached. The relevance of this would need to be determined on a case by case basis; the combination of load and resistance factors and the 5% fractile is so conservative that the service load is likely going to be less than 61% of the anchorage capacity even in unreinforced concrete. Where the capacity of supplementary reinforcement is substituted for the concrete breakout strength, it may be worthwhile to check the ratio of service load to concrete breakout strength since cracks tend to form prior to reinforcement picking up load.

7 Summary and Recommendations

7.1 Summary

Chapter 2 presented a literature review of headed anchors subjected to shear and tension loads. Research that influenced the design of headed anchors was presented and the discus- sion is expanded to include groups of headed studs welded to a common baseplate. Chap- ter 3 summarized the current provisions in CSA A23.3:19 Annex D for the design of embeds. Chapter 4 discussed recent efforts to better estimate the capacity of embeds in RC by ac- counting for a combination of concrete and reinforcement capacity, similar to existing shear provisions. The influence of combined shear and tension load and the effect that different shear connections have on embed behaviour is also discussed. Chapter 5 presents the test program used to examine the behaviour of embeds subjected to shear loading in RC with different shear connections. Chapter 6 presents and discusses the findings from the test program and provides recommendations for designers and future researchers.

7.2 Conclusions

The following conclusions are drawn from the report:

1. From the literature review on the behaviour and design of headed anchors and em- bedded plates in Chapters 2 and 3, limitations in the current literature and Annex D of A23.3 were identified. Currently, Annex D provides overly conservative estimates of concrete breakout capacity due to the use of the 5% fractile resistance and the treatment of concrete as if it were unreinforced. Though conservatism in design is not inherently bad, adequate levels of safety are already accounted for in limit states de- sign load and resistance factors. The combination of the 5% fractile resistance and the unreinforced concrete design assumption is overly punitive and results in inefficient de- sign. Furthermore, the treatment of combined loading is only addressed for the case of concentric tension and shear loads, but there is no guidance given for eccentric shear. Even so, the interaction equation provided by A23.3:19 is more or less conservative depending on the failure mode and reinforcement in the concrete.

2. In Chapter 4, the state of embedded plate behaviour in reinforced concrete was dis- cussed and it was found that a new model from Sharma et al. (2018) may be suited to more accurately assess embed capacity by simultaneously considering reinforcement and concrete contributions to breakout strength. Additionally, the consideration of tension shear interaction is increasingly important as the shear resistance is increased by means of additional reinforcement around the embed. As shear resistance increases, all else being equal, a larger portion of the tension breakout resistance is occupied, leaving less capacity available to resist shear. The tension shear interaction equation provides conservative estimates of the reduction in shear capacity for simple shear connections in this test program, where moment that is transferred to the embed is assumed to come only from the eccentricity of the applied load.

3. Chapter 5 details the experimental test program that was conducted, and Chapter 6 examines the results of the test program and compares them to current Canadian design standards and other recent literature. Peak load in all eight tests greatly exceeded the loads as they are calculated using CSA A23.3:19, even at the largest reinforcement spacings. The presence of minimal shear reinforcement anchored within the breakout cone is likely sufficient to reduce the variability in strength that has justified the use of the 5% fractile resistance to this point.

4. Recent research by Sharma et al. (2018) provides good estimates of the test results when tension shear interaction is accounted for. The method used to assess tension shear interaction, which assumes an applied moment proportional to the eccentric shear load, assumes there is no restraint present, i.e., the shear connection is a perfect pin. Since embeds in practical applications will not typically be free to rotate as they were in the test program, this approach is conservative provided there are no other tensile forces or moments applied to the connection.

5. The method of load application plays a pivotal role in the behaviour of the embed. The pinned loading detail used in the test program is well suited for evaluating the tension shear interaction, but less useful for evaluating the effects of reinforcement on shear capacity of the embeds since the failure mode tended towards a pryout-style, or combined tension shear failure. The only notable effect that the bolted loading arm

connection used on the last four tests had was the prevention of a weld failure in DA-215. Despite coupling the plate rotation to the load arm rotation, embeds were still able to rotate and produced tension breakout cones at peak load.

7.3 Recommendations for Future Work

To provide an improved method of calculating anchorage capacities in RC more testing is needed to better understand the effects of different reinforcement amounts/layouts on embed capacity. Full scale tests are expensive and time consuming; Finite Element Analysis (FEA) could be used to conduct parametric studies where reinforcement amount and layout is var- ied, as well as plate edge distance, anchor spacing, and number of stud rows. One series of tests should provide full uplift restraint to assess pure shear behaviour, and a second series should consider a more realistic load rotation behaviour to assess the effect this has when compared to an equivalent rotationally restrained analysis.

Whether full scale testing or FEA is utilized, future research should consider how shear load is applied to embeds to ensure that load rotation behaviour of the connection is consis- tent with what would occur in practical applications. In the current test program, embeds were able to rotate freely, which resulted in a pryout-style failure as the shear capacity in- creased by way of increased reinforcement. In reality, the severity of the pryout effect would be limited by the element that is applying load to the connection. The type of shear connec- tion could also be varied to determine the effect that more or less flexible connections have on the behaviour of embeds to verify assumptions that some designers currently make.

References

AISC (2016a). *AISC 341-16: Seismic Provisions For Structural Steel Buildings*. American Institute of Steel Construction.

AISC (2016b). *AISC 360-16: Specification for Structural Steel Buildings*. American Institute of Steel Construction.

Anderson, N. and Meinheit, D. (2000). "Design criteria for headed stud groups in shear: Part 1 — steel capacity and back edge effects." *PCI Journal*, 45, 46–75.

Anderson, N. S. and Meinheit, D. F. (2005). "Pryout capacity of cast-in headed stud an- chors." *PCI Journal*, 50(2), 90–112.

Astaneh, A. (1989). "Demand and supply of ductility in steel shear connections." *Journal of Constructional Steel Research*, 14(1), 1–19.

Astaneh, A., Call, S. M., and McMullin, K. M. (1989). "Design of single plate shear connec- tions." *Engineering Journal*, 26(1), 21–32.

ASTM (2014). *ASTM C469: Standard Test Method for Static Modulus of Elasticity and Poisson's Ratio of Concrete in Compression*. American Society for Testing and Materials, Pennsylvania, United States.

ASTM (2018a). *ASTM C39: Test Method for Compressive Strength of Cylindrical Concrete Specimens*. American Society for Testing and Materials, Pennsylvania, United States.

ASTM (2018b). *ASTM C78: Standard Test Method for Flexural Strength of Concrete (Using Simple Beam with Third-Point Loading)*. American Society for Testing and Materials, Pennsylvania, United States.

ASTM (2021). *ASTM A370: Standard Test Methods and Definitions for Mechanical Testing of Steel Products*. American Society for Testing and Materials, Pennsylvania, United States.

Batho, C. and Rowan, H. (1934). "Investigations on beam and stanchion connections." *Second Report of the Steel Structures Research Committee. London*.

Bažant, Z. P. (1984). "Size effect in blunt fracture: concrete, rock, metal." *Journal of engineering mechanics*, 110(4), 518–535.

Bažant, Z. P. and Oh, B. H. (1983). "Crack band theory for fracture of concrete." *Matériaux et Construction*, 16(3), 155–177.

Bode, H. and Roik, K. (1987). "Headed studs–embedded in concrete and loaded in tension." *ACI Symposium Publication*, 103.

Bræstrup, M., Nielsen, M., Jensen, B., and Bach, F. (1976). "Axisymmetric punching of plain and reinforced concrete."

Bui, T., Limam, A., Nana, W., Arrieta, B., and Roure, T. (2018). "Cast-in-place headed anchor groups under shear: Experimental and numerical modelling." *Structures*, 14, 178 – 196.

Bujňák, J., Mečár, J., and Bahleda, F. (2019). "Tensile resistance of an anchor plate with supplementary reinforcement." *Structural Concrete*, 20(1), 164–170.

Cannon, R. W., Godfrey, D. A., and Moreadith, F. L. (1981). "Guide to the design of anchor bolts other steel embedments." *Concrete International*, 3(7).

CEN (2004). *Eurocode 2: Design of Concrete Structures - Part 1-1: General Rules for Buildings*. European Committee For Standardization.

CEN (2019). *Eurocode 2: Design of Concrete Structures - Part 4-2: Design of Fastenings for Use in Concrete*. European Committee For Standardization.

Chin, I. (2021). "Standardization and testing of embedded plates for design, fabrication, and construction economy." MSc. report, University of Alberta.

CISC (2016). *Handbook of Steel Construction, 11th Edition*. Canadian Institute of Steel Construction, Markham, ON.

Correlated Solutions (2009). "Vic-2d reference manual." Correlated Solutions Inc.

CSA (2019). *CSA A23.3:19 Design of Concrete Structures*. Canadian Standards Association, Mississauga, ON.

DeVries, R. (1996). "Anchorage of headed reinforcement in concrete." Ph.D. dissertation, University of Texas at Austin.

Eligehausen, R. (2017). "Fastening in concrete construction past, present and future." *3rd International Symposium on Connections between Steel and Concrete*.

Eligehausen, R. and Balogh, T. (1995). "Behavior of fasteners loaded in tension in cracked reinforced concrete." *ACI Structural Journal*, 92(3), 365–379.

Eligehausen, R., Bouska, P., Cervenka, V., and Pukl, R. (1992). "Size effect of the concrete cone failure load of anchor bolts."

Eligehausen, R. and Fuchs, W. (1986). "Tragverhalten und bemessung von befestigungen ohne randeinfluß unter querzugbelastung (load-bearing behaviour and design of fixings without edge influence under shear loading)."

Eligehausen, R. and Hofmann, J. (2003). "Experimentelle und numerische untersuchungen an befestigungen am bauteilrand unter querlast (experimental and numerical investigations on fixings under shear loading close to an edge)." *Report*, University of Stuttgart.

Eligehausen, R., Mallee, R., and Silva, J. (2006). *Anchorage in Concrete Construction*, <http://dx.doi.org/10.1002/9783433601358>.

Eligehausen, R., Sharma, A., and Asmus, J. (2019). "Behavior and design of fastenings with headed studs with supplementary reinforcement close to an edge under shear loads perpendicular to the edge."

Elwell, D. J. and Fu, G. (1995). "Compression testing of concrete: Cylinders vs. cubes." *Report No. FHWA/NY/SR-95/119* (03).

Fuchs, W., Eligehausen, R., and Breen, J. E. (1995). "Concrete capacity design (ccd) ap- proach for fastening to concrete." *ACI Structural Journal*, 92(1), 73–94.

Furche, J. and Eligehausen, R. (1991). "Lateral blow out failure of headed studs near a free edge." *ACI Symposium Publication*, 130.

Gehri, N., Mata-Falcón, J., and Kaufmann, W. (2020). "Automated crack detection and measurement based on digital image correlation." *Construction and Building Materials*, 256.

Grosser, P. R. (2012). "Load-bearing behavior and design of anchorages subjected to shear and torsion loading in uncracked concrete." Ph.D. dissertation, University of Stuttgart

Hong, K., Yang, J., and Lee, S. (2002). "Moment–rotation behavior of double angle connec- tions subjected to shear load." *Engineering Structures*, 24(1), 125–132.

Jebara, K., Ožbolt, J., and Hofmann, J. (2016). "Pryout failure capacity of single headed stud anchors." *Materials and Structures*, 49(5), 1775–1792.

Jones, S. W., Kirby, P. A., and Nethercort, D. A. (1983). "The analysis of frames with semi- rigid connections - a state-of-the-art report." *Journal of Constructional Steel Research*, 3(2), 2–13.

Lee, N. H., Park, K. R., and Suh, Y. P. (2010). "Shear behavior of headed anchors with large diameters and deep embedments." *ACI Structural Journal*, 107(2), 146–156.

Lin, Z., Liu, Y., and He, J. (2014). "Behavior of stud connectors under combined shear and tension loads." *Engineering Structures*, 81, 362–376.

Morris, G. A. and Packer, J. A. (1987). "Beam-to-column connections in steel frames." *Canadian Journal of Civil Engineering*, 14(1), 68–76.

Muir, L. and Thornton, W. (2011). "The development of a new design procedure for con- ventional single-plate shear connections." *Engineering Journal*, 48.

Nethercot, D., Li, T., and Ahmed, B. (1998). "Unified classification system for beam-to- column connections." *Journal of Constructional Steel Research*, 45(1), 39–65.

Nilforoush, R. (2017). "Anchorage in concrete structures: Numerical and experimental evaluations of load-carrying capacity of cast-in-place headed anchors and post-installed adhesive anchors." Ph.D. dissertation, Luleå University of Technology.

Nilsson, M., Ohlsson, U., and Elfgren, L. (2011). "Effects of surface reinforcement on bearing capacity of concrete with anchor bolts." *Cement and Concrete Research*, 44.

Ollgaard, J. G., Slutter, R. G., and Fisher, J. W. (1971). "Shear strength of stud connectors in lightweight and normalweight concrete." *Engineering Journal, American Institute of Steel Construction*, 8(2), 55–64.

Park, Y., Jo, S., Kim, T., Kang, C., and Jae-bong, K. (2016). "Static shear strength of cast- in anchors with stirrup reinforcement." *Journal of Korean Society of Steel Construction*, 28, 1–12.

Park, Y. M., Kim, T. H., Kim, D. H., Kang, C. H., and Lee, J.-H. (2017). "Breakout shear strength of cast-in-place anchors using shaking table tests." *Proceedings of the Institution of Civil Engineers - Structures and Buildings*, 170(12), 939–950.

Richard, R. M., kung Hsia, W., and Chmielowiec, M. (1988). "Derived moment rotation curves for double framing angles." *Computers and Structures*, 30(3), 485–494.

Riemann, H. (1985). "Extended kappa -method for the design of fixing devices as exemplified by headed stud anchorages." *Betonwerk und Fertigteil-Technik/Concrete Precasting Plant and Technology*, 51(12), 808–815.

Rodriguez, D. G. and Moehle, J. P. (2021). "Comparative study of punching shear and concrete breakout." *ACI Structural Journal*, 118(2).

Shaikh, A. F. and Yi, W. (1985). "In-place strength of welded headed studs." *PCI Journal*, 30, 56–81.

Sharma, A., Eligehausen, R., and Asmus, J. (2017a). "Experimental investigation of concrete edge failure of multiple-row anchorages with supplementary reinforcement." *Structural Concrete*, 18(1), 153–163.

Sharma, A., Eligehausen, R., and Asmus, J. (2017b). "A new model for concrete edge failure of multiple row anchorages with supplementary reinforcement failure." *Structural Concrete*, 18(6), 893–901.

Sharma, A., Eligehausen, R., Asmus, J., Bujnak, J., and Schmid, K. (2018). "Analytical model for anchorages with supplementary reinforcement under tension or shear forces." *High Tech Concrete: Where Technology and Engineering Meet*, Springer International Publishing, 974–982.

Vita, N., Sharma, A., and Hofmann, J. (2019). "Local strengthening of anchorages with post-installed (supplementary) reinforcement." *IOP Conference Series: Materials Science and Engineering*, Vol. 615.

Zhao, G. (1995). "Tragverhalten von randfernen kopfbolzenverankerungen bei betonbruch (behaviour of headed stud anchors remote to an edge at concrete failure)." *Deutscher Ausschuss fuer Stahlbeton*.

Zhao, G. and Eligehausen, R. (1992). "Vorschläge zur modifikation des cc-verfahrens (propos- als for modification of the cc method)." *Report No. 12/20-91/11*, University of Stuttgart.

Zhao, G., Fuchs, W., and Eligehausen, R. (1989). "Einfluß der bauteildicke auf das tragver- halten von dübelbefestigungen im ungerissenen beton unter querzugbeanspruchung (in- fluence of component thickness on the load-bearing behaviour of anchors in non-cracked concrete under shear loading)." *Report No. 10/12A-89/5*, University of Stuttgart (March).

A Design Calculations

This appendix provides all of the design calculations that justify the sizing and selection of the structural components of the experimental program. Since these calculations were conducted with the purpose of estimating true capacity of the system, all material factors are set to 1.0 (φ = 1.0).

Embedded Plate Capacity

This section details the design checks for the embedded plates. This includes the stud shear strength, weld strengths, and shear tab/double angle capacities. Prior to the test program, expressions from Sharma et al. (2018) were used to estimate that the maximum load that could be resisted was 400 kN, so that is what the embeds were checked against.

Stud Shear Strength

The stud shear strength is given as

$$V_{sar} = \phi A_{se,V} f_{uta} \tag{A.1}$$

f_{uta} was taken as 500 MPa, consistent with material tests.

$$V_{sar} = \phi A_{se,V} f_{uta} = 0.86 \frac{\pi * 15.88^2}{4} (4) * 500 = 340 \text{kN} \tag{A.2}$$

Shear Tab

Although many of the features of the embed design are dictated by the standardized embeds proposed by Chin (2021), the shear tab was checked because the hypothesized peak load at the onset of the test program was larger than the loads calculated by Chin (2021).

Weld Strength

Treating the welds as lines, the shear force per linear mm of weld is:

$$f_v = \frac{V}{2L} = \frac{400}{2 \cdot 250} = 0.8 \text{ kN/mm} \tag{A.3}$$

Where V = design shear load (kN) and L = weld length (mm), which is doubled since there is a weld on each side of the shear tab. The force due to flexure per linear mm of weld is:

$$f_m = \frac{M}{S} = \frac{65 \cdot 400}{\frac{2 \cdot 250^2}{6}} = 1.248 \text{ kN/mm} \tag{A.4}$$

Where M is the moment due to eccentric shear (kNmm) and S is the elastic section modulus of the weld treated as a line (mm^3/mm). The peak force per linear mm of weld is:

$$f_{u,peak} = \sqrt{f_v^2 + f_m^2} = \sqrt{0.8^2 + 1.248^2} = 1.48 \text{ kN/mm} \tag{A.5}$$

The angle of the combined force with the weld axis is:

$$\theta = \arctan\left(\frac{f_m}{f_v}\right) = \arctan\left(\frac{1.248}{0.8}\right) = 57.3^\circ \tag{A.6}$$

The unfactored fillet weld strength per linear mm of weld is:

$$V_r = 0.67 \frac{DX_u}{\sqrt{2}}(1 + 0.5 \sin\theta) \tag{A.7}$$

$$V_r = 0.67 \frac{D \cdot 490}{\sqrt{2}} \cdot (1 + 0.5 \sin(57.3)) = 0.330D \text{ kN/mm}$$

Where D = weld size and X_u = weld metal ultimate strength. Equating V_r and $f_{u,peak}$:

$$0.330D = 1.48 \rightarrow D = 4.5 \text{ mm} \tag{A.8}$$

Therefore, the 10 mm weld specified by Chin (2021) is sufficient.

Block Shear

$$V_r = U_t A_n F_u + 0.6 A_{gv} \frac{F_y + F_u}{2} = (0.6)(16 * 40)(450) + (0.6)(16 * 205) \frac{300 + 450}{2} = 911\text{kN} \tag{A.9}$$

Shear Yielding

$$V_r = 0.6 A_v F_y = (0.6)(250 * 16)(300) = 720\text{kN} \tag{A.10}$$

Bolt Bearing

Bolt bearing is not checked here. The shear tab is much thicker than the web of the connected

therefore if the W section's web passes the bearing check, so too will the shear tab.

Bolt Shear

Bolts are only checked for the shear tab. The bolts are loaded in double shear for the double angle connection, so if the bolts are sufficient for the shear tab they will also be sufficient for the double angles. No area reduction factor is included because the threads are not located in the shear plane.

$$B_r = 0.6nmA_bF_{u,bolt} = (0.6)(3)(1)\left(\frac{\pi * 22.23^2}{4}\right)(825) = 576 \text{ kN} \quad \text{(A.11)}$$

Angles

The angles, welds, and bolts were selected based on CISC Tables 3-37 and 3-38 (CISC, 2016). Therefore, no design calculations were directly performed in this process. However, through industry consultation, it is understood that the capacity listed in the handbook is limited by weld capacity. For the connection selected, the factored capacity, from CISC Table 3-38, is $V_r = 300$kN. Therefore, the unfactored capacity is $300/0.67 = 447$kN.

Block Shear

$$V_r = UA_tF_un + 0.6A_{gv}\frac{F_y + F_u}{2} \quad \text{(A.12)}$$

$$= 2\left((0.6)(37 * 7.9)(450) + (0.6)(195 * 7.9)\left(\frac{300 + 450}{2}\right)\right) = 851\text{kN} \quad \text{(A.13)}$$

Shear Yielding

$$V_r = 0.6A_{gv}F_y = 2\left(\frac{1}{(0.6)(7.9 * 230)(300)}\right) = 654\text{kN} \quad \text{(A.14)}$$

W Section

Bolt Bearing

$$B_r = 3td_bnF_u = (3)(8.5)(15.88)(3)(450) = 547 \text{ kN} \quad \text{(A.15)}$$

Concrete Breakout

Sharma et al. (2018) - Numerical Example

In this section the expressions presented by Sharma et al. (2018) that were discussed in Section 4.1 are used to predict the capacity of tests with a stirrup spacing of 175 mm.

The mean concrete breakout of a single 16 mm stud, with an effective embedment length greater than $8d_a$, in 40 MPa unreinforced concrete, at an edge distance of 300 mm is given by Fuchs et al. (1995):

$$V_{cbr} = \left(\frac{l_e}{d_a}\right)^{0.2}\sqrt{\frac{f'_c}{d_a}}\,c_{a1}^{1.5} = (0.976)(8)^{0.2}\sqrt{\frac{40}{15.88}}(300)^{1.5} = 198\text{kN} \quad \text{(A.16)}$$

Where l_e/d_a is taken as the maximum permitted value of 8. The projected failure surface is

$$A_{Vco} = 4.5c_{a1}^2 = (4.5)(300)^2 = 405,000\text{mm}^2 \quad \text{(A.17)}$$

The projected failure surface for a 4 stud embedded plate, as described in the experimental program is

$$A_{Vc} = (400)(3 * 300 + 150) = 420,000\text{mm}^2 \quad \text{(A.18)}$$

The member depth modification factor is

$$\Psi_{h,V} = \sqrt{\frac{1.5c_{a1}}{h}} = \sqrt{\frac{(1.5)(300)}{400}} = 1.06 \quad \text{(A.19)}$$

The remaining modification factors that are normally present in the concrete breakout equa- tion are set to 1.0. $\Psi_{c,V}$, which normally accounts for the presence of reinforcement, is addressed in the calculation of reinforcement capacity by Equation (A.22)

Thus, the concrete breakout strength in shear of the 4 stud embedded plate is

$$V_{cbgr} = V_{cbr}\frac{A_{Vco}}{A_{Vc}}\Psi_{h,V} = (198)\left(\frac{420,000}{405,000}\right)(1.06) = 219\text{kN} \quad \text{(A.20)}$$

Turning attention to the reinforcement capacity. For 10M stirrups at a spacing of 175mm and a 15M perimeter bar (analogous to ST-175 and DA-175). The hook capacity of the first stirrup, that lies between the anchors, is given as:

$$N_{r,hook} = \Psi_1\Psi_2\Psi_3 A_s F_y \left(\frac{f_{cc}^t}{30}\right)^{0.1}$$

(A.21)

Since this is the first stirrup that is intercepted by a crack, Ψ_1 is taken as 0.95. Ψ_2 is calculated as follows

$$\Psi_2 = \left(\frac{d_L}{d_b}\right)^{2/3} \leq 1.2 = \left(\frac{16}{11.3}\right)^{2/3} = 1.26 \leq 1.2 \quad \text{(A.22)}$$

Ψ_3 is calculated as follows, nothing that the anchorage length is the length of the bar in the breakout body, less the clear cover of 32mm.

$$\Psi_3 = \left(\frac{l_1}{c_{a1}}\right)^{0.4}\left(\frac{10}{d_b}\right)^{0.25} = \left(\frac{268}{300}\right)^{0.4}\left(\frac{10}{11.3}\right)^{0.25} = 0.93 \quad \text{(A.23)}$$

The concrete cylinder strength is converted to the cube strength by

$$f_{cc}^t = f_c^t/0.85 = 40/0.85 = 47.1\text{MPa} \quad \text{(A.24)}$$

Therefore, the hook strength of the first bar, taking $f_y = 400$ MPa:

$$N_{r,hook} = \Psi_1\Psi_2\Psi_3 A_s F_y \left(\frac{f_{cc}^t}{30}\right)^{0.1} = (0.95)(1.2)(0.93)\left(\frac{11.3^2\pi}{4}\right)(400)\left(\frac{47.1}{30}\right)^{0.1} = 44.5\text{kN} \quad \text{(A.25)}$$

The bond strength is given by

$$N_{r,bond} = \frac{\pi d_b (l_1 - l_{1,min}) f_{bm}}{\alpha_2} \quad \text{(A.26)}$$

The minimum anchorage length, $l_{1,min}$ is $4d_b$ = 45mm. The bond strength, f_{bm}, is calculated as per EN1992-1-1, one of the European design provisions for concrete buildings (CEN, 2004). EN1992-1-1 provides various concrete tensile strengths based on the compressive strength, and calculates the design bond strength as a function of the tensile strength. Eligehausen et al. (2019) calculates f_{bm} by multiplying the design bond strength by a factor of 2.0. For 40 MPa concrete, EN1992-1-1 gives f_{bm} = 7.5 MPa. α_2 is given below

$$\alpha_2 = 1 - \frac{0.15(32 - 11.3)}{11.3} = 0.73 \quad \text{(A.27)}$$

Therefore, the contribution to the stirrup capacity from bond is

$$N_{r,bond} = \frac{\pi d_b (l_1 - l_{1,min}) f_{bm}}{\alpha_2} = \frac{\pi(11.3)(268 - 45)(7.5)}{0.73} = 81.3\text{kN} \quad \text{(A.28)}$$

The total stirrup resistance, before being adjusted for the eccentricity from the applied load, is then

$$N_r = N_{r,bond} + N_{r,hook} \leq A_s F_y = 81.3 + 44.5 \leq 40.1 = 125 \leq 40.1 \text{ kN} \quad \text{(A.29)}$$

Here, it is clear that the first bar is well anchored and will be able to develop its full yield strength. Moving on to the second bar, which is 175 mm on either side of the first bar (the calculation for one bar will be performed and multiplied by 2). Since the preceding bar yielded, $\Psi_1 = 0.95$, and Ψ_2 will be 1.2 for all stirrups. For Ψ_3, the anchorage length of the bar within the breakout body must first be calculated. Since the second bars are 175
mm away from the bar that is directly in between the anchors, the distance to the studs is $175 - 150/2 = 100$ mm. Therefore, if the standard 35° breakout cone is assumed, the anchorage length of the second bars is

$$l_1 = (300 - 32) - 100 \tan 35 = 198 \text{ mm} \tag{A.30}$$

$$\Psi_3 = \left(\frac{l_1}{c_{a1}}\right)^{0.4}\left(\frac{10}{d_b}\right)^{0.25} = \left(\frac{198}{300}\right)^{0.4}\left(\frac{10}{11.3}\right)^{0.25} = 0.82 \tag{A.31}$$

$$N_{r,hook} = \Psi_1\Psi_2\Psi_3 A_s F_y \left(\frac{f_{cc}'}{30}\right)^{0.1} = (0.95)(1.2)(0.82)\left(\frac{11.3^2\pi}{4}\right)(400)\left(\frac{47}{30}\right)^{0.1} = 39.2 \text{ kN} \tag{A.32}$$

The bond capacity will be very similar to that of the first bar, only with a change in the anchorage length

$$N_{r,bond} = \frac{\pi d_b (l_1 - l_{1,min}) f_{bm}}{\alpha_2} = \frac{\pi(11.3)(198 - 45)(7.5)}{0.73} = 56.1 \text{ kN} \tag{A.33}$$

The capacity for the second bars is

$$N_r = 2(39.2 + 56.1) \le 2A_s F_y = 190 \text{ kN} \rightarrow 80.2 \text{ kN} \tag{A.34}$$

This process is repeated for all of the bars that are within the breakout body with $l_1 \ge l_{min}$, and is tabulated below:

Table A.1 – Stirrup resistances for ST175 and DA175

Bar Number	# of Bars	Bar Yields? (Y/N)	Bar Capacity (kN)
1	1	Y	40
2	2	Y	80
3	2	N	63
		Total	**183 kN**

Taking $N_r = 183$ kN and adjusting for the eccentricity of the applied load

$$z = 0.85 * min(2h_{ef}, 2c_{a1}, h_a) = (0.85)(2)(150) = 255 \text{ mm} \quad \text{(A.35)}$$

$$x = 1 + \frac{e_s}{255} = 1 + \frac{65 + 32 + 5}{255} = 1.40 \quad \text{(A.36)}$$

$$V_s = \frac{183}{1.40} = 131 \text{ kN} \quad \text{(A.37)}$$

Where e_s is the eccentricity between the stirrups and the applied load, which includes the distance from the baseplate to the bolt line (65 mm), the concrete clear cover (32 mm), and half the bar diameter (5 mm). In this calculation, it is assumed that the bottom leg of the stirrup does not contribute to capacity, consistent with the mythology of the model (Figure 4.7). Finally, the concrete breakout strength in shear can be calculated.

$$V_r = V_{cgbr} + V_s = 0.5 \cdot 219 + 2 \cdot 131 = 372 \text{ kN} \quad \text{(A.38)}$$

Note that there is no factor of 0.5 in front of V_{cgbr}, since the pure (or uplift restrained) shear capacity is being calculated here, and the interaction equation is used to account for the tension effects.

Both V_r and T_r are required to implement the interaction equation. Since there is no reinforcement provided specifically to resist concrete breakout in tension of the back row of anchors, T_r can be calculated using the mean CCD expressions. The concrete breakout strength is calculated for the back row of anchors only, since these are the only ones in tension due to the eccentric shear load. Some Ψ factors are omitted in the calculation of T_r as they do not apply to this case.

$$T_r = T_{cgbr} = k_c \sqrt{f'_c} h_{ef}^{1.5} \frac{A_{Nc}}{A_{Nc0}} \Psi_{c,N} \quad \text{(A.39)}$$

$$T_r = 16.8\sqrt{40}(150)^{1.5}\frac{(3 \cdot 150)(3 \cdot 150 + 150)}{9 \cdot 150^2} 1.25 = 325 \text{ kN}$$

The interaction equation can now be used to solve for V_f, the allowable shear load, which is less than V_r due to interaction effects. Usually this is an iterative process since T_f is a function of V_f. However, referring to Figure 6.19 and interpolating between curves for $V_r/T_r = 1.14$ and $e = 65$ mm, the ratio of V_f/V_r is ~0.78. Therefore, V_f is $0.78 \cdot 372 = 290$ kN. The shear capacity is reduced by 82 kN as a result of the interaction of tension and shear forces, referred to in this report as the prying effect.

B Load versus Crack Width Plots

Refer to Section 6.9 for Locations 1, 2 and 3.

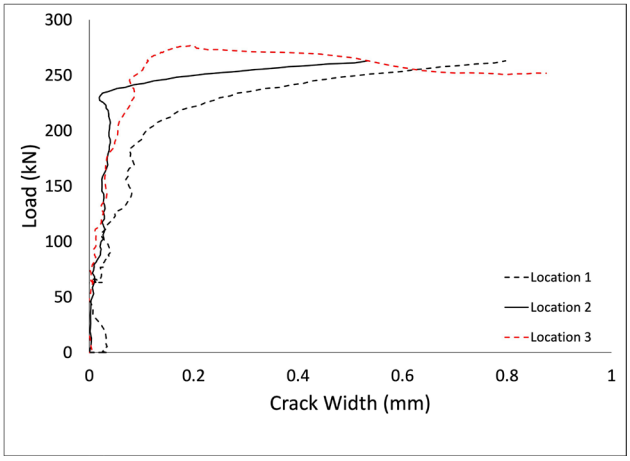

Figure B.1 – ST-250 crack widths

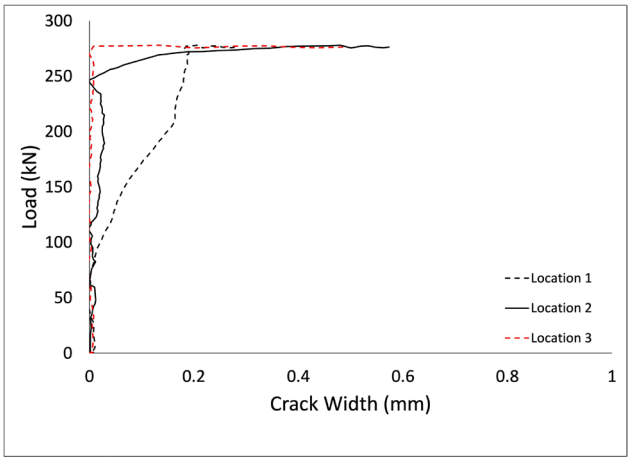

Figure B.2 – ST-215 crack widths

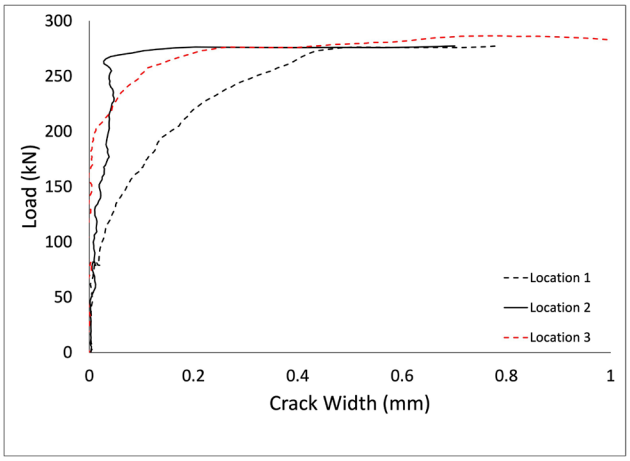

Figure B.3 – ST-175 crack widths

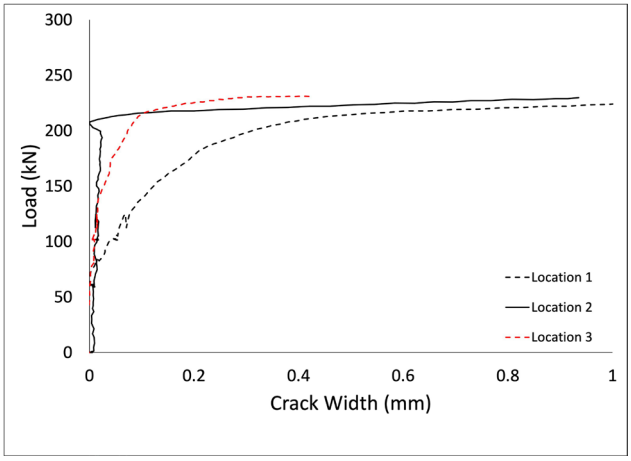

Figure B.4 – DA-250 crack widths

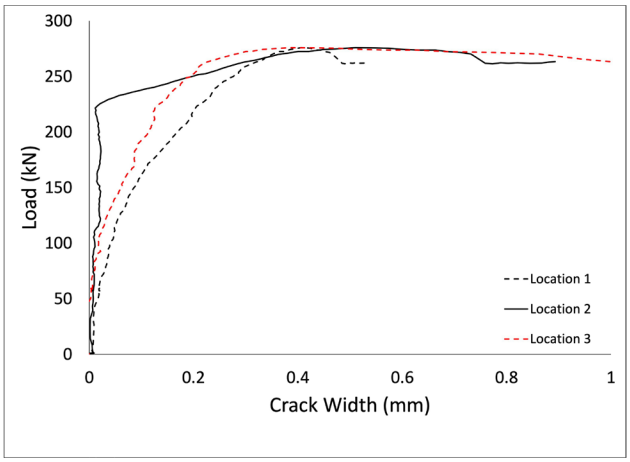

Figure B.5 – DA-215 crack widths

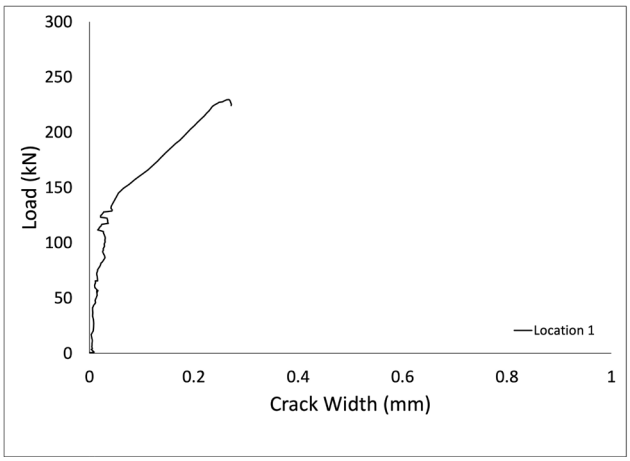

Figure B.6 – DA-175 crack widths

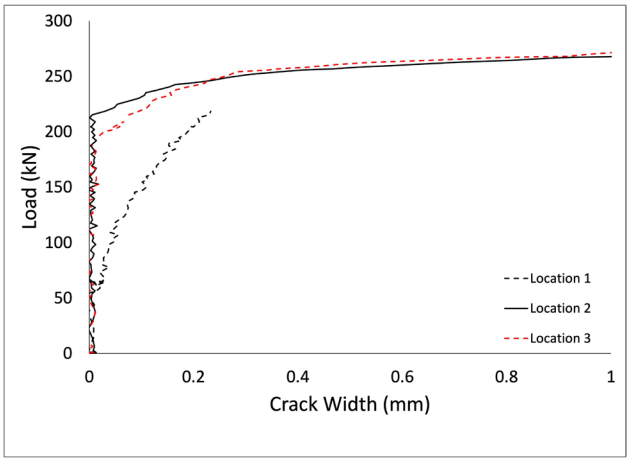

Figure B.7 – PR-20M crack widths

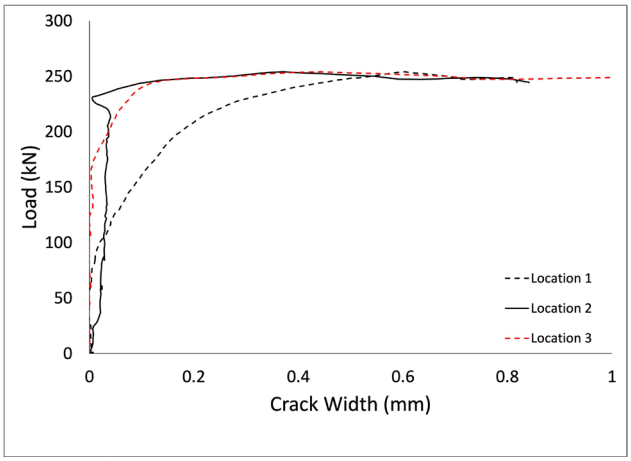

Figure B.8 – PR-UR crack widths

C Material Properties

Table C.1 – Headed Studs

	Specimen 1	Specimen 2	Specimen 3	Mean	Standard Deviation
E_s (GPa)	216	201	196	204	10.4
f_{uta} (MPa)	503	510	505	506	3.6
Initial Diameter	9.01	9.02	9.02	9.02	0.01
Initial Area (mm^2)	63.8	63.9	63.9	63.9	0.1

Table C.2 – 10M Reinforcement

	Specimen 1	Specimen 2	Specimen 3	Mean	Standard Deviation
E_s (GPa)	201	201	209	204	4.6
f_y (MPa)	470	462	471.5	468	5.1
f_u (MPa)	680	680	682	681	1.2
Yield Force (kN)	47.1	46.3	47.3	46.9	0.51
Peak Force (kN)	68.2	68.2	68.4	68.3	0.12

Table C.3 – 15M Reinforcement

	Specimen 1	Specimen 2	Specimen 3	Mean	Standard Deviation
E_s (GPa)	201	201	209	204	4.6
f_y (MPa)	463	459	463	462	2.3
f_u (MPa)	691	691	689	690	1.2
Yield Force (kN)	93.1	92.3	93.1	92.8	0.46
Peak Force (kN)	138.9	138.9	138.5	138.8	0.23

Table C.4 – 20M Reinforcement

	Specimen 1	Specimen 2	Specimen 3	Mean	Standard Deviation
E_s (GPa)	197	202	194	198	4.0
f_y (MPa)	413	413	405	410	4.6
f_u (MPa)	596	592	603	597	5.6
Yield Force (kN)	123.3	123.3	121.0	122.5	1.38
Peak Force (kN)	178.0	176.8	180.1	178.3	1.66

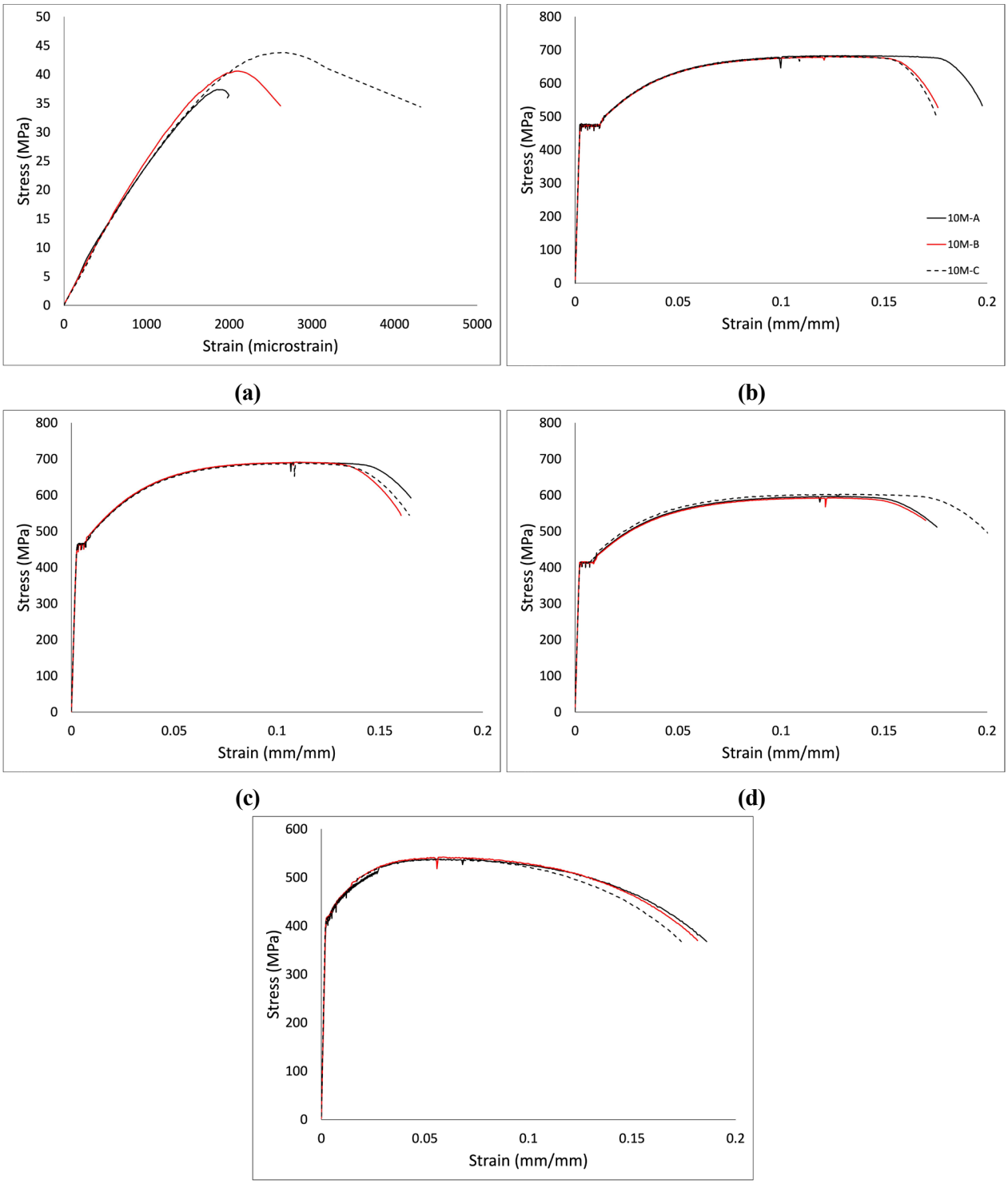

Figure C.1 – Stress strain curves for (a) concrete cylinders, (b) 10M reinforcing bars, (c) 15M reinforcing bars, (d) 20M reinforcing bars, and (e) headed studs